Role of EHD1 in Renal Proximal Tubular Endocytosis and Recycling

DISSERTATION



ZUR ERLANGUNG DES DOKTORGRADES DER NATURWISSENSCHAFTEN
(DR. RER. NAT.) DER FAKULTÄT FÜR BIOLOGIE UND VORKLINISCHE
MEDIZIN DER UNIVERSITÄT REGENSBURG

vorgelegt von
Sara Cerqueira Afonso
aus Lissabon, Portugal

im Jahr 2017

Promotionsgesuch eingereicht am: 27.10.2017

Die Arbeit wurde angeleitet von: Herr Prof. Dr. med. Richard Warth

Prüfungsausschuss: Herr Prof. Dr. rer. nat. Reinhard Sterner (Vorsitzender)

Herr Prof. Dr. med. Richard Warth (1. Gutachter/Prüfer)

Frau Prof. Dr. rer. nat. Marina Kreutz (2. Gutachter/Prüfer)

Herr Prof. Dr. rer. nat. Rainer Schreiber (3. Prüfer)

Unterschrift _____

(Sara Cerqueira Afonso)

Table of Contents

Table of Contents 1
1. Introduction 5
1.1 Clinical case and identification of new gene mutation 5
1.2 The EHD Protein Family 6
1.2.1 Tissue expression of EHD proteins and subcellular localization 7
1.2.2 General structure of EHD proteins 7
1.2.3 Function of EHD proteins 10
1.2.3.1 EHD1 13
1.2.3.2 EHD2 16
1.2.3.3 EHD3 17
1.2.3.4 EHD4 18
1.2.4 EHD proteins and human diseases 19
1.3 The Kidney and EHD Proteins 21
1.4 The Inner Ear and EHD Proteins 23
1.5 The Testis, Epididymis and EHD proteins 24
2. Objectives 26
3. Materials and Methods 27
3.1 Materials 27
3.1.1 Instruments 27
3.1.2 Laboratory material 28
3.1.3 Substances 29
3.1.4 Enzymes, Kits 31
3.1.5 Software 32
3.1.6 Oligonucleotides 32
3.1.7 Antibodies 33
3.1.8 Buffers and Solutions 34
3.2 Methods 38
3.2.1 Mice 38
3.2.1.1 The *Ehd1*$^{-/-}$ mouse model 38
3.2.1.2 Isolation of genomic DNA 39
3.2.1.3 Genotyping of *Ehd1*$^{-/-}$ mice 39
3.2.2 Cell lines 40

3.2.2.1 Inducible LLC-PK1 WT-, R398W-hEHD1 cell lines 40
3.2.3 Histological Methods 40
3.2.3.1 Retrograde arterial perfusion and tissue fixation 40
3.2.3.2 Bouin's fixation of paraformaldehyde-perfused testicles and epididymis ...40
3.2.3.3 Paraffin embedment of paraformaldehyde-perfused tissue and sections preparation 41
3.2.3.4 Cryo preparation of paraformaldehyde-perfused tissue and sectioning 41
3.2.3.5 Preparation of paraformaldehyde-perfused tissue for electron microscopy 42
3.2.3.6 Hematoxylin and Eosin staining 42
3.2.3.7 Periodic Acid–Schiff staining 42
3.2.3.8 Detection of β-galactosidase activity: X-Gal staining 43
3.2.3.9 Immunohistochemistry 43
3.2.3.10 Microscopy 44
3.2.4 Molecular Biology Methods 45
3.2.4.1 Isolation of total RNA from mouse tissue and LLC-PK1 cells 45
3.2.4.2 Synthesis of cDNA by RNA reverse transcription 46
3.2.4.3 Quantitative Polymerase Chain Reaction (Real time PCR) 46
3.2.4.4 Isolation of protein from mouse kidney and LLC-PK1 cells 47
3.2.4.5 Quantification of protein samples 47
3.2.4.6 Western blot 48
3.2.4.7 Co-immunoprecipitation (Co-IP) in mouse tissue 49
3.2.4.8 Coomassie blue staining of SDS-PAGE from mouse spot urine 49
3.2.5 Auditory brainstem response measurement in the mouse 50
3.2.5.1 Mouse preparation 50
3.2.5.2 f-ABR measurement (frequency-specific auditory brainstem responses) ..51
3.2.5.3 Data evaluation 51
3.2.6 Evaluation of mouse spermatozoon motility 51
3.2.7 Challenge of the mice with the low-molecular-weight protein β_2-microglobulin 51
3.2.7.1 Conjugation of β_2-microglobulin with the fluorescent tag Alexa Fluor 546 .51
3.2.7.2 IV injection of β_2-microglobulin-Alexa Fluor 546 into mice 52
3.2.7.3 Isolation of blood serum and kidney homogenization 52
3.2.7.4 Measurement of β_2-microglobulin-Alexa Fluor 546 fluorescence 52
3.2.8 Measurement of colocalization using immunofluorescence 53
3.2.9 Live-imaging of renal proximal tubular endocytosis in the mouse kidney 53
3.2.9.1 Mouse preparation 53
3.2.9.2 Multiphoton microscopy 53

3.2.9.3 Data evaluation 54
3.2.10 Determination of protein stability 54
3.2.11 Transepithelial transport of bovine serum albumin (BSA) by LLC-PK1 cells ..54
3.2.12 β_2-microglobulin uptake by LLC-PK1 cells 55
3.2.13 Statistics 55
4. Results 57
4.1 Expression and localization of EHD1 in the mouse tissues 57
4.1.1 *Ehd1* mRNA levels in the mouse 57
4.1.2 EHD1 localization in mouse tissues on the cellular level 57
4.1.2.1 EHD1 localization in the testis 58
4.1.2.2 EHD1 localization in the kidney 59
4.2 Characterization of the *Ehd1*$^{-/-}$ mouse phenotype 64
4.2.1 Generation of *Ehd1*$^{-/-}$ mouse 64
4.2.2 Basic phenotype of the *Ehd1*$^{-/-}$ mouse 65
4.2.3 Eye phenotype of the *Ehd1*$^{-/-}$ mouse 66
4.2.4 Inner ear phenotype of the *Ehd1*$^{-/-}$ mouse 67
4.2.4.1 Histology of the cochlea in the *Ehd1*$^{-/-}$ mouse 67
4.2.4.2 Measurement of the *Ehd1*$^{-/-}$ mouse hearing ability 68
4.2.4.3 Effect of *Ehd1* deletion on gene expression in the cochlea 69
4.2.5 Testis and epididymis phenotype of the *Ehd1*$^{-/-}$ mouse 70
4.2.5.1 Size of the testes and epididymides in the *Ehd1*$^{-/-}$ mouse 70
4.2.5.2 Histology of the testis and epididymis in the *Ehd1*$^{-/-}$ mouse 71
4.2.5.3 Effect of *Ehd1* deletion on gene expression in the testis and epididymis ..76
4.2.6 Kidney phenotype of the *Ehd1*$^{-/-}$ mouse 76
4.2.6.1 Histology of the kidney in the *Ehd1*$^{-/-}$ mouse 77
4.2.6.2 Test for low-molecular-weight proteinuria in the *Ehd1*$^{-/-}$ mouse 78
4.2.6.3 β_2-microglobulin internalization by renal proximal tubules in the *Ehd1*$^{-/-}$ mouse 80
4.2.6.4 Live-imaging of β_2-microglobulin endocytosis in the *Ehd1*$^{-/-}$ mouse kidney 82
4.2.6.5 Effect of *Ehd1* deletion on gene expression and protein localization in the kidney 85
4.3 LLC-PK1 inducible cell lines 87
4.3.1 WT- and R398W-EHD1 cellular localization 87
4.3.2 WT- and R398W-EHD1 protein stability 89
4.3.3 WT- and R398W-EHD1 protein function 90
4.3.4 Gene expression in WT- and R398W-EHD1 LLC-PK1 cells 92

5. Discussion....94
5.1 *Ehd1* deletion and mouse lethality....94
5.2 *Ehd1*$^{-/-}$ mouse and eye abnormalities....95
5.3 *Ehd1*$^{-/-}$ mouse and hearing deficiency....95
5.4 *Ehd1*$^{-/-}$ mouse and male infertility....96
5.5 *Ehd1*$^{-/-}$ mouse and impaired proximal tubule endocytosis....98
5.6 R398W-EHD1 presents an altered cellular localization....102
6. Summary....104
7. Zusammenfassung....105
8. References....107
9. List of Figures....118
10. List of Tables....120
11. Supplements....121
11.1 Figures....121
11.2 Publications in preparation....122
11.3 Presentations at scientific conferences....122
11.4 Eidesstattliche Erklärung....123
12. Acknowledgments....124

1. Introduction

1.1 Clinical case and identification of new gene mutation

The premise for this dissertation was a clinical case followed up by our co-workers Prof. Dr. Robert Kleta and Dr. Naomi Issler (Royal Free Hospital – Centre for Nephrology, London). In Israel, they examined a total of six patients from four families, three males and three females with ages between 7 and 15 years old. All the patients displayed signs of tubular proteinuria (loss of low-molecular-weight proteins in the urine), with a loss of 1–2 g of protein per day, and sensorineural hearing loss in the high frequency range (>2000 Hz; Figure 1.1). Although glomerular kidney function was normal, the dimercaptosuccinic acid (DMSA) scan — a test used to assess renal morphology, structure and function — showed a poor uptake of this radionuclide by the kidneys, while in normal individuals it accumulates in the kidneys.

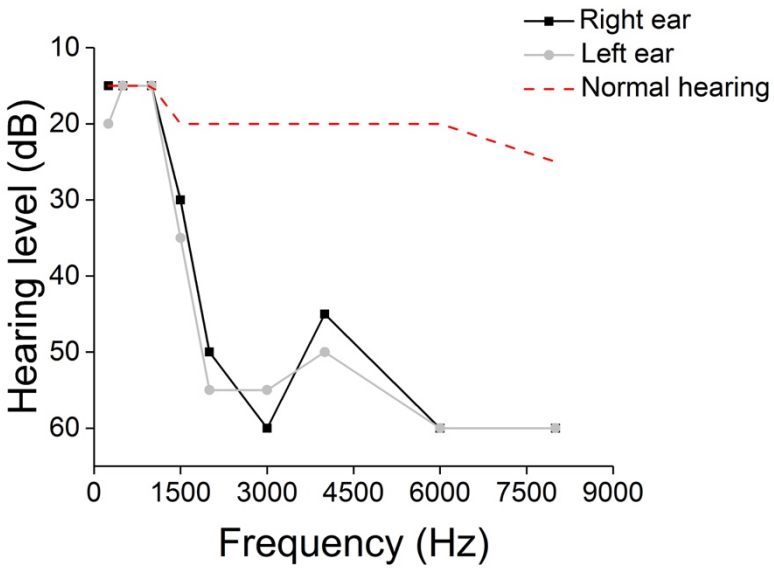

Figure 1.1: Representative audiogram from one of the patients.
The audiogram was performed for both ears and was indicative of a hearing deficit at frequencies higher than 2000 Hz, since the level of the sound required for hearing is increased to ~60 dB, while in a normal audiogram the level is 10–20 dB.

In all four affected families marriages between cousins had occurred facilitating the genetic analysis. Using linkage analysis, Robert Kleta identified the disease-causing locus on chromosome 11. DNA sequencing and haplotype reconstruction revealed a mutation in the gene for the C-terminal Eps15 homology domain protein 1 (EHD1; c.1192C>T). This missense mutation is localized in the exon 5 of the *EHD1* gene and causes an amino acid substitution of an arginine by a tryptophan at the position 398 in the EHD1 protein

(p.Arg398Try or R398W). The disease is inherited in an autosomal recessive fashion (Figure 1.2).

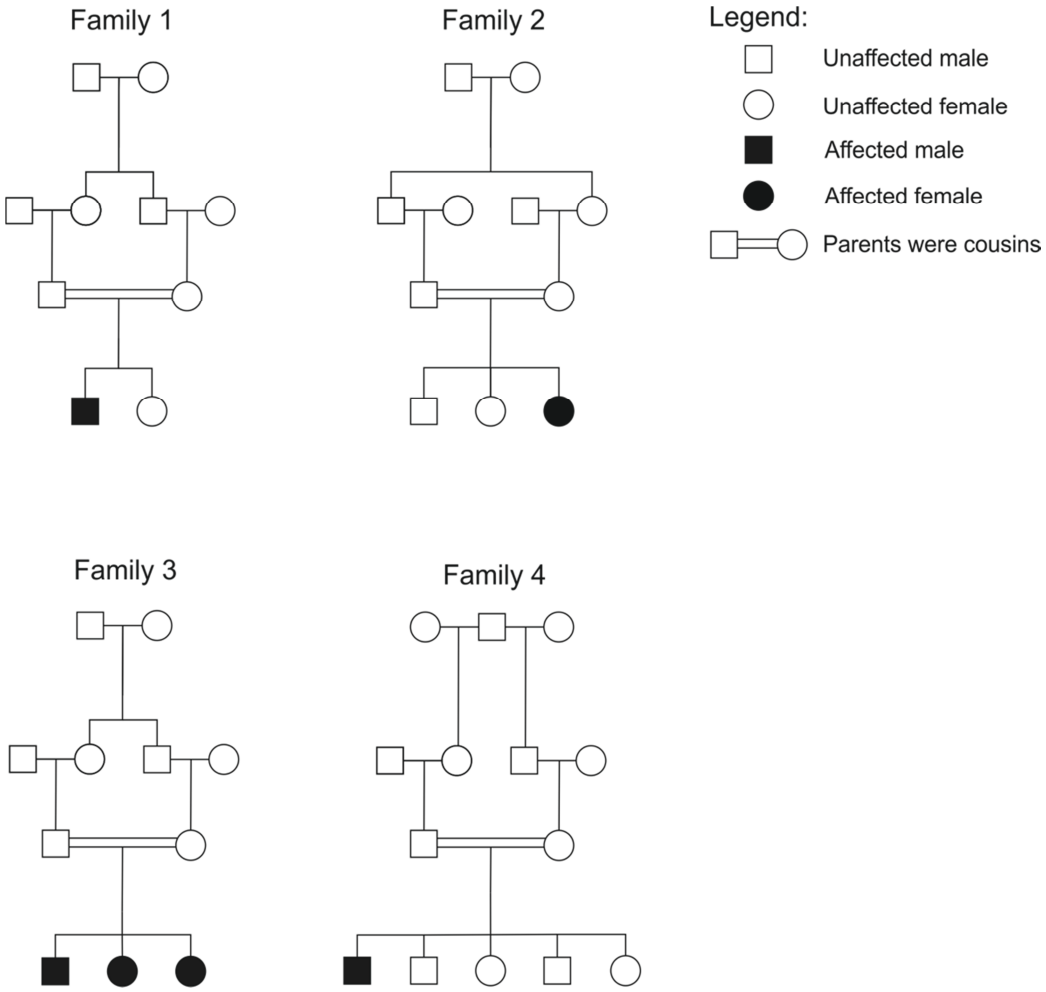

Figure 1.2: Pedigrees of the four families of the examined patients.
The analysis of the pedigrees of all families indicated that the mutation segregates within the families in an autosomal recessive pattern, meaning that only the individuals carrying the mutation in both alleles manifest the disease.

1.2 The EHD Protein Family

The human C-terminal Eps15 homology (EH) domain (EHD) protein family was first characterized around 20 years ago [1,2]. Mammals express four EHD homologous, EHD1 – 4, whose genes are located on different chromosomes: *EHD1* on 11q13, *EHD2* on 19q13.3, *EHD3* on 2p21 and *EHD4* on 15q11.1 [1] in humans and on chromosomes 19, 7, 17 and 2, respectively in mouse [3]. However, all the four proteins show high levels of amino acid sequence-similarity and -identity with each other (70–86%), with EHD1 and EHD3 being the most closely related [4,5]. Orthologs of EHD proteins are also found in some invertebrate organisms, like *C. elegans* or *Drosophila melanogaster*, whose genomes contain only a single *EHD* gene, known as Rme-1 [6] and Past1 [7], respectively.

1.2.1 Tissue expression of EHD proteins and subcellular localization

EHD proteins show a broad tissue expression. As shown in Table 1.1, in murine tissues, EHD1 and EHD4 have a wide range of expression and can be found in brain, thymus, heart, muscle, liver, spleen, lung, kidney, eye, inner ear and EHD1 is further expressed in the testis [8–11]. EHD2 is mainly expressed in the lung, heart, spleen and mammary glands [8,9]. EHD3 seems to be specific from the brain, liver, kidney, spleen and eye [8,9,11].

Table 1.1: Expression of EHD proteins in the mouse tissues.

	Tissue expression											
	Brain	Thymus	Heart	Muscle	Liver	Spleen	Lung	Kidney	Eye	Inner ear	Testis	Mammary glands
EHD1	x	x	x	x	x	x	x	x	x	x	x	
EHD2			x			x	x					x
EHD3	x				x	x		x	x			
EHD4	x	x	x	x	x	x	x	x	x	x		

EHDs subcellular localization was assessed by overexpression in HeLa cells [9]. EHD1, 3, and 4 were present in pleomorphic tubulovesicular structures in the perinuclear area and showed substantial colocalization with each other [9]. In contrast, EHD2 lacked expression in perinuclear tubular structures and showed punctated vesicular staining throughout the cytoplasm and often also in the plasma membrane. EHD2 displayed no colocalization with EHD1 or EHD3, but a partial colocalization with EHD4 [9]. The differences in subcellular localization may suggest that, although some redundancy in function can be expected due to their high sequence similarity, the members of the EHD family serve distinct functions.

1.2.2 General structure of EHD proteins

The EHD proteins have a length of 534–543 amino acids and their general structure encompasses a nucleotide binding domain, flanked by two helical regions, and an EH domain in the C-terminus connected to the helical domain by a linker region (Figure 1.3) [12]. This predicted domain architecture could be confirmed when the crystal structure of the full-length mouse EHD2 protein was obtained (Figure 1.4) [13]. More recently, the crystal structure of the EHD4 dimer was elucidated by X-ray, showing once again a similar domain architecture [14].

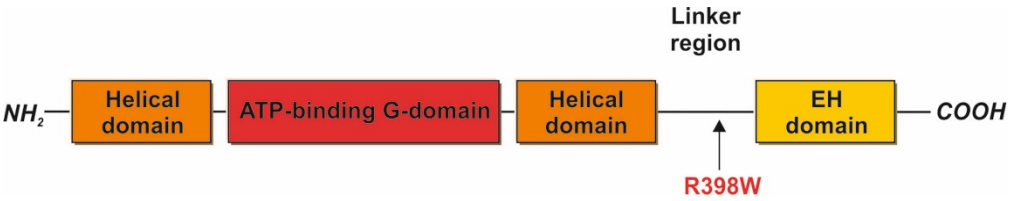

Figure 1.3: Diagram of EHD domain architecture.
EHDs comprise an ATP-binding domain flanked by two helical regions and a C-terminal EH domain connected with the helical domain by a 40-residue linker region. The identified R398W mutation is located within the linker region of the EHD1 protein.

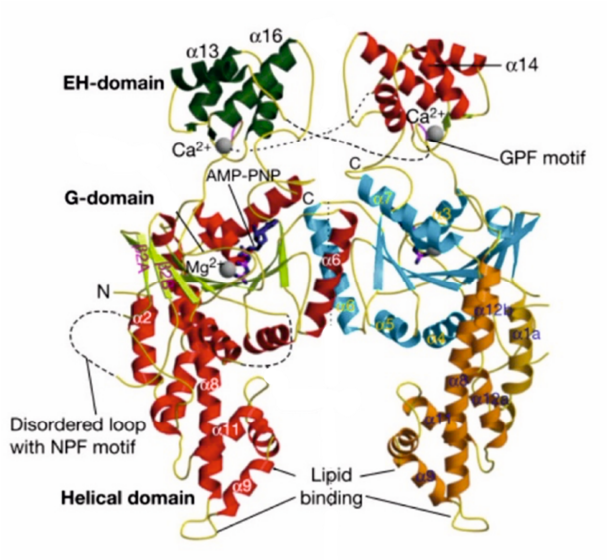

Figure 1.4: The structure of mouse EHD2 dimer.
Ribbon-type representation of the EHD2 dimer. One molecule is colored according to the secondary structure (left; helices in red, β-sheets in green) and the other according to the domain structure (right; helical domains in orange and yellow, G-domain in blue and EH domain in red). GPF (glycine-proline-phenylalanine) and NPF (asparagine-proline-phenylalanine) motifs are indicated. Modified from *Daumke et al, 2007* [13].

The EH domain is a highly conserved motif (50–60% sequence similarity) comprising ~100 residues that is found in proteins from haemosporida, fungi, plants, nematodes, artropoda, amphibia and mammalia [4,15]. This domain was first identified around 20 years ago as a stretch of ~100 residues repeated three times at the N-terminus of the tyrosine kinase substrate Eps15, which is also a substrate for the epidermal growth factor receptor [16,17]. So far several EH domains have been determined using nuclear magnetic resonance (NMR) spectroscopy, including the EH1 of mouse Eps15 [18], the EH2 and EH3 of human Eps15 [19,20], the EH of POB1 [21], the EH of Reps1 [22] and the EH domain of EHD1 [23]. In mammals 11 EH domain containing proteins were identified which can be organized into 5 distinct families: (i) Eps15, (ii) Intersectin, (iii) Reps, (iv) γ-synergin and (v) EHD proteins [24]. All of these EH domains contain two helix-loop-helix motifs known as EF-hands, which are linked by a short anti-parallel β-sheet and are calcium binding sites. Although they present calcium bind sites, not all EF-hands are capable of binding calcium, and they

have been termed either ‘canonical’ or ‘pseudo’ EF-hands, depending on their binding ability [25,26]. *In vitro* studies using NMR spectroscopy revealed that indeed EHD1 EF-hands are capable of binding calcium [27] and a co-immunoprecipitation assay exhibited an EH domain- and calcium-dependent interaction between EHD4 and Cadherin 23 [10]. The EH domain is mainly responsible for protein-protein interactions through recognition of a NPF (asparagine-proline-phenylalanine) binding motif in the target protein [28,29]. Different studies showed that NPF residues enter a conserved hydrophobic pocket within the EH domain, allowing close contact between the asparagine residue of the NPF and a highly conserved tryptophan residue in the EH domain [19,20]. The importance of this bond was confirmed by mutation of the conserved tryptophan residue, which led to severe impairment of the bond between EH domain and NPF motifs [19]. Unlike the EH domains of most proteins that are localized in the N-terminal region, the EH domain in EHD1–4 is at the C-terminal. Although the 3D structures of N- and C-terminal EH domains share a high similarity, the NMR solution structure of the EHD1 EH domain showed a highly positively charged surface, while N-terminal EH domains generally have a negatively charged surface area [23,29]. This leads to a selective binding of the positively C-terminal EH domains to a subset of NPF-containing proteins that contain acidic residues following the NPF motif [30,31]. Some of these NPF-containing proteins are SNAP29 [32], EHBP1 [33], rabenosyn-5 [34], Rab11-Fip2 [35], syndapin [35] and myoferlin [35]. All these interactions suggest a role in endocytosis and protein recycling, which will be covered in a later section. The C-terminal EH domains are also able to recognize other binding motifs. The crystal structure of the EHD2 dimer identified a GPF (glycine-proline-phenylalanine) motif localized in the linker region that is predicted to bind to the EH domain of the opposing dimeric EHD2 (Figure 1.4) [13]. *In vitro* assays, where the human EH domain of EHD1 was incubated with several peptides, demonstrated the ability of this domain to bind to NPF, GPF and DPF (aspartic acid-proline-phenylalanine) motifs, although with different affinities, with the binding affinity for NPF being much higher than for the other motifs [31,36].

The EHD proteins also contain an ATP (Adenosine triphosphate)/GTP (Guanosine triphosphate)-binding site similar to the one found in Ras and dynamin family GTPases. The first study to demonstrate the functional significance of the predicted nucleotide-binding site utilized an *in vivo* endocytic assay to show that growing oocytes possessing a mutation within the conserved nucleotide-binding site of the *C. elegans* Rme-1 protein exhibited impaired uptake of the yolk protein [6]. Later, the equivalent mutation in human EHD1 led to impairment of the protein association with membranes [37].

The ATP/GTP-binding site was finally confirmed with the elucidation of the crystal structures of both EHD2 and EHD4 in the presence of a non-hydrolysable ATP analogue [13,14] and although the nucleotide binding site has a high similarity to the GTP-binding

proteins, surprisingly all EHD proteins showed a much higher affinity for ATP than GTP [38]. This domain is highly important for the proteins function, which will be discussed in the following section.

1.2.3 Function of EHD proteins

Endocytosis is a very important process in mammalian cells that plays a role in nutrient uptake, cell polarity, internalization of surface receptors, immune surveillance, development and homeostasis [39,40]. The endocytic process includes several mechanisms by which cells internalize molecules and particles into transport vesicles derived from the plasma membrane. All endocytic mechanisms can be divided in two groups, those that are clathrin-dependent and those that are clathrin-independent [39,41,42]. In clathrin-dependent endocytosis (CDE), the cytoplasmic domains of plasma membrane proteins are specifically recognized by adaptor proteins developing clathrin-coated pits, and subsequently clathrin-coated vesicles that are brought into the cell. CDE is facilitated by numerous accessory proteins and requires the GTPase dynamin for vesicle scission [41,42]. Clathrin-independent endocytosis (CIE) was discovered when the endocytosis of many types of endogenous and exogenous cargoes was relatively unaffected by inhibition of CDE, suggesting an alternative pathway. Furthermore, the internalization of these molecules is mainly cholesterol-dependent, which is not the case in CDE [42].

The fate of all endocytosed receptors and membranes is then determined by a complex network of protein-protein interactions mediated by specific modules. Regardless of the mode of entry, the internalized receptors are sorted at the early endosome (EE), and while some are designated for degradation, others are sorted by the endosomal system and returned to the plasma membrane where these proteins can partake in additional rounds of internalization. This “rescue” of molecules is known as endocytic recycling and can be divided in two groups, fast recycling — when the receptors are trafficked to the plasma membrane through a direct way — and slow recycling — when the receptors are trafficked via the endocytic recycling compartment (ERC) [41]. The most prominent morphological characteristics in the recycling system are the dynamic tubulation of the recycling system membranes and vesicle formation. A complex network of proteins is involved in this elaborate process, e.g. the Rab and EHD proteins [41,43,44].

The Rabs are members of the Ras superfamily of small GTP-binding proteins and known to be involved not only in the membrane trafficking but also in cell signaling, cell migration, cytokinesis, ciliogenesis, apoptosis and autophagy [45]. A classic example of Rab involvement in vesicle formation is the one of Rab5. The Rab5–GDI (GDP dissociation inhibitor) complex is required for clathrin-coated vesicle formation *in vitro* [46] and overexpression of a Rab5-GAP (GTPase-activating protein), inhibits epidermal growth

factor receptor internalization [47]. Also the Rab11a-containing recycling system utilizes multiple mechanisms for the growth of tubules and their subsequent vesiculation [48,49]. Rab8 and Rab35 were reported to be distributed into tubular and vesicular endosomes and also to be involved in the recruitment of EHD proteins [50,51].

EHD proteins have been linked to a number of Rab proteins through their association with mutual effectors, namely molecules interacting with CasL-Like1 (MICAL-L1) [52], Rabenosyn-5 [34] and Rab11-FIP2 [35]. Although Rabs are primarily involved in vesicle tethering and fusion, EHDs may function in vesicle scission, thus regulating vesicle transport from endosomes to downstream compartments [13]. The elucidation of the crystal structure of both EHD2 [13] and EHD4 [14] made a great contribution to the understanding of EHDs functional mechanisms, leading to the proposal of a model in which these proteins have a function in the regulation of membrane fission (Figure 1.5) [12,44]. EHD dimerization seems to be required for association with tubular membranes, since EHD mutants, impaired in their ability to homo- or hetero-oligomerize, display a cytoplasmic distribution [35]. Dimerization of EHDs is mediated by a hydrophobic interface in the nucleotide-binding G domain upon ATP binding [13,14]. After dimerization, the association with the tubular membranes is facilitated by EHDs lipid-binding helical regions [13,14] or through direct binding of C-terminal EH domains to phosphatidylinositols [27]. In addition, the recruitment and stabilization of EHDs to and on membranes can be assisted by EH domain binding to different NPF-containing interaction partners [34,35,52]. It was predicted that EHD2 and EHD4 oligomerize in ring-like structures around lipid tubules in a ATP-dependent way via the conserved nucleotide binding domain, causing the curvature of the membrane [13,14]. This oligomerization stimulates the EHDs intrinsic ATPase activity leading to ATP hydrolysis, which induces a conformational change that destabilizes the tubular membranes causing the scission of the vesicles containing the cargo, facilitating therefore the vesicular transport [12–14,44].

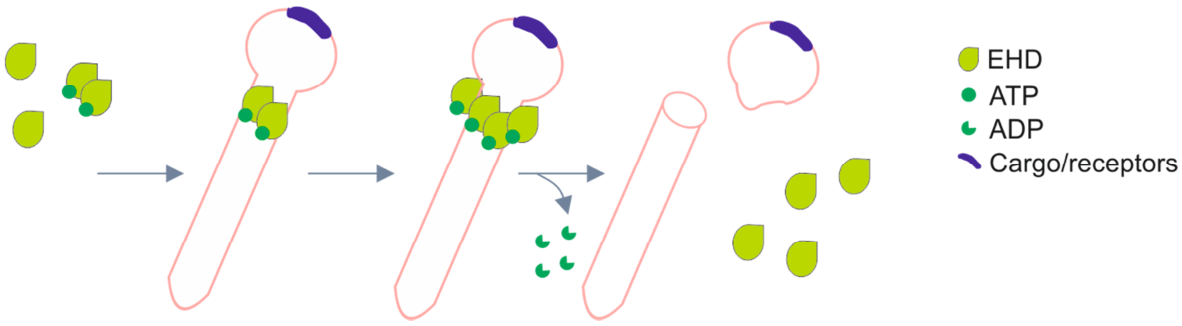

Figure 1.5: Proposed model of EHD proteins function.
EHD proteins are involved in vesicle scission. Upon binding of ATP and protein dimerization, a membrane binding site is formed, allowing the dimer to associate with tubular membranes. Association with the membranes leads to further oligomerization, which after ATP hydrolysis

destabilizes the tubular membranes causing vesicles scission. Modified from *Naslavsky et al, 2011* [12].

Although the four homologues present a high sequence similarity and apparently a similar mechanism of function, EHDs regulate different steps of endocytic traffic (Figure 1.6) [12]. However, several studies in mice and cell lines showed that loss of expression of one EHD can be partially compensated by other EHDs [9,53,54].

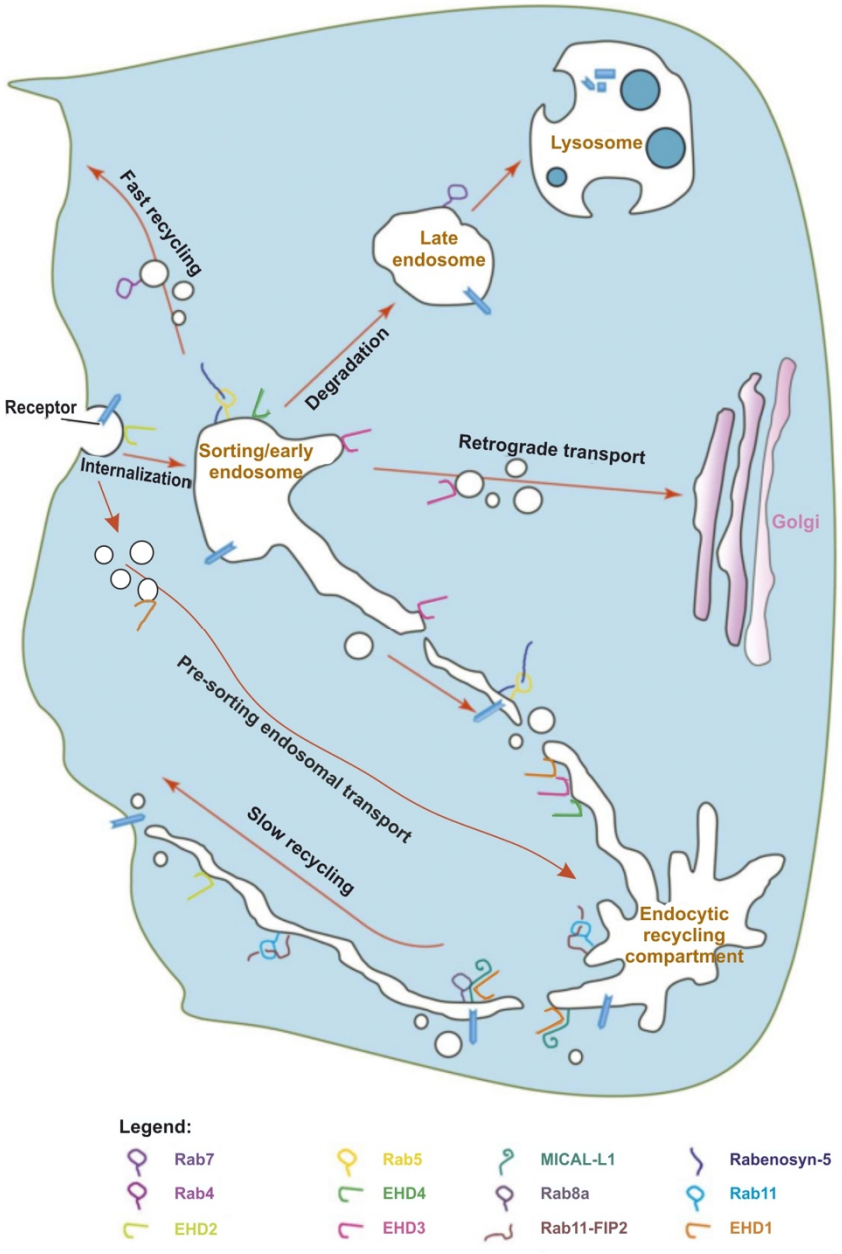

Figure 1.6: Regulation of endocytic transport by EHD proteins, Rabs and effectors. Internalized receptors can be directly transported to the endocytic recycling compartment in an EHD1-dependent process, or most commonly reach the early endosome where they are sorted. After sorting the receptors are trafficked through one of at least four pathways. Receptors designated for degradation are sorted to endosome microdomains containing EHD4, Rab5 and Rabenosyn-5 and transported to late endosomes and lysosomes. Other internalized proteins are transported from early endosome to the Golgi via an EHD3 and/or EHD1-dependent retrograde pathway. Receptors that recycle back to the plasma membrane can do it either by a direct (fast

recycling) or indirect (slow recycling) way. The fast recycling pathway from early endosome to plasma membrane is poorly understood and requires the function of Rab4. Alternatively, many receptors are first directed to the perinuclear endocytic recycling compartment and then shuttled to the plasma membrane. Slow recycling requires the sequential function of multiple regulators including Rab5, Rab11, Rab8a, their effectors (Rabenosyn-5, Rab11-FIP2 and MICAL-L1, respectively), and EHD proteins. Modified from *Naslavsky et al, 2011* [12].

1.2.3.1 EHD1

The most studied of the four mammalian EHD proteins is EHD1. It localizes to and is the best-known marker of large recycling tubules, whose diameter can reach up to 200 nm [37]. This protein is mainly associated with the recycling of membrane cargo from the EE to the ERC and back to the plasma membrane in a both clathrin-dependent [55] and independent [37] process.

The importance of EHD1 in the recycling process was shown for the first time when the presence of a dominant-negative construct with a point mutation near the EH domain resulted in the redistribution of the ERC and in a delayed recycling of the transferrin receptor by TRVb-1 cells [56]. So far, the involvement of EHD1 in the recycling of several receptors was already reported, such as the transferrin receptor [56], AMPA type glutamate receptors [57], major histocompatibility complex (MHC) class II molecules [58], integrin β_1 [59], cystic fibrosis transmembrane conductance regulator [55], insulin-regulated GLUT4 glucose transporter[33], G-protein-activated inwardly rectifying potassium channels [60], calcium-activated potassium channel KCa2.3 [61], CD59 [62] and Insulin-like growth factor 1 receptor [63]. Furthermore, many interaction partners were already assigned to EHD1, helping to unravel its role in different stages of the endocytic pathway. Some of the recognized partners are GTPase Regulator Associated with Focal adhesion kinase-1 (GRAF1) [64], MICAL-L1 [52,64], Syndapin2 [65], Rabenosyn [64], Rab11-FIP2 [35], Numb, SNAP29 [63], EHD3 [66] and EHD4 [67]. These interactions are established mainly through the already mentioned EH domain/NPF motif.

Recently, studies aiming to identify the differential roles of the EHD proteins showed that EHD1 is capable of membrane vesiculation, consistent with enhanced tubular recycling endosomes network observed upon EHD1 depletion [68]. Although EHD1 seems capable of direct interaction with tubular membranes, by preferentially binding to phosphatidylinositols via its EH domain [27], EHD1 interaction partners such as MICAL-L1 and Syndapin2 are essential for tubular recycling endosomes biogenesis. MICAL-L1 and Syndapin2 were shown to interact directly and to bind to a phosphatidic acid (PA), an essential lipid component of tubular recycling endosomes, recruiting afterwards EHD1 to the membrane [65]. In other immunoprecipitation studies using HeLa cells, it was observed that also GRAF1 is localized to a complex containing both MICAL-L1 and EHD1, and it seems to act synergistically with EHD1 to induce tubular recycling endosome vesiculation

in a semi-permeabilized cell system [64]. It was also reported that phosphatidyl-serine flipping by a recycling endosome-localized P_4-ATPase is required for the recruitment of EHD1, since the depletion of ATP8A1 impaired the asymmetric transbilayer distribution of phosphatidyl-serine in the recycling endosomes, leading to dissociation of EHD1 from these structures, and generation of aberrant endosomal tubules that appeared resistant to fission [69].

EHD1 is mainly known to mediate the recycling of internalized proteins from a pericentriolar ERC to the plasma membrane [32–34,37,55–57]. However, it was also reported the EHD1 involvement in the transport of receptors from EE to the ERC. Studies in cultured cells showed that the knockdown of connecdenn, a DENN domain-containing protein of neuronal clathrin-coated vesicles, or Rab35 disrupts recruitment of EHD1 to the EE and leads to an enlargement of the compartment [51]. More recently, it was also observed that EHD1 plays a role in the regulation of the trafficking of the glycosylphosphatidylinositol-anchored protein CD59 in a much earlier stage of the endocytic pathway, controlling the transport of CD59 from pre-sorting endosomes to the ERC in a protein kinase C-dependent manner [62].

In addition to its well documented role in the regulation of receptor recycling, EHD1 is also involved in the process of cell adhesion and migration. It was reported that EHD1 is required for the trafficking of Src — a protein tyrosine kinase known to mediate focal adhesion turnover, cell spreading and migration — to the plasma membrane and its activation [70]. Furthermore, the knockdown of EHD1 impaired Src activation and its localization to the cell periphery following treatment with growth factor [70].

Other studies in cultured cells revealed a role of EHD1 in neurite outgrowth. EHD1 was shown to regulate the endocytosis of the L1/neuron-glia cell adhesion molecule (NgCAM), a protein involved in axonal path-finding and guidance, axonal branching, and myelination in neurons [71]. It was also observed that active Rab35 coordinates MICAL-L1 and centaurin-β_2 at Arf6-positive endosomes in response to nerve growth factor stimulation, which induces neurite outgrowth of PC12 cells. The recruited MICAL-L1 and centaurin-β_2 then recruit EHD1 to the same compartment by functioning as a scaffold factor for EHD1 and as an inactivator of Arf6, respectively. This molecular relationship seems to be necessary for successful neurite outgrowth [72]. Furthermore, EHD1 was not only detected in both the gray and white matter of adult rat spinal, but also when using an acute spinal cord contusion injury model in adult rats, it was observed that EHD1 expression was low in the sham-operated adult rat spinal cords but was significantly up-regulated one day after injury [73]. These evidences are also in support of an involvement of EHD1 in neurite outgrowth.

EHD1 also regulates the internalization of the low density lipoprotein (LDL) receptor [74] and has been proposed as a modulator of insulin-like growth factor 1 receptor signaling [63].
Very recently, a new role of EHD1 in the regulation of mitochondrial fission was observed [75]. The EHD1 interaction with the retromer complex led to VPS35-mediated removal of inactive dynamin-related protein 1 (Drp1) — a protein required for mitochondrial division — from mitochondrial membranes. EHD1 depletion induced a static and elongated network of mitochondria in the cell [75].
Finally, in the last years, a new function of EHD1 and its homologue EHD3 in early ciliogenesis has been suggested [76]. Using retinal pigment epithelium (RPE) cells and zebrafish embryos, Lu and co-workers observed both EHD1 and EHD3 localization at preciliary membranes and ciliary pocket. They also showed that EHD-dependent membrane tubulation is essential for ciliary vesicle formation and assembly [76].
Whereas EHD1 was identified mainly as a gatekeeper to promote ERC-plasma membrane recycling of multiple receptors, it clearly has evolved to carry out additional endocytic functions in specific organelles and in specialized cells, becoming essential in several cell processes, such as migration and ciliogenesis.

1.2.3.1.1 Ehd1$^{-/-}$ mouse models

So far, several *Ehd1*$^{-/-}$ mice have been generated, producing more or less controversial data. One study, where the knockout was achieved by deletion of exon 1 of *Ehd1*, reported increased mortality, reduced body weight, and impaired testicular function in the knockout mice [77]. A more detailed evaluation of the testis revealed abnormal spermatogenesis in the seminiferous tubules and absence of mature spermatozoa in the epididymis of knockout males. Abnormal acrosomal development on round spermatids, clumping of acrosomes, misaligned spermatids and the absence of normal elongated spermatids were also observed [77]. Another study, that used the same knockout mouse to characterize the role of EHD1 in muscle development, showed that *Ehd1*$^{-/-}$ myoblasts displayed defective receptor recycling and mislocalization of key muscle proteins, such as caveolin-3 and Fer1L5 [78]. Loss of EHD1 also led to smaller muscles and myofibers *in vivo* [78]. In wildtype skeletal muscle EHD1 is localized at the transverse tubule, and EHD1 absence resulted in overgrowth of transverse tubule with increased vesicle accumulation in the skeletal muscle [78]. A third study on the same mouse revealed that EHD1 also seems to play a role in early ocular lens development [11]. *Ehd1*$^{-/-}$ mice exhibited a range of ocular defects, including microphthalm congenital cataracts, anophthalm nd aphakia [11]. A conditional *Ehd1* deletion in the ocular lens led to developmental defects that included thin epithelial layers, small lenses and absence of corneal endothelium, as well

as reduced lens epithelial proliferation, survival and aberrant corneal endothelial differentiation [11].

On the other hand, a work using a different *Ehd1*$^{-/-}$ mouse, generated by partial deletion of exon 3 and total deletion of exons 4 and 5, reported no significant difference in the phenotype of the knockout mouse when compared to the wildtype [54]. The knockouts showed a normal life span and no histological abnormalities. Only the *Ehd1*$^{-/-}$ embryonic fibroblasts demonstrated delayed recycling to the plasma membrane with accumulation of transferrin in the endocytic recycling compartment [54]. By comparison of all these reports it is possible that the *Ehd1* deletion in the second mouse model was only partial and that some functional EHD1 protein was still being expressed. However, a recent study also revealed that the severity of the phenotype in the *Ehd1*$^{-/-}$ mouse is dependent on the mouse strain [79]. The *Ehd1* deletion has shown to be embryonic lethal in mice on a predominantly C57BL6 background, but much less severe in mice with other backgrounds [79]. The *Ehd1*$^{-/-}$ embryos died at mid-gestation with a failure to complete key developmental processes including neural tube closure, axial turning and patterning of the neural tube. They also displayed short and stubby cilia on the developing neuroepithelium [79], which is in agreement with the studies in RPE cells and zebrafish embryos that showed a role of EHD1 in ciliogenesis [76].

1.2.3.2 EHD2

EHD2 is the homologue with the lowest sequence identity of the four and also the only one forming homo-oligomers [13], in contrary with the others EHDs that are capable of hetero-oligomerization [66,67]. Although EHD2 was the first of the four homologues to have its structure solved [13], its precise function on the regulation of endocytic transport remained unclear for many years.

The first identified interaction partner of EHD2 was the EH-domain-binding protein 1 (EHBP1) [80]. EHBP1 and EHD2 have been linked to internalization of receptors such as transferrin and GLUT4, potentially by linking clathrin-dependent endocytosis to filamentous actin via the EHBP1 CH domain [80]. Later studies provided evidence that EHD2 can also function redundantly with EHD1, namely in the transferrin recycling pathway. EHD2 localization not only overlaps with transferrin [8] but also its depletion, as well as EHD1 knockdown, leads to delayed transferrin recycling from the ERC [9]. Moreover, in myoblasts derived from mice lacking the EHD2 binding partner myoferlin, a delay in transferrin recycling was also observed [81]. In addition, EHD2 was shown to be involved in myoblast fusion [81].

Despite of being capable of vesiculating tubular recycling endosomes, Cai and co-workers provided evidence that EHD2 is unable of doing it *in vivo* [68]. Instead, EHD2 has been

associated with stabilization and constrainment of caveolae to the plasma membrane [82–84]. EHD2 interacts with Pacsin2 and Cavin1, which mediate EHD2 association with caveolae, and although it is not necessary for caveolae formation it is involved in caveolae turnover and stability [82]. Furthermore, using infrared reflection–absorption spectroscopy, it was observed that EHD2 is able to regulate caveolae dynamics via ATP-mediated oligomerization of an open state of the protein partially inserting into the membrane [83].

It is possible that EHD2 might be involved in receptor recycling in some tissues, but in others, such as adipocytes, EHD2 seems to play a more central role in receptor internalization [12].

Until now no *Ehd2*$^{-/-}$ mouse was generated to further study the physiological role of EHD2.

1.2.3.3 EHD3

EHD3 is the homologue sharing the highest sequence identity with EHD1 and, as previously mentioned, it was even shown by yeast two-hybrid analysis and immunoprecipitation of overexpressed EHDs, that these two paralogs are interaction partners [9,66]. However, contrary to EHD1, EHD3 does not appear to be a major player in the recycling pathway from the ERC to the plasma membrane. Studies in HeLa cells revealed that EHD3 depletion led to an impaired transport, with accumulation of cargo at peripheral EE failing to reach the ERC [35]. Adding to these findings, EHD3 was also shown to be involved in the EE-to-Golgi retrograde transport, since its knockdown resulted in aberrant Golgi morphology and function and delayed biosynthetic transport of lysosomal enzymes [85].

Unlike EHD1, which is primarily responsible for tubular recycling endosomes vesiculation, EHD3 is a membrane-tubulating protein in charge of recycling endosomes stabilization [68,86]. Bahl and co-workers [86] hypothesized that EHD3 binds to MICAL-L1 [52] and Syndapin2 [30] via NPF-EH interactions stabilizing these two proteins on the tubular recycling endosomes membranes, preventing their dissociation and degradation. Following cargo sorting, it is suggested that EHD3 is replaced by EHD1 resulting in vesicles fission [86]. The mechanism that triggers the EHD switch remains unknown but it is very likely to be related with *in vivo* modifications, such as EHD3 SUMOylation [87] and desumoylation, as well as specific signaling triggers through receptors [70,88].

As mentioned before, as well as EHD1, EHD3 was also found to be involved in ciliogenesis, being primarily localized at the ciliary pocket membrane and essential for reorganization of the M-centriole and association of ciliary vesicles, displaying a somehow overlapping function with EHD1 [76].

1.2.3.3.1 Ehd3$^{-/-}$ *mouse models*

Studies in *Ehd3*$^{-/-}$ mice showed cardiac problems, such as arrhythmias and blunted response to adrenergic stimulation together with reduced expression of Na/Ca exchanger (NCX1), L-type Ca-channel type 1.2 (Cav1.2) and associated functions [89,90].

Due to EHD3 specific expression in the glomerular endothelium in the kidney, the *Ehd3*$^{-/-}$ mouse was investigated in order to assess EHD3 role in renal development and pathology [91]. *Ehd3*$^{-/-}$ animals showed no clear phenotype, and exhibited no proteinuria or glomerular pathology. However, the expression of EHD4 was increased in the glomerular endothelium of *Ehd3*$^{-/-}$ mice, which suggested functional compensation [91]. Therefore, George and co-workers generated a *Ehd3*$^{-/-}$; *Ehd4*$^{-/-}$ mouse, that displayed a smaller body size, possessed smaller and paler kidneys, was proteinuric and died between 3–24 weeks of age [91]. The analysis of *Ehd3*$^{-/-}$; *Ehd4*$^{-/-}$ kidneys showed thrombotic microangiopathy-like glomerular lesions including thickening and duplication of glomerular basement membrane, endothelial swelling and loss of fenestrations. Podocyte foot process and mesangial marker expression were also found abnormal. Finally, vascular endothelial growth factor receptor 2 (VEGFR2) expression and localization in the glomerular endothelial was altered in the double knockout mice, suggesting that EHD-mediated endocytic traffic of key surface receptors such as VEGFR2 is essential for physiological control of glomerular function [91].

1.2.3.4 EHD4

EHD4, whose crystal structure was very recently solved [14], is, after EHD3, the homologue with highest sequence similarity with EHD1. Its function has been associated with the regulation of receptor transport from EE to the ERC and the late endocytic pathway [9,67]. Depletion of EHD4 expression in HeLa cells leads to the generation of enlarged early endosomal structures and accumulation of cargo destined for degradation in the EE [67].

It was also observed in cells that EHD4 is able to interact with EHD1, suggesting a somehow coordinated involvement in the regulation of receptor transport along the early endosome to endocytic recycling compartment axis [9,67]. This observed oligomerization between EHD4 and EHD1 seems to be important in neurons, since balanced levels of EHD1–EHD4 are necessary for proper endocytosis of L1/NgCAM [71]. Furthermore, in neuronal cells EHD4 was found to be involved in the internalization of the TrkA and TrkB nerve growth factors [92,93] and an active fragment of Nogo-A, a potent myelin-associated inhibitor for axonal growth, regeneration, and plasticity in the adult central nervous system [94].

Cadherin 23, a transmembrane protein localized near the tips of hair cell stereocilia in the mammalian inner ear, was also identified as an EHD4 binding partner and interestingly

the co-immunoprecipitation was found to be calcium-sensitive [10], which suggests a role of EHD4 in the auditory pathway.

1.2.3.4.1 Ehd4$^{-/-}$ mouse models

In order to further understand EHD4 function, some *Ehd4*$^{-/-}$ mouse models have already been generated. Due to EHD4 interaction with Cadherin 23, the role of EHD4 in hearing was investigated and compound action potentials were measured in *Ehd4*$^{-/-}$ mice. Although knockout mice displayed normal hearing sensitivity, analysis of mouse cochlear lysates revealed a 2-fold increase in EHD1, but no increase in EHD2 or EHD3, in *Ehd4*$^{-/-}$ cochleae compared with wildtype, suggesting that a compensatory increase of EHD1 may explain the absence of hearing defect in the knockouts [10].

In another *Ehd4*$^{-/-}$ mouse model, young male knockouts showed a 50% reduction in testis weight, progressive reduction in seminiferous tubule diameter, dysregulation of seminiferous epithelium and head abnormalities in elongated spermatids. As consequence, lower sperm counts and reduced fertility were observed [53]. Moreover, in adult mice, *Ehd4* deletion altered the levels of other EHD proteins in the testis in an age-dependent manner. High levels of EHD1 in adult *Ehd4*$^{-/-}$ testis were detected, and they seemed to compensate for lack of EHD4 and prevent the development of severe fertility defects [53]. These results suggest a role of EHD4 and EHD1 in the proper development of germ cells and implicate that EHD protein-mediated endocytic recycling is an important process in germ cell development and testis function.

Recently, the role of EHD4 in the kidney was studied using *Ehd4*$^{-/-}$ mice. EHD4 was found to be differentially expressed along the nephron segments with the highest expression in the inner medullary collecting duct. It was observed that knockout mice excreted a higher volume of more dilute urine than control mice while maintaining a similar plasma osmolality, suggesting that EHD4 plays a role in renal water handling [95]. Furthermore, localization of both aquaporin 2 (AQP2) and phospho-S256-AQP2 (pAQP2) in the renal inner medullary principal cells appeared more dispersed, and the intensity of apical membrane staining for AQP2 was significantly reduced in knockout mice compared to wildtype mice in baseline conditions, suggesting an important role of EHD4 in the trafficking of AQP2 [95].

1.2.4 EHD proteins and human diseases

Until today no direct link has been established between a human disease and the EHD proteins. However, alterations in the expression level of the different homologues were observed in some diseases. Furthermore, EHDs were described as being involved in the recycling of some disease-causing proteins (Table 1.2).

Table 1.2: Relationship of EHD proteins with human disease. Modified from *Naslavsky et al, 2011* [12].

EHD Protein	*Disease or condition*	*Transcript or protein*	*Phenotype/Function*	*Fold increase or decrease*	*Reference*
EHD1	Pseudoexfoliation glaucoma	–	Enhanced levels of serum antibodies	–	96
	Apergillus fumigatus infection	Transcript	Enhanced EHD1 expression in monocytes	2-fold increase	97
	Metastic ability of well-differentiated pancreatic endocrine neoplasms	Transcript	Decrease expression	3-fold decrease	98
	Sickle-cell disease	Protein	Decrease expression	–	99
	Aeromonas hydrophila cytotoxic enterotoxin induced-genes	Transcript	Increased expression in macrophages	4-fold increase	100
	Plasmodium falciparum infected erythrocytes	Transcript	Increased expression in erythrocytes	5-fold increase	101
	Prostate cancer	Protein	Secreted from exosomes of prostate cancer cells	–	102
	Cutaneous T cell lymphoma	Transcript	Increased expression in lesion	2-fold increase	103
	Breast cancer	Protein	Increased expression in primary breast cancer cells	2-fold increase	104
	Metastasis in non-small cell lung cancer	Transcript	Increased expression in non-small cell lung cancer tissue	6-fold increase	105
EHD1,-3	Alzheimer's disease	–	Involved in β-secretase level and transport in axons	–	106
EHD1,-4	Glioma	–	Gene loss proposed	–	107
EHD2	Diabetes mellitus-associated bladder dysfunction	Protein	Decreased expression	2-fold decrease	108
EHD3	Oral squamous cell carcinoma	Transcript	Decreased expression	12-fold decrease	109

	Small-cell lung cancer	Transcript	Increased expression	_	110
	Acute myeloid leukemias	_	Gene methylation	_	111
	Glioma	Transcript	Low or no expression	_	112
EHD4	Systemic onset juvenile idiopathic arthritis	Transcript	Increased expression	1-fold increase	113

1.3 The Kidney and EHD Proteins

The kidneys are a pair of organs located at the level of the eleventh thoracic vertebra to the second lumbar vertebra in the retroperitoneal space. The kidneys are responsible for water, electrolyte and acid-base balance in the body, regulation of the blood pressure, production of hormones, like Erythropoietin and Renin, and excretion of toxic substances, such as metabolic end products. Macroscopically, the kidney consists of a connective tissue capsule, the cortex and the medulla, the papilla and the pelvis. The basic and functional unit of the kidney is the nephron (Figure 1.7). Each kidney is composed by approximately 1 million nephrons.

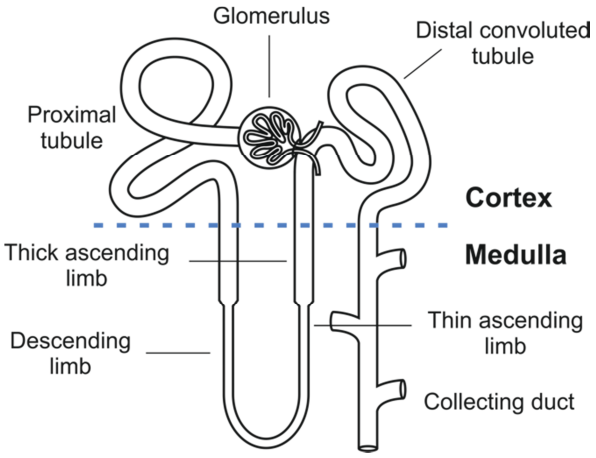

Figure 1.7: Schematic model of a nephron.
The nephron is the functional unit of the kidney. It consists of several tubular segments with different functions, beginning at the glomerulus, followed by the proximal tubule, thin descending limb, thin ascending limb, thick ascending limb, distal convoluted tubule, connecting tubule and collecting duct.

The nephron starts with the glomerulus, which lies in the renal cortex and is the place where the blood is filtered. The glomerulus consists of two major entities, namely the network of capillaries that transport the blood to the site and the enlarged head of the nephron that collects the filtered fluid, known as Bowman's capsule. The capillaries are formed by a thin layer of endothelial cells that is closely associated with the visceral epithelium separated by a basement membrane. The side of the basement membrane that faces outwards from the capillary is lined with cells known as podocytes and their foot processes. They control the filtration of particles from the capillary lumen into Bowman's

space. Molecules until 6 kDa are freely filtered, the filtration capacity for particles up to 50–60 kDa is reduced and particles larger than 60 kDa are no longer filtered. The charge of the particles also determines their filtration ability, since podocyte foot processes and the basement membrane have a negatively charged coat, called glycocalyx, that limits the filtration of negatively charged molecules.

The fluid that is filtered enters then the proximal tubule, which is made up of cuboidal epithelial cells that contain a brush border on the apical side. Here, essential substrates such as glucose, phosphate, bicarbonate and amino acids are reabsorbed as well as $^{2}/_{3}$ of the filtered sodium, chloride and water. Additionally, filtered low-molecular-weight proteins are reabsorbed in the proximal tubule. Reuptake of proteins is mainly controlled by two receptors, megalin and cubilin [114]. The receptors fulfil their task by receptor-mediated endocytosis mediating delivery of their ligands to the lysosomes of the proximal tubule, while they undergo recycling themselves [115]. In cases of some renal diseases that are characterized by proteinuria and defective tubular reuptake of filtered proteins, it has been shown that renal megalin expression is reduced [116]. Also in the absence of megalin, the mice displayed a tubular resorption deficiency and excretion of low-molecular-weight plasma proteins in the urine (low-molecular-weight proteinuria) [117].

After the filtrate leaves the proximal tubule it enters the loop of Henle. It consists of the descending limb, thin ascending limb and thick ascending limb. The morphology of the loop of Henle allows the so called counter current mechanism that is a prerequisite for producing concentrated urine. In the thin limbs, reabsorption of water (descending limb) and salt (ascending limb) is mainly of passive nature. The thick ascending limb energizes the counter current mechanism and is responsible for some 25% of the filtered sodium. Afterwards, in the distal convoluted tubule, sodium, chloride, magnesium and calcium are reabsorbed transcellularly. The final segments of the nephron are the connecting tubule and the collecting duct. These segments are responsible for the fine tuning of sodium and water reabsorption as well as potassium secretion. Moreover, urinary pH is adjusted to its final value by transport of bicarbonate and protons in intercalated cells.

Some studies have already addressed the localization of the EHD proteins in the kidney: EHD2 was proposed to be mainly localized at the interlobular arteries [91], EHD3 at the glomerular endothelium [91], EHD4 in the peritubular capillaries [91] and collecting duct [95] and EHD1 in the brush border epithelium of proximal tubules [91]. However, the role and importance of EHD1 in the kidney is still unknown and no renal phenotype has been reported for the *Ehd1*$^{-/-}$ mouse models so far.

1.4 The Inner Ear and EHD Proteins

In the inner ear the sensory organs for hearing and balance are localized. The semicircular canals are part of the balance system and the cochlea is the hearing part of the inner ear.

The cochlea is a bony structure shaped like a helix and filled with two fluids, endolymph and perilymph. The Organ of Corti is the sensory receptor system inside the cochlea which holds the hair cells and the nerve receptors for hearing (Figure 1.8). In the cochlea sound waves are transformed into electrical impulses, which are then sent on to the brain. The mechanical energy from movement of the middle ear bones pushes in a membrane (the oval window) in the cochlea. This force leads to movement of the cochlea's fluids that in turn stimulates the hair cells. Individual hair cells respond to specific sound frequencies (pitches) so that, depending on the pitch of the sound, only certain hair cells are stimulated. Signals from these hair cells are transformed into nerve impulses and then sent to the brain via the auditory nerve.

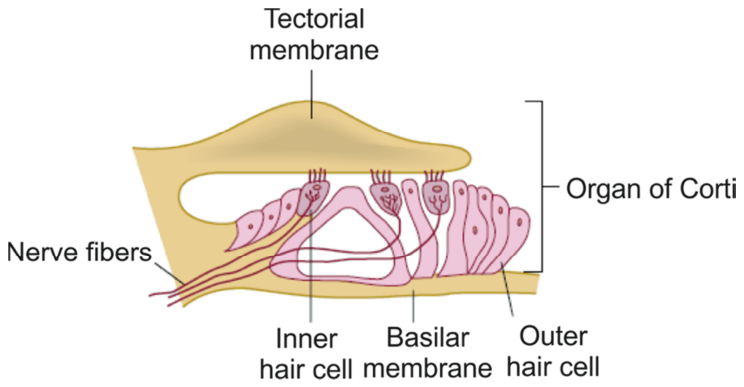

Figure 1.8: Schematic model of the Organ of Corti.
The Organ of Corti is the sensory receptor in the cochlea and where the sound waves are transformed into electrical impulses. It is composed by a tectorial membrane, inner and outer hair cells and a basilar membrane. Modified from https://michaelsoud.wikispaces.com/Different+Frequencies+and+the+Sound+Shadow.

The range of frequencies that can be heard differs from organism to organism. The human range is commonly between 20–16000 Hz, while for mice is 2000–90000 Hz [118].

Until know, not much is known about EHD proteins in the inner ear. It was only reported that EHDs are expressed in the cochlea and that EHD4 is able to interact with Cadherin 23 (CDH23), a transmembrane protein localized near the tips of hair cell stereocilia in the mammalian inner ear, in cochlear hair cells [10]. As previously mentioned, in *Ehd4*$^{-/-}$ mice cochlea a compensation of the loss of EHD4 by increased expression of EHD1 was proposed [10]. However, a specific role of EHD1 in the auditory system that could explain the hearing loss of our patients is not yet described.

1.5 The Testis, Epididymis and EHD proteins

The testis and the epididymis are components of the reproductive system. The primary functions of the testis are to produce sperms, in a process called spermatogenesis, and to produce androgens, such as testosterone. The presence of both testosterone and follicle-stimulating hormone (FSH) is necessary to support spermatogenesis. The testis consists of very fine coiled tubes known as seminiferous tubules. In these tubules spermatogenesis occurs, during which spermatogonia undergo mitotic divisions and differentiate into spermatocytes, which in turn undergo two meiotic divisions, differentiate to round spermatids that later form elongated spermatids and are released from Sertoli cells during spermiation, resulting ultimately in spermatozoa formation (Figure 1.9). In the seminiferous tubule, the referred Sertoli cells and the myoid cells are also present. The Sertoli cells support the development of germ cells and they produce inhibin, an inhibitor of FSH secretion. The myoid cells surround the seminiferous tubules. Finally, in the interstitial space the Leydig cells are localized. They are responsible for the production and secretion of testosterone and other androgens.

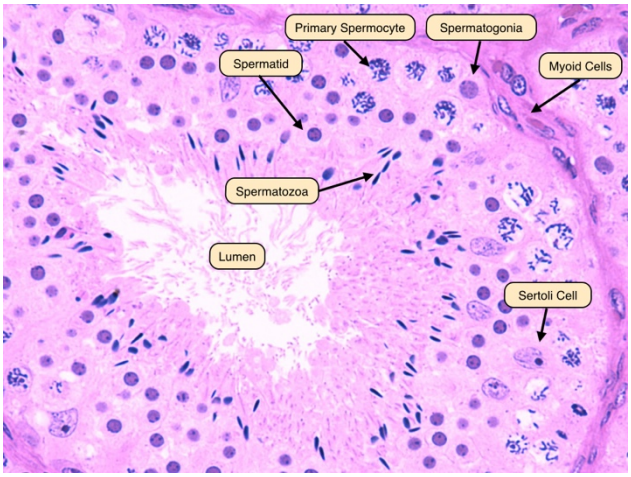

Figure 1.9: Seminiferous tubule.
The seminiferous tubule is the basic unit of the testis. In these tubules the spermatogenesis takes place, leading to the development of spermatogonia into spermatozoa. From http://medcell.med.yale.edu/histology/male_reproductive_system_lab/spermatogenesis.php.

The developing spermatozoa travel then through the seminiferous tubule to the rete testis and efferent ducts until they reach the epididymis. The epididymis can be divided into three regions: the head, the body and the tail. Spermatozoa formed in the testis enter the head of the epididymis, progress to the body and finally reach the tail region, where they are stored. The spermatozoa are not mature when they reach the epididymis, lacking motility and the ability of fertilization. It is in the epididymis that the spermatozoa undergo a maturation processes needed to acquire the lacking abilities.

As previously referred, studies in *Ehd1*$^{-/-}$ and *Ehd4*$^{-/-}$ mice reported a role of these proteins in spermatozoa development [53,77]. The absence of EHD1 led to male infertility due to abnormal spermatogenesis and impaired acrosomal development in spermatids [77]. The loss of EHD4 resulted in reduction of seminiferous tubule diameter, dysregulation of seminiferous epithelium and head abnormalities in elongated spermatids in young mice [53]. Interestingly, an increase in EHD1 levels in the adult *Ehd4*$^{-/-}$ testis was observed that probably functionally compensated for the lack of EHD4 and prevented the development of severe fertility defects [53].

2. Objectives

Our co-worker Robert Kleta (University College London) has examined 6 patients with tubular proteinuria (1–2 g per day) and hearing loss at a high frequency range. Using linkage analysis and sequencing, Robert Kleta identified in all patients a homozygous mutation leading to a single amino acid substitution (R398W) in the linker region of the C-terminal Eps15 homology domain (EHD1) 1 protein. In mammals, EHD1 belongs to a family of four homologous proteins — EHD1–4 — that are presumably associated with the recycling of membrane cargo from the endocytic recycling compartment to the plasma membrane by fission of intracellular vesicles.

The major aims of this dissertation were to gain novel insights into the physiological role of EHD1 in several tissues and to elucidate the molecular and pathomechanisms leading to this EHD1-associated human disease. To this end, the phenotype of an *Ehd1*$^{-/-}$ mouse with the focus on the inner ear and kidney was characterized and the consequences of the R398W mutant in a proximal tubular cell model were assessed. Due to previous reports on *Ehd1*$^{-/-}$ mice infertility and abnormal spermatogenesis [77] as well as on defective eye development [11], the testicular and ocular phenotypes were also addressed.

Histochemistry and microscopy were used to investigate the histology of the cochlear, renal and testicular tissues of the *Ehd1*$^{-/-}$ mice. The mice hearing ability was assessed by auditory brainstem response measurements. The kidney function of the *Ehd1*$^{-/-}$ mice was analyzed by protein overload assays *in vivo* and live-imaging on proximal tubular protein reabsorption. Finally, two tetracycline-inducible LLC-PK1 cell lines expressing wildtype (WT) and mutant (R398W) EHD1 were analyzed in order to understand the cellular effects of the EHD1 mutation found in patients.

3. Materials and Methods

3.1 Materials

3.1.1 Instruments

Instruments	Producer
Autoclave	Tuttnauer 2540ELC, biomedis GmbH, Gießen, Germany
Camera CCD 2k (for electron microscope)	Troendle, Moorenweis, Germany
Camera CMOS 4k F416 (for electron microscope)	TVIPS, Gauting, Germany
CED 3505 programmable attenuator	Cambridge Electronic Division Limited, Cambridge, UK
CED micro 1401 data acquisition unit	Cambridge Electronic Division Limited, Cambridge, UK
Confocal Microscope LSM 710	Zeiss, Jena, Germany
CryoStar NX70	Thermo Fisher Scientific, Dreieich, Germany
Fusion-FX7- Spectra	Vilber Lourmat, Eberhardzell, Germany
Gas mixer for Isoflurane-Vaporizer	MFI Föhr Medical Instruments GmbH, Seeheim, Germany
Incubator	Heraeus Instruments, Osteode, Germany
Inverted Microscope Observer Z.1	Zeiss, Jena, Germany
Inverted Microscope Axiovert 200	Zeiss, Jena, Germany
Isoflurane-Vaporizer	MFI Föhr Medical Instruments GmbH, Seeheim, Germany
Laminar Flow	Thermo Fisher Scientific, Dreieich, Germany
Light-Cycler LC480	Roche, Mannheim, Germany
Microcentrifuge	Hettich, Tuttlingen, Germany
Millicell® ERS-2 Voltohmmeter	Merck, Darmstadt, Germany
NanoDrop 2000c Spectrophotometer	Thermo Fisher Scientific, Dreieich, Germany
NanoDrop 3300 Fluorospectrometer	Thermo Fisher Scientific, Dreieich, Germany
NOVOstar Microplate reader	BMG Labtech, Ortenberg, Germany
Microtome (Rotary microtome RM2165)	Leica, Wetzlar, Germany
Mini-PROTEAN Tetra Vertical Electrophoresis Cell	Bio-Rad, Munich, Germany
Mini Trans-Blot Cell	Bio-Rad, Munich, Germany
Paraffin incubator	Modell 300, Memmert, Schwabach, Germany
Perfusor	Precidor 902681, Infors AG, Bottmingen, Switzerland
pH electrode	Schott Geräte, Mainz, Germany
PowerPac Basic Power Supply	Bio-Rad, Munich, Germany
Roller pump	Ismatec SA., Zürich, Switzerland
Scale (EK-600)	A&D Instruments Ltd, Tokyo, Japan
Surgery instruments	FST, Bad Oeynhausen, Germany

Sound-attenuated chamber	Industrial Acoustics, Niederkrüchten, Germany
Speaker (for f-ABR measurement)	SinusLive neo 25S, pro hifi, Kaltenkirchen, Germany
Thermomixer 5436	Eppendorf GmbH, Hamburg, Germany
Transmission electron microscope EM902	Zeiss, Oberkochen, Germany
Transmission electron microscope JEM-2100F	JEOL, Tokyo, Japan
Warm plate for paraffin sections	HI 1220, Leica, Wetzlar, Germany
Warm table for surgeries	Dr. J. Barhanin, Nice, France
Water bath	Modell W13, Haake, Karlsruhe, Germany

3.1.2 Laboratory material

Products	**Producer**
0,5 ml Insulin-syringe	BD Micro-Fine+, BD Consumer Healthcare, Heidelberg, Germany
96-well PCR-Plate, white	Nerbe Plus GmbH, Winsen/Luhe, Germany
96-well plate	Nuclon Surface, Nunc A/S, Roskilde, Denmark
Cell culture flasks (T-25, T-75)	Nuclon Surface, Nunc A/S, Roskilde, Denmark
Cell Culture Inserts, 0,4µm PCF, 12mm diameter	Merck Millipore, Darmstadt, Germany
Cell culture plates (6-well, 12-well, 24-well)	Nuclon Surface, Nunc A/S, Roskilde, Denmark
Cell scraper	TPP Techno Plastic Products AG, Trasadingen, Switzerland
Coverslips	A. Hartenstein GmbH, Würzburg, Germany
DePeX mounting medium	Serva Electrophoresis GmbH, Heidelberg, Germany
Eppendorf microplestle for 1,2 – 2 mL tubes	A. Hartenstein GmbH, Würzburg, Germany
Eppendorf Tubes (0,2 ml, 0,5 ml, 1,5 ml, 2 ml)	Eppendorf AG, Hamburg, Germany
Epoxy embedding medium	Sigma, Taufkirchen, Germany
Falcon tubes (15 ml, 50 ml)	Greiner bio-one, Frickenhausen, Germany
Filter paper	GE Healthcare Life Sciences, Buckinhamshire, UK
GeneRuler™ DNA Ladder (50 bp, 100 bp, 1 kb)	MBI Fermentas GmbH, St. Leon-Rot, Germany
Latex gloves	Kimberly-Clark, Roswell, USA
Light-Cycler Capillaries	Roche, Mannheim, Germany
Millex-GP Syringe Filter Unit, 0.22 µm, polyethersulfone, 33 mm, gamma sterilized	Merck Millipore, Darmstadt, Germany
Mortar	Rosenthal Technik, Tostedt, Germany
Nanosep Centrifugal	VWR International, Darmstadt, Germany
Non-fluorescent Glycergel mounting medium	DakoCytomation, Dakato North America Inc., Carpinteria, USA
Pasteur pipettes	Brand, Wertheim, Germany

Millicell® Cell Culture Inserts, 0,4 µm	Merck, Darmstadt, Germany
Pestle	Rosenthal Technik, Tostedt, Germany
Petri dishes (p35, p60, p100 mm)	Nuclon Surface, Nunc A/S, Roskilde, Denmark
Pipette tips (10 µl, 200 µl, 1000 µl)	Sarstedt, Nümbrecht, Germany
Polysine microscope adhesion slides	Kindler, Freiburg, Germany
Polyvinylidene difluoride (PVDF) membrane	GE Healthcare GmbH, Freiburg, Germany
Serological Pipettes	Nerbe Plus GmbH, Winsen/Luhe, Germany
Tissue cassettes for paraffin blocks	A. Hartenstein GmbH, Würzburg, Germany
Tissue Tek OCT-Medium	Sakura Finetek Europe B.V., Zoeterwoude, Netherlands

3.1.3 Substances

Products	**Producer**
0,9% NaCl isotonic solution	B. Braun Melsungen AG, Melsungen, Germany
1,4-Dithiothreitol (DTT)	Sigma, Taufkirchen, Germany
2-Methylbutane	Carl Roth GmbH + Co. KG, Karlsruhe, Germany
2x Laemmli Sample Buffer	Bio-Rad, Munich, Germany
4x Laemmli Sample Buffer	Bio-Rad, Munich, Germany
Acetic acid (glacial)	Merck, Darmstadt, Germany
Agarose	AppliChem, Darmstadt, Germany
Albumin-FITC	Sigma, Taufkirchen, Germany
Ammonium acetate	Sigma, Taufkirchen, Germany
Ammonium persulfate	Sigma, Taufkirchen, Germany
Bradford Protein Assay	Bio-Rad, Munich, Germany
BSA (Albumin from bovine serum)	Sigma, Taufkirchen, Germany
BSA (albumin from bovine serum)-Alexa Fluor 594	Thermo Fisher Scientific, Dreieich, Germany
$CaCl_2$	Carl Roth GmbH + Co. KG, Karlsruhe, Germany
Chloroform	Sigma, Taufkirchen, Germany
Citric acid monohydrate	Sigma, Taufkirchen, Germany
Coomassie® Brilliant Blue R-250	Merck, Darmstadt, Germany
Creatinine	Sigma, Taufkirchen, Germany
Cresyl violet acetate	Merck, Darmstadt, Germany
D-Mannitol	Fluka Chemie GmbH, Buchs, Switzerland
D-Potassium gluconate	Sigma, Taufkirchen, Germany
EDTA	Sigma, Taufkirchen, Germany
EGTA	Sigma, Taufkirchen, Germany
Eosin Y	Abcam, Cambridge, UK
Ethanol	J. T. Baker, Deventer, Netherlands
FCS (Fetal Calf Serum)	Gibco Cell Culture Systems - Invitrogen, Karlsruhe, Germany
FITC–Dextran 500 kDa	Sigma, Taufkirchen, Germany

Glucose	Merck, Darmstadt, Germany
Glutaraldehyde	Sigma, Taufkirchen, Germany
Glycerol	Sigma, Taufkirchen, Germany
Glycine	Merck, Darmstadt, Germany
Heparin	Liquemin N 25000, 5 ml, Roche, Mannheim, Germany
HEPES	AppliChem, Darmstadt, Germany
IGEPAL CA-630	Sigma, Taufkirchen, Germany
Inulin-FITC	Sigma, Taufkirchen, Germany
Isoflurane	Baxter Deutschland GmbH, Unterschleißheim, Germany
Isopropanol	Merck, Darmstadt, Germany
K_2HPO_4	Merck, Darmstadt, Germany
$K_3[Fe(CN)_6]$	Merck, Darmstadt, Germany
$K_4[Fe(CN)_6]$	Sigma, Taufkirchen, Germany
KCl	Merck, Darmstadt, Germany
Ketamine 100mg/mL	Sigma, Taufkirchen, Germany
$KH_2PO_4*3H_2O$	Merck, Darmstadt, Germany
L-Glutamine, 200 mM (100x)	Gibco Cell Culture Systems - Invitrogen, Karlsruhe, Germany
Mayer's hemalun solution	Carl Roth GmbH + Co. KG, Karlsruhe, Germany
Methanol	Merck, Darmstadt, Germany
$MgCl_2*6H_2O$	Merck, Darmstadt, Germany
$MgSO_4*7H_2O$	Merck, Darmstadt, Germany
Na^+-Pyruvate, 100 mM solution	Sigma, Taufkirchen, Germany
$Na_2HPO_4*2H_2O$	Merck, Darmstadt, Germany
NaCl	Merck, Darmstadt, Germany
$NaH_2PO_4*H_2O$	Merck, Darmstadt, Germany
Nonfat-dried milk	AppliChem GmbH, Darmstadt, Germany
Opti-MEM™, Reduced Serum Medium	Thermo Fisher Scientific, Dreieich, Germany
OsO_4	Sigma, Taufkirchen, Germany
Osteosoft®	Merck, Darmstadt, Germany
Paraffin	Paraplast-Plus Paraffin, Sherwood, St. Louis, USA
Paraformaldehyde	Merck, Darmstadt, Germany
Penicillin-Streptomycin solution	1000 I.E./ml Pen G, 10000 µg/ml Strep.-Sulfat, Gibco Cell Culture Systems - Invitrogen, Karlsruhe, Germany
Periodic acid	Thermo Fisher Scientific, Dreieich, Germany
Picric acid	Sigma, Taufkirchen, Germany
Pierce™ Protein G Agarose	Thermo Fisher Scientific, Dreieich, Germany
Polyethylene glycol sorbitan monolaurate (Tween 20)	Sigma, Taufkirchen, Germany
Precision Plus Protein™ Dual Color Standards	Bio-Rad, Munich, Germany
Protease Inhibitor Cocktail Set III, EDTA-Free	Merck, Darmstadt, Germany
Protein A Sepharose®	Abcam, Cambridge, UK

Restore Western Blot Stripping Buffer	Thermo Fisher Scientific, Dreieich, Germany
Rompun (xylazine) 100mg/mL	Bayer Animal Health, Monheim, Germany
Rotiphorese® Gel 30 (37,5:1) (30% Acrylamide)	Carl Roth GmbH + Co. KG, Karlsruhe, Germany
RPMI 1640 medium, L-Glutamine	Thermo Fisher Scientific, Dreieich, Germany
Schiff's reagent	Sigma, Taufkirchen, Germany
SDS (sodium dodecyl sulfate)	Merck, Darmstadt, Germany
Sodium acetate	Merck, Darmstadt, Germany
Sodium azide	Sigma, Taufkirchen, Germany
Sodium cacodylate trihydrate	Sigma, Taufkirchen, Germany
Sodium citrate-dihydrate	Merck, Darmstadt, Germany
Sodium deoxycholate	Sigma, Taufkirchen, Germany
Sucrose	Merck, Darmstadt, Germany
TEMED 99%, for electrophoresis	Carl Roth GmbH + Co. KG, Karlsruhe, Germany
Transferrin from Human Serum, Alexa Fluor™ 555 Conjugate	Thermo Fisher Scientific, Dreieich, Germany
Tris-Hydrochloride	Merck, Darmstadt, Germany
Triton X-100	Sigma, Taufkirchen, Germany
TRIzol™ Reagent	Thermo Fisher Scientific, Dreieich, Germany
Trypsin-EDTA (10x) solution	0,5% Trypsin, 5,3 mM EDTA, Gibco Cell Culture Systems - Invitrogen, Karlsruhe, Germany
Western Blotting Luminol Reagent	Santa Cruz, Heidelberg, Germany
X-Gal (5-Bromo-4-chloro-3-indolyl β-D-galactopyranoside)	Sigma, Taufkirchen, Germany
Xylol	Merck, Darmstadt, Germany
β_2-Microglobulin, human, Recombinant, *E. coli*	Merck Millipore, Darmstadt, Germany
β-Mercaptoethanol	Merck, Darmstadt, Germany

3.1.4 Enzymes, Kits

Product	**Producer**
Alexa Fluor 546 Protein Labeling Kit	Thermo Fisher Scientific, Dreieich, Germany
DNAse I (RNAse-Free DNAse Set)	Quiagen, Hilden, Germany
dNTP-Mix	MBI Fermentas GmbH, St. Leon-Rot, Germany
M-MLV Reverse Transcriptase	Promega, Madison, Wisconsin, USA
M-MLV Reverse Transcriptase Buffer (5x)	Promega, Madison, Wisconsin, USA
Protease (from Streptomyces griseus)	Sigma, Taufkirchen, Germany
Random Hexamer Primer (100 µM)	MBI Fermentas GmbH, St. Leon-Rot, Germany
REDTaq® ReadyMix™ PCR Reaction Mix	Sigma, Taufkirchen, Germany
RNAse Inhibitor	Peqlab Biotechnologie GMBH, Erlangen, Germany
NucleoSpin RNA kit	Macherey-Nagel, Düren, Germany
SYBR® Green PCR Kit	Roche, Mannheim, Germany

3.1.5 Software

Product	Producer
CorelDraw Graphics Suite X7	Corel Corporation, Ottawa, Canada
ImageJ V1.37c	Wayne Rasband, NIH, USA
Origin V94E	OriginLab Corporation, Northampton, USA
ZEN Pro V2.3	Zeiss, Jena, Germany

3.1.6 Oligonucleotides

All oligonucleotides were produced by Invitrogen, Karlsruhe, Germany.

Gene	Organism	Primer	Sequence	Annealing-T.
Ehd1	Mus musculus	sense antisense	CATCAGCCGAGGTTATGAC CTGAGATGTCCAGCTTGTG	57°C
Ehd2	Mus musculus	sense antisense	CCTTCCGCAAACTCAACC CGTGTCGATGATGCTGATG	57°C
Ehd3	Mus musculus	sense antisense	GCCTTCCTGAACAGGTTTG GGCTGATCCTCTGCTTCTC	57°C
Ehd4	Mus musculus	sense antisense	GGCAAGACCACGTTCATC GTTGGCTCTGGACCAATTC	57°C
Lrp2 (Megalin)	Mus musculus	sense antisense	CAGTCAGTGGCCAAGAATG CAGTCTCTGGTCCCATCAC	63°C
Cubn (Cubilin)	Mus musculus	sense antisense	TGATGGTACCCGGATTAGAC GTTTCCCTCCTCCGTAGTC	63°C
Amn (Amnionless)	Mus musculus	sense antisense	GCAGCTCTGTGCAATGAC TCCAGTTGGAGGCAGTATC	63°C
Snap29	Mus musculus	sense antisense	CAGCAGGTCCTTGTCTCTCA TCTCTGTGTGTTCTAGGACTCC	57°C
Rab11a	Mus musculus	sense antisense	CGGTACAGGGCTATAACGTC CCAATAAGGCACCTACTGCT	58°C
Rab8a	Mus musculus	sense antisense	GGATTCGGAACATTGAAGAG TCCCCAGTATCATCTTCTCC	60°C
Pacsin2 (Syndapin-2)	Mus musculus	sense antisense	TGGTAGAGAAGGGACCACAG CCTCTCTGCTTCAGACATGA	60°C
Myo5a (Myosin-Va)	Mus musculus	sense antisense	AGAGGCTTACAAGCAAATGG GCATGGCATACTTAGCAGAG	60°C
Micall1	Mus musculus	sense antisense	GTGCTTCCCCACTTGCTAT GCTGAAGGAGGTTCTGAGTG	61°C
Rbsn (Rabenosyn5)	Mus musculus	sense antisense	TCTGTGGGTCTATCATGTGC GTGCTCAGAGAGTCCTTGCT	60°C
Cd59a	Mus musculus	sense antisense	CTCTATGCTGTAGCCGGAAT TGATCTCACCATGACAATCTG	60°C
Actb (β-Actin)	Mus musculus	sense antisense	CCACCGATCCACACAGAGTACTT GACAGGATGCAGAAGGAGATTACTG	57°C
Ehd1 (wt allele)	Mus musculus	sense antisense	CACTTATGGTCAGCGGATGG CCCTCTGGACAAATGAACTGG	58°C

Ehd1 (ko allele)	Mus musculus	sense antisense	GGTCGCTACCATTACCAGTTG GGCCATTTCCTGCTACTTTG	58°C
EHD3	Sus scrofa	sense antisense	GGCAATGCCTTCCTGAAC CGTGTCGATGACACTGATG	57°C
RAB8A	Sus scrofa	sense antisense	TGTCCTGTTCCGCTTCTC TGCCATCAAGCTCTATGGTC	58°C
RAB11A	Sus scrofa	sense antisense	GACGACGAGTACGACTACC CCAATGGTGCTCTTGCTTTC	58°C
MICALL1	Sus scrofa	sense antisense	CCCGACCTGCTAGATTTTG CTTCTCAGCCACCTCGAAG	58°C
TFRC	Sus scrofa	sense antisense	ATACATGGACCGGGCTAAC GGGTCACCTGTTCCTAGATG	58°C

3.1.7 Antibodies

Description	Type	Dilution	Producer
anti-Cubilin, goat polyclonal IgG	Prim.-Ab	1:200 (IF*)	Santa Cruz, Heidelberg, Germany
anti- CD107a (LAMP1), rat polyclonal [1D4B] IgG	Prim.-Ab	1:200 (IF)	BD Biosciences, Heidelberg, Germany
anti-EHD1, rabbit monoclonal [EPR4954] IgG	Prim.-Ab	1:100 (CoIP**) 1:200 (IF) 1:1000 (WB***)	Abcam, Cambridge, UK
anti-Megalin, guinea pig polyclonal IgG	Prim.-Ab	1:100 (CoIP) 1:200 (IF) 1:5000 (WB)	Dr. F. Theilig, Freiburg, Germany Pineda Antikörper, Berlin, Germany
Anti-Retinol Binding Protein, goat polyclonal	Prim.-Ab	1:200 (IF)	Thermo Fisher Scientific, Dreieich, Germany
Anti-β_2-microglobulin, rabbit monoclonal [EP2978Y]	Prim.-Ab	1:1000 (WB)	Abcam, Cambridge, UK
Anti-β-actin, rabbit polyclonal	Prim.-Ab	1:1000 (WB)	Sigma, Taufkirchen, Germany

Alexa Fluor® 488 donkey anti-rabbit	Sec.-Ab	1:400	Thermo Fisher Scientific, Dreieich, Germany
Alexa Fluor® 555 donkey anti-rat	Sec.-Ab	1:400	Thermo Fisher Scientific, Dreieich, Germany
Alexa Fluor® 647 donkey anti-rabbit	Sec.-Ab	1:400	Thermo Fisher Scientific, Dreieich, Germany
Cy5 donkey anti-guinea pig	Sec.-Ab	1:400	Thermo Fisher Scientific, Dreieich, Germany
Alexa Fluor® 488 donkey anti-goat	Sec.-Ab	1:400	Invitrogen, Karlsruhe, Germany
Alexa Fluor® 647 phalloidin	No Ab	1:400	Invitrogen, Karlsruhe, Germany

HOE33342 (Stock concentration: $5x10^{-4}$ M)	No Ab	1:500	Invitrogen, Karlsruhe, Germany
donkey anti-rabbit IgG-HRP	Sec.-Ab	1:4000	Santa Cruz, Heidelberg, Germany
donkey anti-guinea pig IgG-HRP	Sec.-Ab	1:2000	Santa Cruz, Heidelberg, Germany

*IF – Immunofluorescence
**CoIP – Co-Immunoprecipitation
***WB – Western Blot

3.1.8 Buffers and Solutions

Description	Substance	Amount
Fixation solution, pH 7,4	EGTA	1 mM
	K_2HPO_4	15 mM
	$MgCl_2$	2 mM
	NaCl	90 mM
	Paraformaldehyde	3%
	Sucrose	100 mM
	in distilled water	
Post-fixation solution	PBS	13,32 mL
	Sucrose	3,2 g
	Fixation solution	20 mL
Phosphate Buffered Saline (PBS), pH 7,4	KH_2PO_4	1,8 mM
	Na_2HPO_4	10,3 mM
	NaCl	137 mM
	in distilled water	
PBS-Tween	PBS	99,9%
	Tween 20	0,1%
2% glutaraldehyde solution, pH 7,4	Glutaraldehyde	2%
	Sodium cacodylate	0,1 M
	in distilled water	
4% glutaraldehyde solution, pH 7,4	Glutaraldehyde	4%
	Sodium cacodylate	0,1 M
	in distilled water	
1% OsO_4 solution, pH 7,4	OsO_4	1%
	Sodium cacodylate	0,1 M
	in distilled water	
Citrate Buffer, pH 6	Sodium citrate - dihydrate	2,059 g

	Citric acid - monohydrate	0,317 g
	in distilled water	to 1000 ml

0,1% SDS solution	SDS	0,1% (v/v)
	in PBS	

Blocking solution, pH 7,4	BSA	5%
	Triton X-100	0,04%
	in PBS	

Solution for antibody dilution (IF), pH 7,4	BSA	0,5%
	Triton X-100	0,04%
	in PBS buffer	

Solution for antibody dilution (Western blot)	BSA	1,5% (w/v)
	Sodium azide	0,02% (v/v)
	in PBS-Tween	

Cresyl violet solution	Cresyl violet acetate	0,1% (w/v)
	in distilled water	

Differentiation solution	Acetic acid	1% (v/v)
	in 96% ethanol	

LLC-PK1 cells medium	RPMI 1640 medium	500 ml
	FBS (heat-inactivated)	10%
	Penicillin-Streptomycin solution	1%

FITC-Dextran solution, pH 7,4	FITC-Dextran	25 mg/mL
	in 0,9% NaCl solution	

Albumin-FITC solution, pH 7,4	Albumin-FITC	10 mg/mL
	in 0,9% NaCl solution	

2% alcoholic eosin solution	Eosin Y	2% (w/v)
	Glacial acetic acid	0,5% (v/v)
	Ethanol	99,5% (v/v)

1% periodic acid solution	Periodic acid	1% (w/v)
	in distilled water	

Bouin's fixative	Picric acid	71% (v/v)
	Paraformaldehyde	24% (v/v)
	Acetic acid (glacial)	5% (v/v)

X-Gal solution A, pH 7.4	Sodium deoxycholate	1 mg/mL
	IGEPAL CA-630	2 mg/mL
	EGTA	5 mM
	$MgCl_2$	2 mM
	K_2HPO_4	100mM
	in distilled water	

X-Gal solution B	X-Gal	0,5 mg/mL
	$K_3[Fe(CN)_6]$	10 mM
	$K_4[Fe(CN)_6]$	10 mM
	in X-Gal solution A	

Co-immunoprecipitation lysis buffer	Tris-HCl	25 mM
	NaCl	150 mM
	EDTA	1 mM
	IGEPAL CA-630	0,1%
	Glycerol	5%
	in distilled water	

Stacking buffer, pH 6,8	Tris	0,5 M
	in distilled water	

Separation buffer, pH 8,8	Tris	1,5 M
	in distilled water	

Polyacrylamide stacking gel	H_2O	2,7 mL
	Stacking Buffer	500 µL
	30% Acrylamide	670 µL
	10% SDS	40 µL
	10% Ammonium persulfate	40 µL
	TEMED	4 µL

Polyacrylamide separation gel	H_2O	7,9; 5,9; 4,9; 3,4 mL
(6%; 10%; 12%; 15%)	Separation buffer	3,8 mL
	30% Acrylamide	3; 5; 6; 7,5 mL
	10% SDS	150 µL
	10% Ammonium persulfate	150 µL

	TEMED	12; 6; 6; 6 µL

Running buffer	Tris	0,025 M
	Glycine	0,192 M
	SDS	0,1% (w/v)

Transfer buffer (low-molecular-weight proteins)	Tris	3,0 g/L
	Glycine	14,4 g/L
	Methanol	20% (v/v)

Transfer buffer (high-molecular-weight proteins)	Tris	3,0 g/L
	Glycine	14,4 g/L
	Methanol	20% (v/v)
	Tween-20	0,05% (v/v)

PVDF membrane blocking solution	Nonfat-dried milk	5% (w/v)
	in PBS-Tween	

Protein fixation solution on polyacrylamide-gel	Methanol	50% (v/v)
	Acetic acid (glacial)	10% (v/v)
	Distilled water	40% (v/v)

Coomassie staining solution	Coomassie Brilliant Blue R-250	0,05% (w/v)
	Methanol	50% (v/v)
	Acetic acid (glacial)	10% (v/v)
	Distilled water	40% (v/v)

Coomassie destaining solution	Methanol	5% (v/v)
	Acetic acid (glacial)	7% (v/v)
	Distilled water	88% (v/v)

Sorenson's Buffer (133 mM), pH 7,4	133 mM Na_2HPO_4	80,4 mL
	133 mM KH_2PO_4	19,6 mL

Sorenson's Buffer (5 mM), pH 7,4	Sorenson's Buffer (133 mM)	3,76%
	in 0,9% NaCl isotonic sol.	

3.2 Methods

3.2.1 Mice

3.2.1.1 The *Ehd1*$^{-/-}$ mouse model

The *Ehd1*$^{-/-}$ mouse was generated by the Sanger Institute, as described previously [119], and acquired from the European Mouse Mutant Archive (ID: 05712). For this mouse, the *Ehd1* gene locus was targeted for homologous recombination in C57BL/6N embryonic stem cells [120]. The targeting vector was designed to allow cre-mediated deletion [121] of exon 2 (Figure 3.1). Only animals heterozygous for the conditional allele were further bred.

The conditional mouse was then bred with a global 129/Sv Cre Recombinase pCX-NLS Cre mouse and the heterozygous offspring for the *Ehd1* gene (*Ehd1*$^{+/-}$) was crossed among each other in order to obtain homozygous progeny for the *Ehd1* gene deletion (*Ehd1*$^{-/-}$). The resulting homozygous wildtype (*Ehd1*$^{+/+}$) and *Ehd1*$^{+/-}$ offspring were used as control mice. As result of the mixed genetic C57BL/6N x 129/Sv background (C57BL6;129S), offspring could either present a black or brown color.

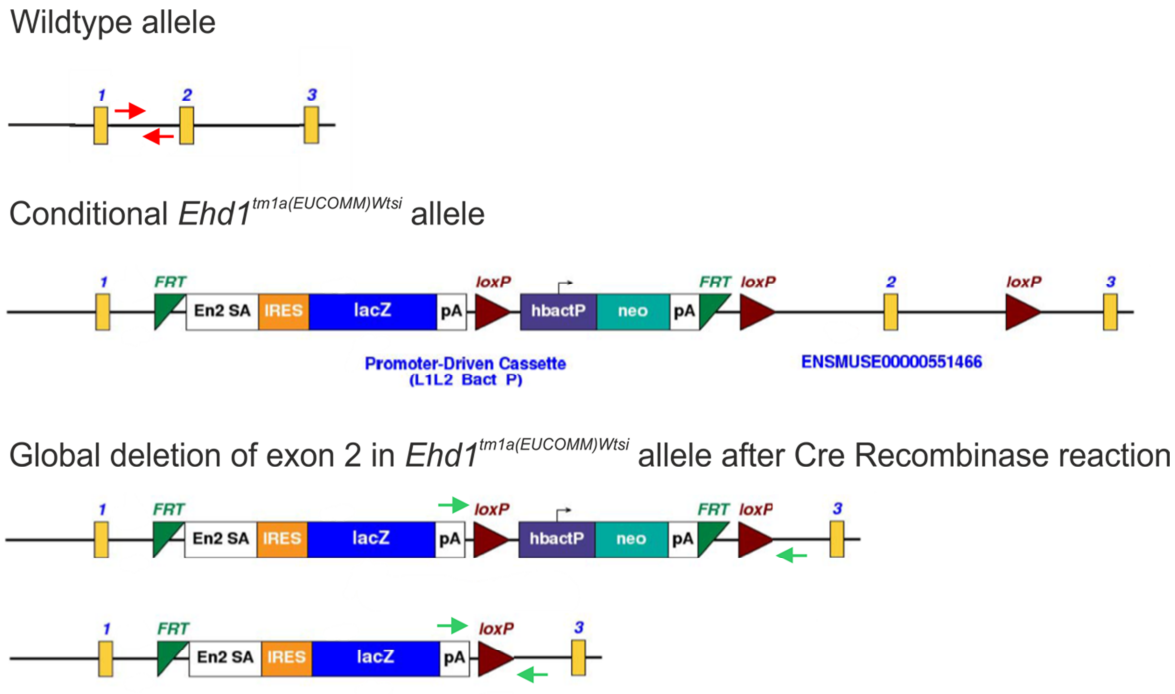

Figure 3.1: Different alleles for *Ehd1* locus.
The insertion of the targeting vector, by homologous recombination, into *Ehd1* locus originated a conditional allele. This allele harbors three loxP sites capable of being recognized by a Cre recombinase, leading eventually to exon 2 deletion. Two different alleles carrying the exon 2 deletion can be obtained, depending on the recognized loxP sites. The hybridization position for the primers used for the wildtype (red arrows) and knockout (green arrows) alleles is depicted.

Animals were maintained on a standard diet with free access to food and water. The experimental protocols were approved by the local councils for animal care and were conducted according to the German and French law for animal care.

3.2.1.2 Isolation of genomic DNA

The genomic DNA (gDNA) was isolated from tail biopsies (2 mm) of mice. The tails were digested overnight at 55°C in 300 µL Tail Buffer (0.1 M EDTA, 0.5% SDS, 50 mM Tris-HCl, pH 8) with 1 µL proteinase K (100 mg/mL) and shaking. On the next day, 100 µL of ammonium acetate (7.5 M) were added to the digested tails, followed by 600 µL of isopropanol, always with proper homogenization of the solution. The mixture was then incubated at -20°C for 20 minutes, for DNA precipitation. Thereafter, the probe was centrifuged for 10 minutes at 13000 rpm to obtain the DNA pellet. The pellet was washed with 1 mL of 70% Ethanol, centrifuged once again and the supernatant was discarded. Finally, after air-dried for 15 minutes, the gDNA was resuspended in 80 µL of TE buffer (10 mM Tris, 1 mM EDTA, pH 7.5). The gDNA was stored at 4°C.

3.2.1.3 Genotyping of *Ehd1*$^{-/-}$ mice

The genotyping of the mice was performed through real time polymerase chain reaction (PCR), using the SYBR® Green PCR Kit and a Light-Cycler System 2.0 from Roche. The PCR master mix was prepared with 1 µL mouse gDNA, 5 µL SYBR® Green mix, 3 µL PCR-H_2O, 0.5 µL of each sense and antisense primers (10 µM), for either the wildtype or knockout alleles (see 3.1.6 Oligonucleotides and Figure 3.1). The conditions used for the run in the light cycler were: 95°C for 10 min, 95°C for 15 sec, 58°C for 20 sec, 72°C for 30 sec, 40 cycles. The amplicon sizes for the wildtype and knockout alleles were 456 base pairs (bp) and 401 bp, respectively. The PCR conditions only allowed the identification of the knockout allele resulting from the recognition of the first and third loxP sites by the Cre Recombinase (see Figure 3.1, second possibility for global deletion of exon 2 in *Ehd1*$^{tm1a(EUCOMM)Wtsi}$ allele).

3.2.2 Cell lines

3.2.2.1 Inducible LLC-PK1 WT-, R398W-hEHD1 cell lines

As a cell model the LLC-PK1 cell line was used. They are renal proximal tubular cells derived from pig [122] and were used due to the presumed function of EHD1 in the kidney and more specifically in proximal tubular cells. The LLC-PK1 cells were stably transfected by Dr. Enriko Klootwijk (Royal Free Hospital – Centre for Nephrology, London), using the Tet-On-System to control the expression of the transfected gene. The expression can be activated by adding tetracycline (1 µg/mL) to the cell medium for at least 48 h. Tetracycline binds to the repressor, preventing the inhibition of the gene promotor and allowing then gene transcription. These cells were either transfected with the human form of wildtype or mutant R398W EHD1 (WT-, R398W-hEHD1).
The cells were maintained in flasks at 37°C and 5% CO_2 in LLC-PK1 medium. For specific experiments cells were grown in cell culture filters in order to achieve polarization.

3.2.3 Histological Methods

3.2.3.1 Retrograde arterial perfusion and tissue fixation

The fixation of the tissue was performed to preserve the material and improve the cutting conditions. The fixation with paraformaldehyde causes cross-linking between the proteins, stabilizing the structure.
The mice were anesthetized through inhalation of isoflurane (2.5% isoflurane in a gas mixture of 50% oxygen and 50% nitrogen with a flow of 60 mL/min). After opening the abdominal cavity and clearing the abdominal aorta, the vessel was clamped below the renal artery. The polyethylene catheter was inserted distal to the clamp and fixed with another clamp. After incision of the inferior vena cava and removal of the proximal aortal clamp, blood was removed by perfusion with 10 mL 0.9% NaCl supplemented with 10 IU/mL of Heparin. Next, the dead mice were perfused with fixation solution at a constant flow rate of 10 mL/min assured with a roller pump. The fixed organs were then harvested and handled accordingly to the following procedure (cryo or paraffin preparation).

3.2.3.2 Bouin's fixation of paraformaldehyde-perfused testicles and epididymis

Bouin's fixative consists of picric acid, formaldehyde and acetic acid. It is normally used for testicular fixation because it preserves nuclei and chromosomes and allows identification of mitotic and meiotic figures. Bouin's fixative also works as a mordant for paraformaldehyde-fixed tissues, improving the results of the staining.

The harvested paraformaldehyde-perfused testicles and epididymides were fixed overnight at 4°C in Bouin's fixative. The tissue was then washed in PBS to remove the excess of picric acid, stored in 70% ethanol and later embedded in paraffin (see 3.2.3.3 Paraffin embedment of perfused tissue and sections preparation).

3.2.3.3 Paraffin embedment of paraformaldehyde-perfused tissue and sections preparation

For paraffin embedment, the harvested paraformaldehyde-perfused organs were stored in 70% methanol. The tissue was then placed in embedding cassettes and, before the paraffin embedment, washed with increasing concentrations of methanol (70%, 80%, 90%, 100%; 25 min each wash) for gradual dehydration, followed by a final wash with 100% isopropanol for 25 min. After this, the tissue was incubated for 1 h in isopropanol/paraffin (1:1) and next placed overnight in paraffin, always at 70°C. On the next day, the paraffin solution was changed, in order to remove any traces of isopropanol, and the tissue was left to incubate for 1 h more in the new paraffin solution at 70°C. Finally, the tissue was embedded in liquid paraffin (70°C) in a metal cast, covered with the tissue cassette and the paraffin was let to cool and harden overnight at 4°C.

On the next day, the tissue embedded in paraffin was removed from the cast and then sectioned using a rotary microtome. The sections obtained had a thickness of 5 µm. The sections were then placed in a water bath at 40°C, to allow stretching. After mounting the sections on polysine microscope slides, they were left to dry for 30 min at 40°C. The sections were stored at 4°C.

For paraffin embedment of cochlear tissues decalcification is needed before storage in 70% methanol. To this end, cochleae were incubated overnight at 4°C in a PBS based solution containing 1.5% paraformaldehyde and 17% sucrose (post-fixation solution), rinsed in PBS and decalcified for 5 days in Osteosoft® at 4°C. After washing with PBS, the cochleae were stored in 70% methanol and the described protocol for paraffin embedment was followed.

3.2.3.4 Cryo preparation of paraformaldehyde-perfused tissue and sectioning

The harvested perfused tissues were incubated for 1 h at 4°C in post-fixation solution. The high sucrose content reduces the formation of crystals, when freezing the tissue. Next, the tissues were frozen in 2-methylbutane, cooled to -35°C, and then stored at -80°C.

Before cutting, the frozen specimen was embedded in OCT-medium and fixed in the object holder. The sections were cut using a cryostat with a chamber temperature of -25°C. The thickness of the sections was 5 µm. Finally, the sections were mounted on polysine microscope slides and stored at -20°C.

3.2.3.5 Preparation of paraformaldehyde-perfused tissue for electron microscopy

After harvesting the perfused tissues, they were post fixated with 4% glutaraldehyde solution for 60 min and then rinsed two times with 0.1 M sodium cacodylate pH 7.4, 15 min each.

Inducible LLC-PK1 cells were grown on cover slips and induced with tetracycline (1 µg/ml) for 48 h. Before embedment, cells were fixed using a 2% glutaraldehyde solution for about 1 h. Post fixation and dehydration were carried out by rinsing the samples in 0,1 M sodium cacodylate pH 7.4 (3 x 20 min), 1% OsO4 solution (2 h), 0.1 M sodium cacodylate pH 7.4 (3 x 20 min), 50% ethanol (15 min), 70% ethanol (15 min), 90% ethanol (15 min), 96% ethanol (15 min), 100% ethanol (20 min), acetone (3 x 15 min). Finally, samples were embedded in epoxy embedding medium and polymerized at 60°C for 48 h using standard protocols.

3.2.3.6 Hematoxylin and Eosin staining

The Hematoxylin-Eosin (HE) staining takes advantage of the electrostatic attraction between ions of opposite charge, one of which is fixed in the tissue, and the other one is in the dye. Hematoxylin has a deep blue-purple color and can react with negatively charged, basophilic cell components, such as nucleic acids in the nucleus. Eosin is pink and stains positively charged acidophilic components in the tissue, such as amine groups of proteins in the cytoplasm.

For the HE staining, paraffin embedded tissue sections were used. Before being stained, paraffin sections were incubated two times with xylol, 15 min each, and then washed with 100% isopropanol and decreasing concentrations of ethanol (99%, 95%, 80%, 70%; 15 min each wash), leading to deparaffinization and rehydration of the tissue. After washing during 5 min with PBS, the sections were incubated for 3 min with Mayer's hemalum solution. Hemalum is a complex formed from aluminium ions and haematin (oxidation product of hematoxylin) that binds to nucleic acids. The sections were then washed with flowing tap water for 3 min, in order to remove excess of hemalum solution and produce the blue/purple chromatin stain. Next, the tissues were counterstained with 2% alcoholic eosin solution for 2 min and eosin excess was washed away with distilled water for 1 min. The dehydration of the sections was performed by a very brief wash with increasing concentrations of ethanol (70%, 80%, 95%,99%) and a 5 min wash in xylol (two times). Finally, the sections were mounted in DePeX (xylol based mounting media).

3.2.3.7 Periodic Acid–Schiff staining

Periodic acid–Schiff (PAS) is a staining used to detect polysaccharides such as glycogen, and muco-substances such as glycoproteins, glycolipids and mucins in tissues.

For the PAS staining, paraffin embedded tissue sections were used and, like described before (see 3.2.2.4 Hematoxylin and Eosin staining), deparaffinized and rehydrated before the staining. The sections were then incubated with 1% periodic acid solution for 10 min, leading to the oxidation of glycols into aldehydes. Afterwards, the tissue was rinsed three times with distilled water, 1 min each, and further incubated with the Schiff's reagent for 15 min. The Schiff's reagent is a mixture of pararosaniline and sodium metabisulfite that reacts with aldehydes giving a purple/magenta color to the tissue. In order to wash away the excess of Schiff's reagent, the sections were rinsed with tap water at 37°C for 5 min. Next, a counterstain with Mayer's hemalum solution was performed with incubation of the sections for 1 min, enabling the staining of nucleic acids. The tissues were once again washed with tap water for 5 min and the sections were dehydrated (see 3.2.2.4 Hematoxylin and Eosin staining) and mounted in DePeX.

3.2.3.8 Detection of β-galactosidase activity: X-Gal staining

X-Gal (5-bromo-4-chloro-3-indolyl-beta-D-galactopyranoside) staining is a histochemical technique used to detect the expression of the bacterial *LacZ* gene. The technique takes advantage of the product of the *LacZ* gene, the β-galactosidase enzyme. β-galactosidase catalyzes the hydrolysis of β-galactosides into monosaccharides. X-Gal is an organic compound consisting of galactose linked to a substituted indole, which functions as a substrate to β-galactosidase. The enzyme has high specificity for the galactose part of the substrate but low specificity for the remainder. Thus, it hydrolyses X-Gal, releasing the substituted indole that spontaneously dimerizes to give an insoluble, intensely blue product.

X-Gal staining provides a visual assay of *LacZ* activity. Therefore, we can use this blue stain as a marker of our gene of interest by placing the *LacZ* gene under the control of the regulatory elements of the gene of interest. For the mouse line used in this project, the *LacZ* gene was knocked into the *Ehd1* gene in the targeting vector used to create the conditional $Ehd1^{tm1a(EUCOMM)Wtsi}$ allele (Figure 3.1).

After paraformaldehyde perfusion of the mice, cryo preparation and sectioning, the tissues were rinsed for 5 min with PBS. The sections were then incubated overnight in X-Gal solution B at 37°C, in the dark. On the next day, the sections were again washed with PBS for 5 min and the slides were mounted with non-fluorescent glycergel mounting medium.

3.2.3.9 Immunohistochemistry

Immunohistochemistry (IHC) is a technique used to identify the interaction of target antigens with specific antibodies tagged with a visible label, which can be either a

fluorescent dye, an enzyme, a gold particle or an isotope. IHC makes it possible to visualize the distribution and localization of specific cellular components within cells and in the proper tissue context. In case of an indirect immunofluorescence two antibodies are used. The first (primary antibody) recognizes the target antigen in the tissue or cell and the second (secondary antibody), which is labelled with a fluorescent tag, is directed against the F_c region of the primary antibody. The antigen-antibody complex can be detected by excitation of the fluorophore with light of the corresponding wavelength.

When immunofluorescence was performed in paraffin-embedded tissue sections, sections were first deparaffinized and rehydrated (see 3.2.2.6 Hematoxylin and Eosin staining) and then incubated in citrate buffer pH 6 for 15 min at 94°C in the water bath for epitope unmasking, followed by a 5 min PBS wash to remove the citrate buffer.

When cryo sections were used for immunofluorescence, they were first washed with PBS for 5 min (two times) to remove the OCT-medium used for the sectioning in the cryostat. For epitope unmasking the sections were incubated in 0.1% SDS solution, followed by two times wash with PBS for 5 min each.

After epitope unmasking, the protocol used for immunofluorescence was the same for both paraffin and cryo sections. The tissue was incubated in a blocking solution (5% BSA solution) for 10 min, to reduce antibody unspecific binding. The primary antibody was then diluted in a PBS based solution containing 0,5% BSA, for further blocking, and 0,04% Triton X-100, a detergent used to permeabilize the cell membranes and help the antibody diffusing into the tissue. The incubation of the sections with the primary antibody was performed overnight at 4°C in a humid chamber. On the next day, the tissue was washed two times with PBS for 5 min each to remove the non-bound antibody and then incubated with the secondary antibody (the same solution for antibody dilution was used) for 1 h at room temperature and in the dark. Finally, the sections were once again washed two times with PBS, each time for 5 min, to remove non-bound secondary antibody and mounted in non-fluorescent glycergel mounting medium.

LLC-PK1 cells for immunofluorescence were cultivated on glass cover-slips. After washed in PBS, the cells were fixed with 3% paraformaldehyde for 10 min and once again thoroughly rinsed with PBS (3 times for 5 min). The following procedure was similar to the one performed for cryo sections.

3.2.3.10 Microscopy

For analysis of several immunofluorescent stainings a confocal microscope (LSM 710, Zeiss) was used. The objective used was a Plan-Apochromat 63x/1.4 water immersion. The pinhole was adjusted to 1 μm optical section thickness. To detect the fluorophore bound to the secondary antibody a monochromatic laser light with wavelength of 405 nm

(for HOE33342), 488 nm (for Alexa Fluor® 488), 561 nm (for Alexa Fluor® 555) and 633 nm (for Alexa Fluor® 647 and Cy5) was used for the excitation of the fluorophore. The emitted fluorescent light was detected accordingly with band-pass filters of 450−517 nm, 493−542 nm, 562−640 nm and with a long-pass filter of 638−755 nm.
An inverted microscope (Axiovert 200, Zeiss) with a 20x objective was used to create an overview of the slices and the 63x objective was used to acquire more detailed images. For the excitation of the secondary antibodies, the corresponding wavelengths for the fluorophores of the secondary antibody were used as already mentioned.
Ultrathin sections were imaged using either an EM902 (Zeiss, Oberkochen, Germany) or a JEM-2100F (JEOL, Tokyo, Japan) transmission electron microscope, operated at 80 keV (902) or 200 keV (JEM). Digital micrographs were recorded using a CCD 2k camera or a CMOS 4k F416 camera.

3.2.4 Molecular Biology Methods

3.2.4.1 Isolation of total RNA from mouse tissue and LLC-PK1 cells

RNA was isolated from several mouse tissues and from both males and females. The mice were anesthetized with isoflurane and then euthanized by cervical dislocation. The tissues were harvested, frozen in liquid nitrogen and stored at -80°C until used. Before RNA isolation, the tissues were minced with a mortar and a pestle in liquid nitrogen and approximately 30 mg were used for the isolation. RNA isolation was performed using a NucleoSpin RNA kit from Macherey-Nagel according to manufacturer's instructions.
The RNA isolation from the cochlea was done as previously described in K. Vikhe et *al*, 2015 [123]. Per mouse, the pair of cochleae was used for RNA extraction. The cochleae were first disintegrated in 750 µL Trizol using an Eppendorf pestle in order to lyse the cells, and then centrifuged at 12000g for 5 min at 4°C to remove bone debris. To the lysate 150 µL of chloroform were added and the sample was mixed for 15 s using the vortex. After centrifugation at 12000 g for 15 min at 4°C, two distinct phases were obtained, an aqueous phase (on top), where the nucleic acids were, and an organic phase (below), enriched with hydrophobic proteins and lipids. The aqueous phase was collected and 350 µL of 70% ethanol were added. The mixture was then purified using the NucleoSpin RNA kit from Macherey-Nagel according to manufacturer's instructions.
For the RNA isolation from LLC-PK1 cells, two 100% confluent p35 mm Petri dishes were used. The cells were washed two times with PBS and then collected using a cell scraper. Cell lysis and RNA extraction were done using the NucleoSpin RNA kit from Macherey-Nagel according to manufacturer's instructions.

Sample concentration and purity were assessed using a Nanodrop spectrophotometer. Samples with a A260/A280 ratio of 1.6–2.0 were accepted.
All RNA samples were stored at -80°C.

3.2.4.2 Synthesis of cDNA by RNA reverse transcription

A RNA molecule can be converted into complementary DNA (cDNA) by a process named reverse transcription. To achieve this, a RNA-dependent DNA-polymerase (also known as reverse transcriptase) was used to synthesize cDNA from the RNA probes obtained before. Since RNA is unstable, the obtained cDNA was later used as template for the PCR. For the reaction, 1 µg of total RNA was diluted in Nuclease-free water making a total volume of 13 µL. After adding 1 µL of Random Hexamer Primers (100 µM), the mixture was incubated for 5 min at 70°C and placed on ice immediately after. To the reaction mix were added: 5 µL M-MLV Reverse Transcriptase Buffer (5X), 1.25 µL dNTP-Mix (10 mM each dNTP), 1 µL RNAse inhibitor and 3.75 µL RNAse-free water. To 20 µL of the reaction mix, 1 µL M-MLV Reverse Transcriptase (100 U) was added, while the other 5 µL of the mix were the negative control with no reverse transcriptase. The two mixes were then incubated for 10 min at room temperature and afterwards for 50 min at 50°C for cDNA synthesis. In order to inactivate the enzyme, the reaction mixes were finally incubated for 15 min at 70°C. The obtained cDNA was stored at 4°C until its usage in the PCR reaction.

3.2.4.3 Quantitative Polymerase Chain Reaction (Real time PCR)

In the quantitative PCR reaction the DNA amount is determined after each PCR cycle by photometry. Because of this, it is possible to follow the exponential PCR reaction in real time. The quantification of the amplified DNA products is performed indirectly through the measurement of the SYBR® Green fluorescent dye. The dye binds the double-strands of DNA with high affinity and once bound its fluorescence intensity is 1000-fold stronger as the free dye and proportional to the amount of DNA.
The real time PCR was performed using the SYBR® Green PCR kit and a Light-Cycler System 2.0 from Roche. The 10 µL reaction mix consists of 5 µL SYBR Green mix, 3 µL RNase free H_2O, 0.5 µL of each sense and antisense primers (10 µM) and 1 µL of cDNA. The sequence and annealing temperature for all primers used is given in section “3.1.6 Oligonucleotides”. The primers were always designed to bind to two consecutive exons, thereby avoiding amplification of contaminant genomic DNA. The protocol used for amplification was: 95°C for 10 min (for DNA-polymerase activation) followed by 40 cycles with 95°C for 15 s (for DNA denaturation), 20 s at the annealing temperature of the primers (for hybridization of the primers with the DNA) and 72°C for 30 s (for elongation

phase). After the run of the amplification protocol, the melting curve of each product was obtained. For this, the DNA temperature was increased from 60°C to 95°C in a controlled fashion (0.1°C/s) and the fluorescence was further measured. The specificity of the primers was always confirmed by analysis of the melting curve and PCR products in a 2.5% agarose-gel. The data were normalized to the expression of the β-actin gene, a known housekeeping gene.

3.2.4.4 Isolation of protein from mouse kidney and LLC-PK1 cells

Protein was isolated from the mouse kidney and from both males and females. The mice were first anesthetized with isoflurane and then euthanized by cervical dislocation. The kidneys were then harvested and homogenized on ice in co-immunoprecipitation lysis buffer (3 µL lysis buffer to 1 mg tissue) supplemented with protease inhibitors (1:100). To help cell lysis, the probes were passed through a syringe with a 22G and 27G needle, respectively 10 times each. Next, the samples were submitted to four cycles of 20 sec sonication, 40 sec incubation on ice. Finally, the probes were centrifuged at 14000 rpm for 10 min at 4°C and the supernatant containing the proteins was collected.
For the protein isolation from LLC-PK1 cells, two 100% confluent p35 mm Petri dishes were used. The cells were washed two times with PBS and then collected in 150 µL co-immunoprecipitation lysis buffer supplemented with protease inhibitor using a cell scraper. The following protocol was similar to the one performed for protein isolation from tissue.
All protein samples were stored at -80°C.

3.2.4.5 Quantification of protein samples

For quantification of the protein samples the Bradford protein assay from Bio-Rad was used. This assay is based on the binding of protein molecules to the Coomassie dye under acidic conditions, resulting in a color change from brown to blue. This method measures the presence of the basic amino acid residues — arginine, lysine and histidine — which contribute to the formation of the protein-dye complex. The dye reagent was diluted 1:5 in distilled water and then filtered to remove particles. The probes (2 µL) were diluted in 1 mL dye, as well as the protein standard, BSA, at increasing concentrations of 2, 4, 6, 8, 10, 15 and 30 µg/mL. After 15 min incubation at room temperature in the dark, the absorbance of triplicates for each sample was measured at 595 nm. The protein concentration of the probes was extrapolated from the calibration curve obtained from the measurements with the standard protein.

3.2.4.6 Western blot

The Western blot is a technique used to detect the presence of a specific protein in a complex mixture extracted from cultured cells or animal tissue. This technique consists of three steps: the run — separation of protein mixtures by size using sodium dodecyl sulfate-polyacrylamide gel electrophoresis (SDS-PAGE); the transfer — efficient transfer of separated proteins to a solid support, normally a polyvinylidene difluoride (PVDF) or a nitrocellulose membrane; and the detection — specific detection of a target protein by appropriate antibodies. After detection, the target protein is visualized as a band on a blotting membrane, X-ray film, or an imaging system.

The protein samples were first diluted 1:1 in 2x Laemmli Sample Buffer (previously supplemented with DTT, according to manufacturer's instructions). After polymerization of the polyacrylamide-gel (4% acrylamide stacking gel — for sample concentration — and 6 to 15% acrylamide separation gel — higher concentrations of acrylamide were used when separation of low-molecular-weight proteins was needed), 30–80 µg of protein sample were loaded and separated by size through electrophoresis. The Precision Plus Protein™ Dual Color Standards (6 µL) were used as a marker to control protein size. The run was performed at 80 V for 30 min, to allow concentration of the sample, and at 100 V for 90 min, for protein separation. The proteins in the polyacrylamide-gel were then transferred to a PVDF membrane, previously activated for 20 sec with methanol and washed with distilled water, through the wet transfer method. In this method, the gel is first equilibrated in transfer buffer and then placed in the "transfer sandwich" (sponge-filter paper-gel-membrane-filter paper-sponge) and pressed together by a support grid. The supported gel sandwich is placed vertically in a tank between stainless steel/platinum wire electrodes and filled with transfer buffer (different for low or high-molecular-weight proteins; see 3.1.8 Buffers and Solutions). Proteins migrate towards the anode due to their overall negative charge. Depending on the size of the protein of interest, the transfer was performed for 75 min at 100 V on ice (low-molecular-weight proteins) or overnight at 30 V and 4°C (proteins larger than 150 kDa). After the protein transfer, the PVDF membrane was blocked in 5% nonfat-dried milk (in PBS-Tween) for 30 min at room temperature to reduce unspecific binding of the antibody to the membrane. Finally, the membrane was incubated overnight at 4°C with agitation with the primary antibody against the protein of interest, washed with PBS-Tween (3 x for 5 min), in order to remove non-bound antibody and incubated with the secondary antibody conjugated with horseradish peroxidase for 1 h at room temperature. After washing the membrane once again with PBS-Tween (3 x for 5 min), the protein bands were detected using chemiluminescent substrates for horseradish peroxidase and observed using an imaging system.

3.2.4.7 Co-immunoprecipitation (Co-IP) in mouse tissue

Co-immunoprecipitation is a widely used method for detection of protein-protein interaction.

Many associations between proteins that exist within the cell remain intact when a cell is lysed under non-denaturating conditions. Therefore, when a certain protein is immunoprecipitated, the proteins that are stably associated with it should also co-precipitate. In a Co-IP an antibody against a specific target protein forms an immune complex with that target in a sample, such as proteins isolated from cultured cells or animal tissue (see 3.2.3.4 Isolation of protein from mouse kidney and LLC-PK1 cells). The immune complex is then precipitated on protein-bound beads (such as Protein A or G) that bind the F_c region of IgG class of antibodies, and all proteins not precipitated on the beads are washed away. Finally, the immune complex is eluted from the beads by incubation with denaturating buffers and analyzed by SDS-PAGE, followed by Western blot detection of the protein that is associated with precipitated protein.

The beads were first prepared in Protein A Sepharose/Protein G Agarose (1:1) mix and washed 3 times with Co-IP lysis buffer. After centrifuging the beads for 1 min at 5000 rpm and 4°C, they were diluted in lysis buffer to obtain a 50% slurry. The protein extract isolated from the mouse kidney (2 mg), as described in section “3.2.3.4 Isolation of protein from mouse kidney and LLC-PK1 cells”, was then precleared with 50 µL of the prepared A/G protein mixed beads and lysis buffer supplemented with protease inhibitor (1:100) was added to a final volume of 500 µL. The mixture was rotated overhead at 4°C for 1 h. Afterwards, the beads were spun down and discarded. The precleared protein extract was incubated overnight with the antibody specific for the target protein (1:100) under overhead rotation at 4°C. As a control for unspecific binding of the beads, a precleared protein extract without antibody incubation undergoing the same protocol was used. On the next day, 100 µL of A/G protein 50% slurry was added to the protein extract and the mixture was incubated for 3 h at 4°C with overhead rotation, in order to precipitate the antibody-protein complex. After 3 h, the beads were washed 5 times in 1 mL Co-IP lysis buffer with a 5 min overhead rotation in between washing steps. Finally the protein was eluted in 50 µL 4x Laemmli Sample Buffer. The stock of protein extract, the eluted protein and the respective control were loaded in a polyacrylamide-gel and a Western blot (see 3.2.3.6 Western Blot) to detect the protein thought to be associated with the precipitated protein was performed.

3.2.4.8 Coomassie blue staining of SDS-PAGE from mouse spot urine

The Coomassie dye is often used to detect proteins in a polyacrylamide-gel. It is able to bind to proteins through ionic interactions between dye sulfonic acid groups and positive

protein amine groups as well as through Van der Waals attractions. The lower limit of detection for the Coomassie dye is around 36–47 ng of protein.

The Coomassie staining was performed to assess for proteinuria (presence of proteins in the urine) in the mice. For this, spot urine was collected from male mice (wildtype, heterozygous and knockout) of the same age. The urine (5 µL) was then diluted 1:1 in 2x Laemmli Sample Buffer and heated at 37°C for 15 min. Afterwards, the samples were loaded into a 12% polyacrylamide separating gel and the run was performed at 50 mA for 5 min, 25 mA for 15 min and 50 mA for 60 min. To avoid diffusion, the proteins were then fixed on the gel by a 45 min incubation in a solution based on methanol (Protein fixation solution on polyacrylamide-gel) with agitation. Next, the gel was stained with Coomassie (Coomassie staining solution) overnight with agitation. On the next day, the gel was once again incubated in Protein fixation solution for 30 min with agitation and finally, to reduce background color, a 3 h incubation in Coomassie destaining solution with agitation was performed. After washing the gel with water, images were made.

3.2.5 Auditory brainstem response measurement in the mouse

The auditory brainstem response (ABR) is often used to assess the hearing ability of animals [124,125]. The ABR reflects the neuronal activity in the auditory pathway and consists of a series of short waves, where the individual waves refer to the different processing steps in the auditory pathway. Wave I is associated with activity in the cochlear nerve, wave II with the dorsal cochlear nucleus, wave III with the superior olivary complex, wave IV with the preolivary and lateral lemniscal nucleus and wave V with the inferior colliculus [126].

The ABR measurements where performed in collaboration with Prof. Dr. Holger Schulze's group (Department of Otorhinolaryngology-Head and Neck Surgery, University Hospital Erlangen) and supervised by Dr. Konstantin Tziridis and Achim Schilling.

3.2.5.1 Mouse preparation

For this experiment, five male and female mice with age between 8–9 weeks were used as control mice (wildtype and heterozygous) and compared with five *Ehd1*$^{-/-}$ animals.

The animals were anaesthetized using a mixture of ketamine (96 mg/kg), xylazine (4 mg/kg) and physiological NaCl solution at a mixing ratio of 9:1:8, initial dose: 0,3 mL s.c.; continuous application at a rate of 0,2–0,3 mL/h. Afterwards, the mice under deep anesthesia were placed within a sound-attenuated chamber on a thermally controlled heating pad at 37°C, and frequency-specific auditory brainstem responses (f-ABR) were measured.

3.2.5.2 f-ABR measurement (frequency-specific auditory brainstem responses)

The protocol was performed as previously described in Tziridis *et al*., 2017 [124]. The f-ABR was measured via subcutaneously placed thin silver wire electrodes (0.25 mm diameter) using a CED micro 1401 data acquisition unit with a CED 3505 programmable attenuator via a custom-made program (Spike2, CED). Auditory stimuli were presented free-field to one ear at 3 cm distance from the animal's pinna via a speaker. The speaker's frequency response function was corrected to be flat within $\pm$1 dB. Stimuli presented were pure tones (6 ms duration including 2 ms cosine-squared rise and fall times) at 11, 22 and 32 kHz. 150 stimuli were presented with alternating inverted phase with a repetition rate of 4 Hz. The stimuli of one frequency were presented pseudorandomized starting at a sound pressure level of 10 dB and ending at 95 dB SPL with a step width of 5 dB.

3.2.5.3 Data evaluation

To obtain f-ABR-based hearing thresholds, the mean f-ABR waves were compared to the mean amplitude 200–100 ms before the stimulus (baseline). Thresholds were defined automatically by a custom-made MATLAB program at the highest attenuation at which the evoked amplitude raised over 5% of the dynamic range above the noise level assessed by fitting of a sigmoid function. Data were discarded at frequencies where this procedure was not possible, for example, at low signal-to-noise ratios.

3.2.6 Evaluation of mouse spermatozoon motility

In order to test for sperm motility, 10 male control mice (wildtype and heterozygous) and 7 knockout males were first anesthetized with isoflurane, euthanized by cervical dislocation and the epididymides were harvested. Sperm motility was observed as previously described in Philipps *et al*., 1972 [127]. The harvested epididymides were rinsed in 0.9% NaCl solution with 5 M Sorenson's Buffer and the spermatozoa were inspected using a brightfield inverted microscope (Axiovert 200, Zeiss) with a 40x objective. Videos were made using the same microscope, objective and settings by acquiring images with a sampling interval of 60 ms for 1 min.

3.2.7 Challenge of the mice with the low-molecular-weight protein β_2-microglobulin

3.2.7.1 Conjugation of β_2-microglobulin with the fluorescent tag Alexa Fluor 546

A recombinant, human β_2-microglobulin expressed in *E. coli.* was purchased from Merck and 1 mg of protein was used for conjugation with the fluorescent tag Alexa Fluor™ 546. The conjugation was achieved by using the Alexa Fluor™ 546 Protein Labelling Kit from

Thermo Fisher, according to manufacturer's instructions. The Alexa Fluor™ 546 reactive dye has a succinimidyl ester moiety that reacts efficiently with primary amines of proteins to form stable dye–protein conjugates. The conjugates were separated from the unconjugated dye by an exclusion purification resin. The obtained β_2-microglobulin-Alexa Fluor 546 exhibited a concentration of ~ 77 µM.

3.2.7.2 IV injection of β_2-microglobulin-Alexa Fluor 546 into mice

For this experiment, male mice of identical age were used (ten wildtype and heterozygous mice as control mice and seven knockout mice).

The mice were first anesthetized through inhalation of isoflurane (2.5% isoflurane in a gas mixture of 50% oxygen and 50% nitrogen with a flow of 60 mL/min). After performing a skin incision at the thigh and clearing the femoral vein, a polyethylene catheter was inserted into the vein. Before injection, the β_2-microglobulin-Alexa Fluor 546 was diluted (1:50) in 0.9% NaCl isotonic solution and the urinary bladder was emptied, using an insulin-syringe. The β_2-microglobulin solution was then injected through the femoral vein at a concentration of 20 µL/g of body weight. After 30 min, urine and blood were collected and retrograde arterial perfusion and tissue fixation was performed as described in section "3.2.2.1 Retrograde arterial perfusion and tissue fixation". The kidneys were harvested and while one was homogenized the other was prepared for cryo sections (see 3.2.2.4 Cryo preparation of paraformaldehyde-perfused tissue and sectioning). The Alexa Fluor 546 fluorescence intensity was then measured using a microplate reader as described below.

3.2.7.3 Isolation of blood serum and kidney homogenization

To isolate the serum after blood collection, the coagulated blood samples were centrifuged at 5000 rpm for 10 min at room temperature. After centrifugation two phases were obtained, a lower phase corresponding to clotted blood and an upper phase corresponding to serum, which was then collected and fluorescence levels were measured.

After harvesting the kidneys, half a kidney was weighted and homogenized in distilled water (1 mg tissue:10 µL distilled water) using an Eppendorf micropestle. The sample was then sonicated for 10 min, followed by a 5 min centrifugation at 14000 rpm and room temperature. The supernatant was collected and fluorescence was measured.

3.2.7.4 Measurement of β_2-microglobulin-Alexa Fluor 546 fluorescence

The fluorescence of β_2-microglobulin-Alexa Fluor 546 in urine, serum and kidney lysate samples was measured by NOVOstar Microplate reader. As a control for the

measurement in the urine sample, the urine of the same mouse collected before β_2-microglobulin-Alexa Fluor 546 injection was used. For the serum and the kidney lysate controls, the same samples were collected from a mouse undergoing the same protocol but injected with 0,9% NaCl isotonic solution instead.

3.2.8 Measurement of colocalization using immunofluorescence

For the measurement of protein colocalization the ZEN Pro V2.3 software was used. The program quantifies the intensity of the fluorescent signal of the fluorophore associated to an antibody specific to the target protein, in a region chosen by the user. Different fluorescent signals can then be compared at the same time and on the same place of the staining. The overlap of the different signals is translated in protein colocalization.

3.2.9 Live-imaging of renal proximal tubular endocytosis in the mouse kidney

This experiment was performed in collaboration with Prof. Dr. Hayo Castrop's group (Institute for Physiology, University of Regensburg) and supervised by Dr. Ina Schießl.

3.2.9.1 Mouse preparation

For this experiment, 6 male and female mice with identical age were used as control mice (wildtype and heterozygous) and compared with 6 knockout animals.

The mice were anesthetized through inhalation of isoflurane (2.5% isoflurane in a gas mixture of 50% oxygen and 50% nitrogen with a flow of 60 mL/min). The body temperature was maintained at 37.5°C by placing the animals on an operating table with a servo-controlled heating plate. A cannula connected to a syringe was inserted into the right jugular for the intravenous infusion of either FITC–Dextran 500 kDa or β_2-microglobulin-Alexa Fluor 546. For the imaging session, the left kidney was exposed by making a small flank incision.

3.2.9.2 Multiphoton microscopy

The experiments were performed using a Zeiss LSM 710 confocal fluorescence microscope equipped with a servo-controlled warming plate to maintain the body temperature of the animal at 37°C. Excitation was achieved using a Chameleon Ultra-II MP laser (Coherent Deutschland, Dieburg, Germany) at 940 nm with a laser power of 20% of 3200 mW. Eight-bit 1454 x 1454 pixel images (providing a theoretical dynamic range for intensities measurements of 0–65536 pixel intensity) were obtained using a pixel dwell time of 3.15 µs and a line average of one by applying a x40 long distance (LD) C-Apochromat 40/1.1 water objective. The emissions were collected using external

detectors [nondescanned detectors with filter set 1 (green channel): beamsplitter 500–550 and long pass (LP) 555 and filter set 2 (red channel): beam- splitter P 565–610 including mirror]. The detector settings were kept constant for all measurements: for the green and red channels, respectively, the master gain was 600/600, the digital gain was 10/10, and the offset was -0.0/0.0. To label the vasculature, a 25 mg/mL solution of FITC-500 kDa Dextran conjugate dissolved in PBS was first concentrated using Nanosep Centrifugal (VWR International, Darmstadt, Germany) and injected intravenously (0.37 µL/g body weight). The fluorescence was detected using the green channel. After 1 min, the β_2-microglobulin-Alexa Fluor 546 dissolved in PBS was injected intravenously (1.56 µL/g body weight) and the proximal tubular β_2-microglobulin uptake was measured as the increase in the tubular fluorescence intensity during the 40 min after injection. The fluorescence was detected using the red channel.

3.2.9.3 Data evaluation

The mean fluorescence intensity of β_2-microglobulin-Alexa Fluor 546 measured in 3–6 proximal tubules per animal overtime (40 min, 20 images) and the background readings for the proximal tubular autofluorescence before β_2-microglobulin-Alexa Fluor 546 injection were assessed using ImageJ V1.37c.

The reabsorption capacity of the proximal tubules was compared after 2, 4 and 40 min of β_2-microglobulin-Alexa Fluor 546 injection, by assessing the mean fluorescence intensity of β_2-microglobulin per tubule and subtracting the background fluorescence.

3.2.10 Determination of protein stability

To determine the stability of WT-hEHD1 and R398W-hEHD1, LLC-PK1 cells were grown in p35 mm Petri dishes and induced with tetracycline (1 µg/mL) for two days. Afterwards, tetracycline was removed and proteins were isolated from cells on the same day and after 1, 2, 4, 5, 7, 10 and 12 days of tetracycline removal. The protein expression of β-actin, WT- and R398W-EHD1 was analyzed by Western blot in all the samples and the detected bands were quantified using ImageJ V1.37c.

3.2.11 Transepithelial transport of bovine serum albumin (BSA) by LLC-PK1 cells

For this experiment cells were cultivated for three weeks in Millicell® Cell Culture Inserts with a pore size of 0.4 µm and the cell growth was monitored by the measurement of the transepithelial resistance (200–400 Ω/cm^2 after three weeks on inserts). After three weeks, the cells were induced for two days with tetracycline (1 µg/mL) for WT- and

R398W-hEHD1 expression. On the day of the assay, the cells were starved for 5 h in Opti-MEM (reduced serum medium) and then incubated at 37°C and 5% CO_2 with BSA-FITC (25 µg/mL) diluted in Opti-MEM on the apical side and with BSA-Alexa Fluor® 594 (25 µg/mL) on the basolateral side. A 10 µL sample was collected, from both apical and basolateral compartments, after 1 h and 5 h of incubation and the fluorescence for both dyes was measured with the NanoDrop 3300. As control for free transport of the dyes across the insert, an empty insert was used and was subjected to the same protocol. Basolaterally applied BSA- Alexa Fluor® 594 was used as control for the epithelium leakage, since that a tight epithelium should not allow the transport of this dye from the basolateral to the apical side. The presence of BSA-FITC on the basolateral side was then used as a measure of transepithelial transport.

3.2.12 β_2-microglobulin uptake by LLC-PK1 cells

Cells were cultivated for three weeks in Millicell® Cell Culture Inserts with a pore size of 0.4 µm and the cell growth was monitored by the measurement of the transepithelial resistance (200–400 Ω/cm^2 after three weeks on inserts). After three weeks, the cells were induced for two days with tetracycline (1 µg/mL) for WT- and R398W-hEHD1 expression. For the assay, the cells were starved for 5 h in Opti-MEM and then incubated at 37°C and 5% CO_2 with β_2-microglobulin-Alexa Fluor® 546 (1:100) diluted in Opti-MEM on the apical side and with BSA-FITC (25 µg/mL) diluted in Opti-MEM on the basolateral side for 5 h. A 10 µL sample was collected, from both apical and basolateral compartments, after 1 h and 5 h of incubation and the fluorescence for both dyes was measured with the NanoDrop 3300. As control for free transport of the dyes across the insert, an empty insert was used and was subjected to the same protocol. Basolaterally applied BSA-FITC was used as control for the epithelium leakage. After 5 h, the cells were thoroughly washed with PBS and proteins were collected in 100 µL co-immunoprecipitation lysis buffer supplemented with protease inhibitor, using a cell scraper. The protein samples were then submitted to the protocol previously described. The concentration of reabsorbed β_2-microglobulin was analyzed by Western blot using a rabbit antibody against β_2-microglobulin. The detected bands were quantified using ImageJ V1.37c and normalized to β-actin expression.

3.2.13 Statistics

Data are shown in mean values ± standard error of the mean (SEM); “n” stands for the number of observations. Unpaired Student’s t-tests were used to calculate significance between different groups. A p-value ≤ 0.05 was accepted to indicate statistical

significance, which was identified by an asterisk (*). The Statistics were performed using Origin V94E software.

4. Results

4.1 Expression and localization of EHD1 in the mouse tissues

The following set of experiments aimed at investigating *Ehd1* gene expression and protein localization in several mouse tissues. EHD1 localization in the testis and the kidney was studied in more detail.

4.1.1 *Ehd1* mRNA levels in the mouse

Ehd1 mRNA levels in different mouse tissues were addressed by real time PCR using specific primers (Figure 4.1). As shown in Figure 4.1, *Ehd1* has a broad tissue expression. It is expressed at high levels in the testis. *Ehd1* expression in the kidney is also relatively high when compared to the other tissues.

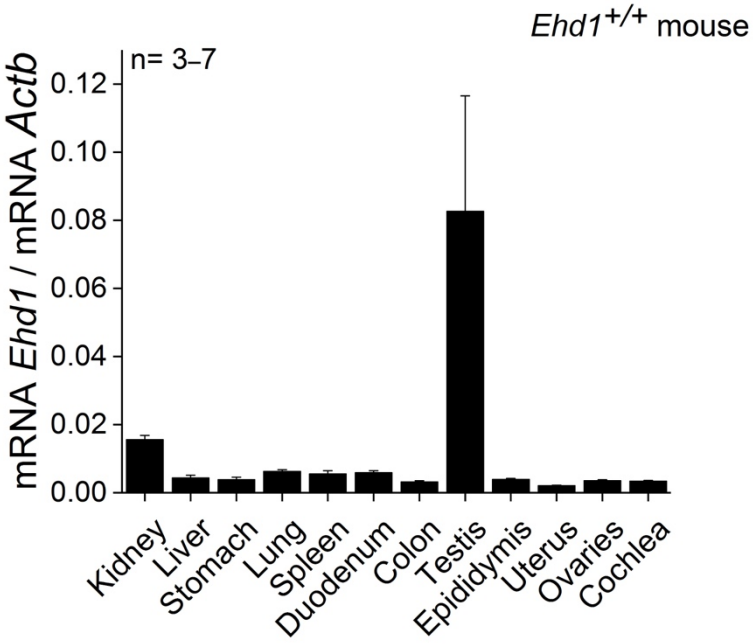

Figure 4.1: *Ehd1* mRNA levels in wildtype mouse tissues.
Ehd1 mRNA levels were quantified by real time PCR and normalized to *Actb* (β-actin) mRNA levels. *Ehd1* displays a broad tissue expression. The highest mRNA levels were detected in the testis and in the kidney. Values are expressed as the mean ± SEM. n= number of mice measured per tissue.

4.1.2 EHD1 localization in mouse tissues on the cellular level

EHD1 localization in several mouse tissues was investigated using *Ehd1* promotor-driven X-Gal staining (Figure 4.2). The X-Gal staining takes advantage of the *LacZ* gene product (β-galactosidase) ability to hydrolyze X-Gal, resulting in a product with blue color. As

previously mentioned, by placing the *LacZ* gene under the control of the *Ehd1* promotor, the blue stain can be used as marker for EHD1 localization.

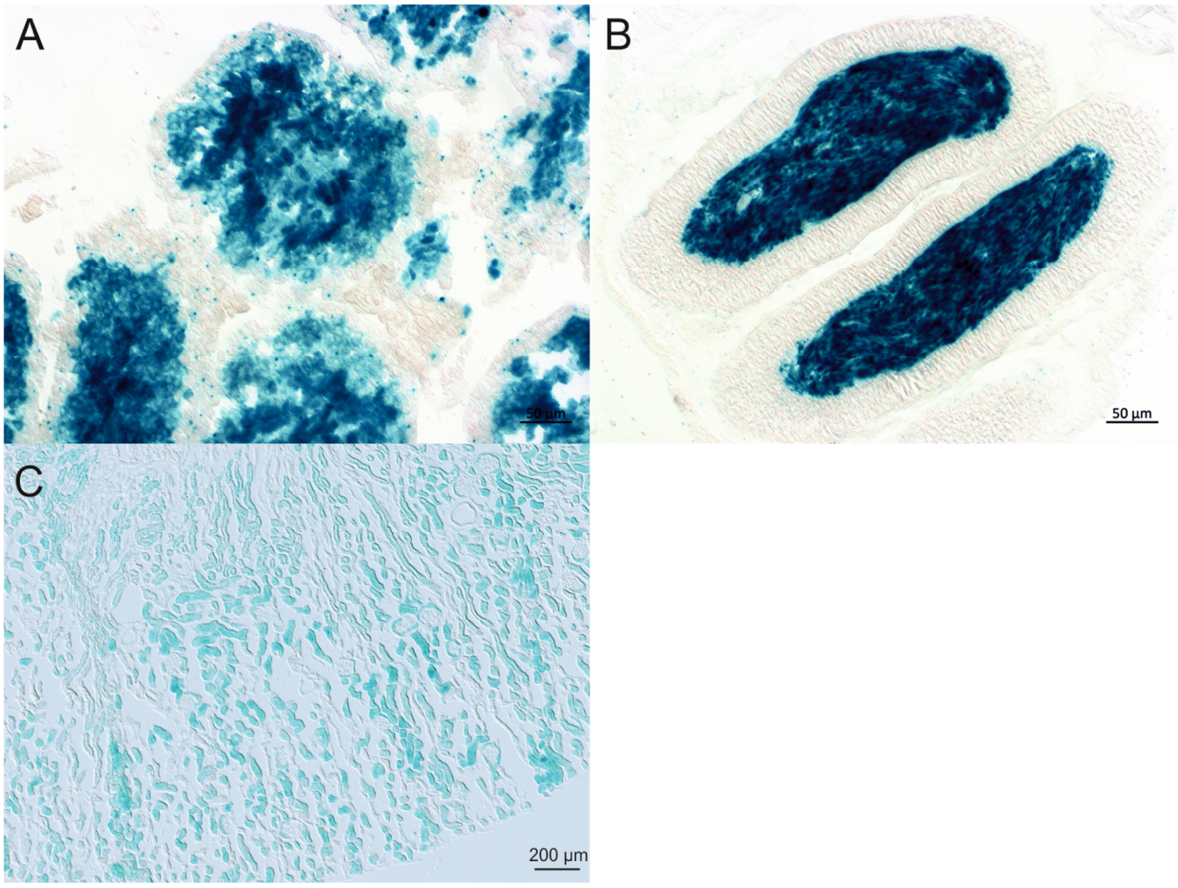

Figure 4.2: *Ehd1* promotor-driven X-Gal staining in adult *Ehd1*$^{+/-}$ mouse tissues.
Ehd1 promotor-driven X-Gal staining (blue) of a transgenic *Ehd1*$^{+/-}$ mouse carrying a *LacZ* gene within the *Ehd1* gene locus. A, Testis. B, Epididymis. C, Kidney.

In an adult *Ehd1*$^{+/-}$ mouse, a blue staining was observed throughout the seminiferous tubules in the testis (Figure 4.2 A). The dark blue staining near the tubule lumen suggests that EHD1 is mostly present in cells in a late stage of spermatogenesis. In the epididymis (Figure 4.2 B), the blue color was found in the stored spermatozoa. In the kidney (Figure 4.2 C), the blue staining was seen in the cortex and outer medulla regions.

4.1.2.1 EHD1 localization in the testis

The localization of the EHD1 protein in the testis was studied in more detail using immunofluorescence (Figure 4.3). A specific signal was obtained, with an antibody against EHD1, in the testis of a *Ehd1*$^{+/+}$ mouse that was absent in the *Ehd1*$^{-/-}$ mouse. EHD1 was observed in the seminiferous tubules in the layer of cells closer to the lumen (Figure 4.3, arrow), which suggests an EHD1 localization in cells at a later stage of spermatogenesis, such as spermatids and spermatozoa. The signal observed in the interstitial space seemed to be unspecific, since it was detected in both wildtype and knockout mice.

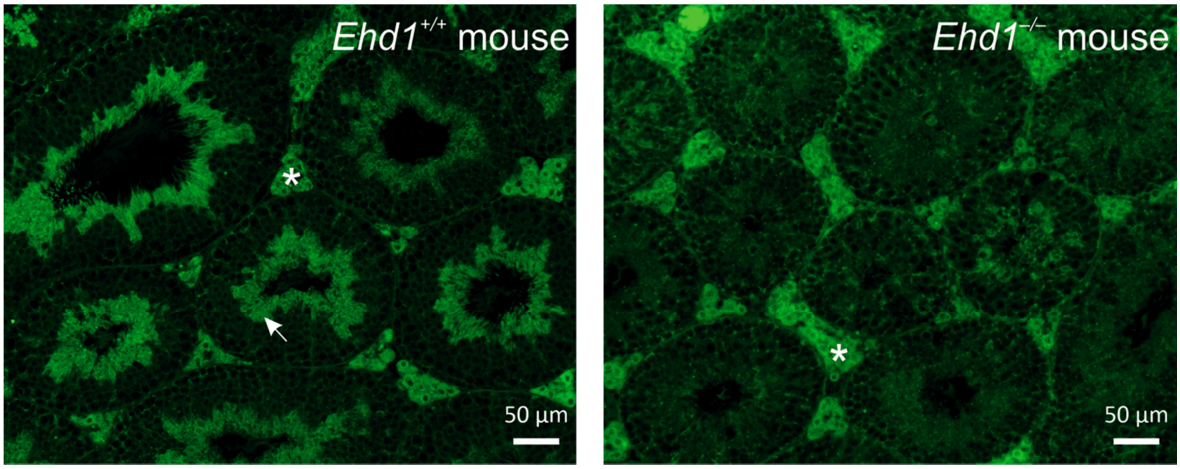

Figure 4.3: EHD1 localization in the seminiferous tubules of adult mice.
Immunofluorescence of EHD1 (green) in paraffin sections of *Ehd1*$^{+/+}$ (left) and *Ehd1*$^{-/-}$ (right) mouse testes. EHD1 staining seemed to be unspecific in cells of the interstitial space (*). However, a specific signal was observed in the seminiferous tubules (arrow), in cells at later stages of spermatogenesis (spermatids and spermatozoa).

4.1.2.2 EHD1 localization in the kidney

The localization of EHD1 in the kidney was previously addressed [91]. However, the next experiments aimed to investigate, in more detail, this kidney localization using immunofluorescence and colocalization with protein markers.

The EHD1 staining in the mouse kidney (Figure 4.4) displayed a specific signal in the renal proximal tubules, throughout the kidney cortex and outer medulla.

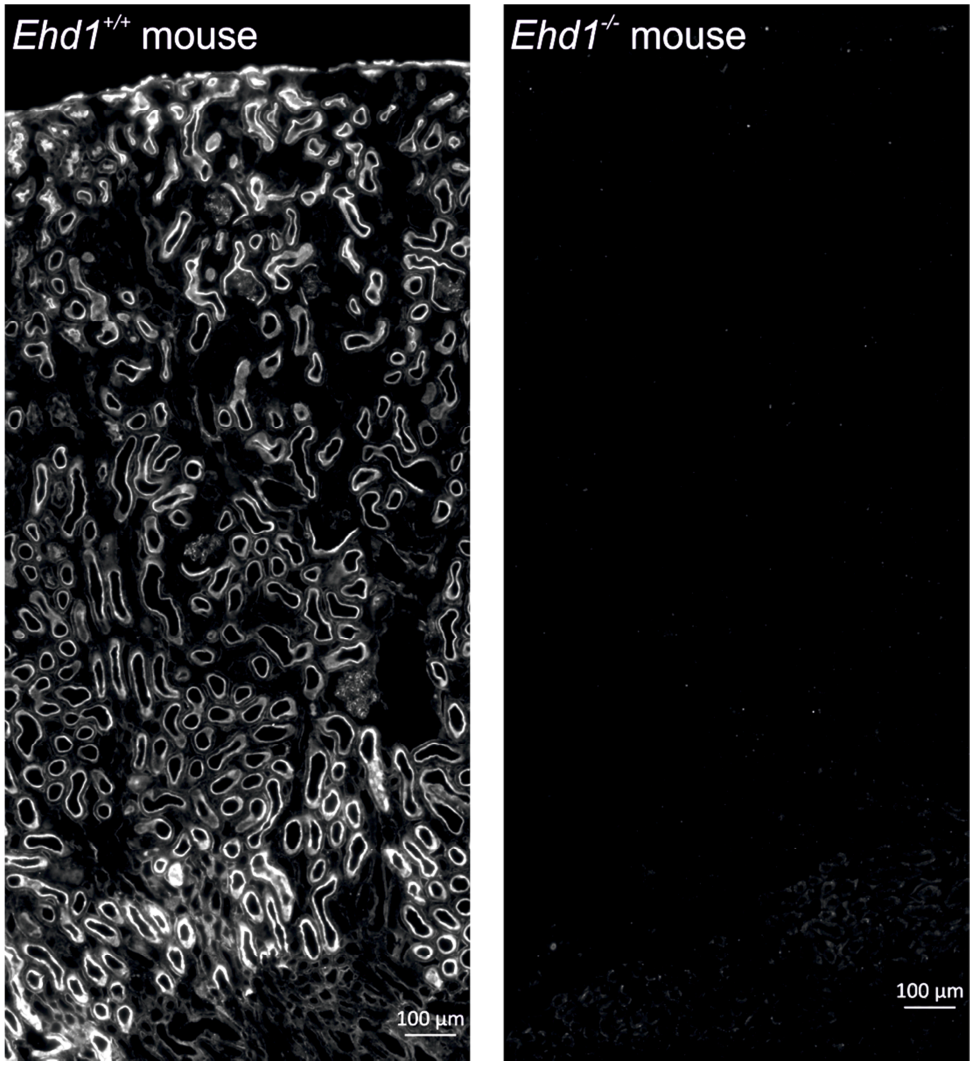

Figure 4.4: EHD1 localization in the renal proximal tubules of adult mice.
Immunofluorescence of EHD1 in cryo sections of *Ehd1*$^{+/+}$ (left) and *Ehd1*$^{-/-}$ (right) mouse kidneys. EHD1 is localized in the proximal tubules in the renal cortex and outer medulla. The lack of EHD1 staining in the *Ehd1*$^{-/-}$ mouse confirms the efficiency of the knockout and the specificity of the immunostaining.

In the proximal tubules, EHD1 exhibited a colocalization with megalin, a marker for the proximal tubules brush border and one of the two main receptors responsible for protein reabsorption (Figure 4.5). This overlapping localization was not only observed in mouse kidney (Figure 4.5 A, B), but also in human kidney (Figure 4.5 C). The colocalization between EHD1 and the lysosome-associated membrane glycoprotein 1 (LAMP1) was also assessed. The vesicle-like staining of LAMP1 did not colocalize with EHD1, the LAMP1 lysosomes presented instead a sub-membranous and more cytoplasmic localization (Figure 4.5 A, B). This suggests that EHD1 is not associated with lysosomal vesicles.

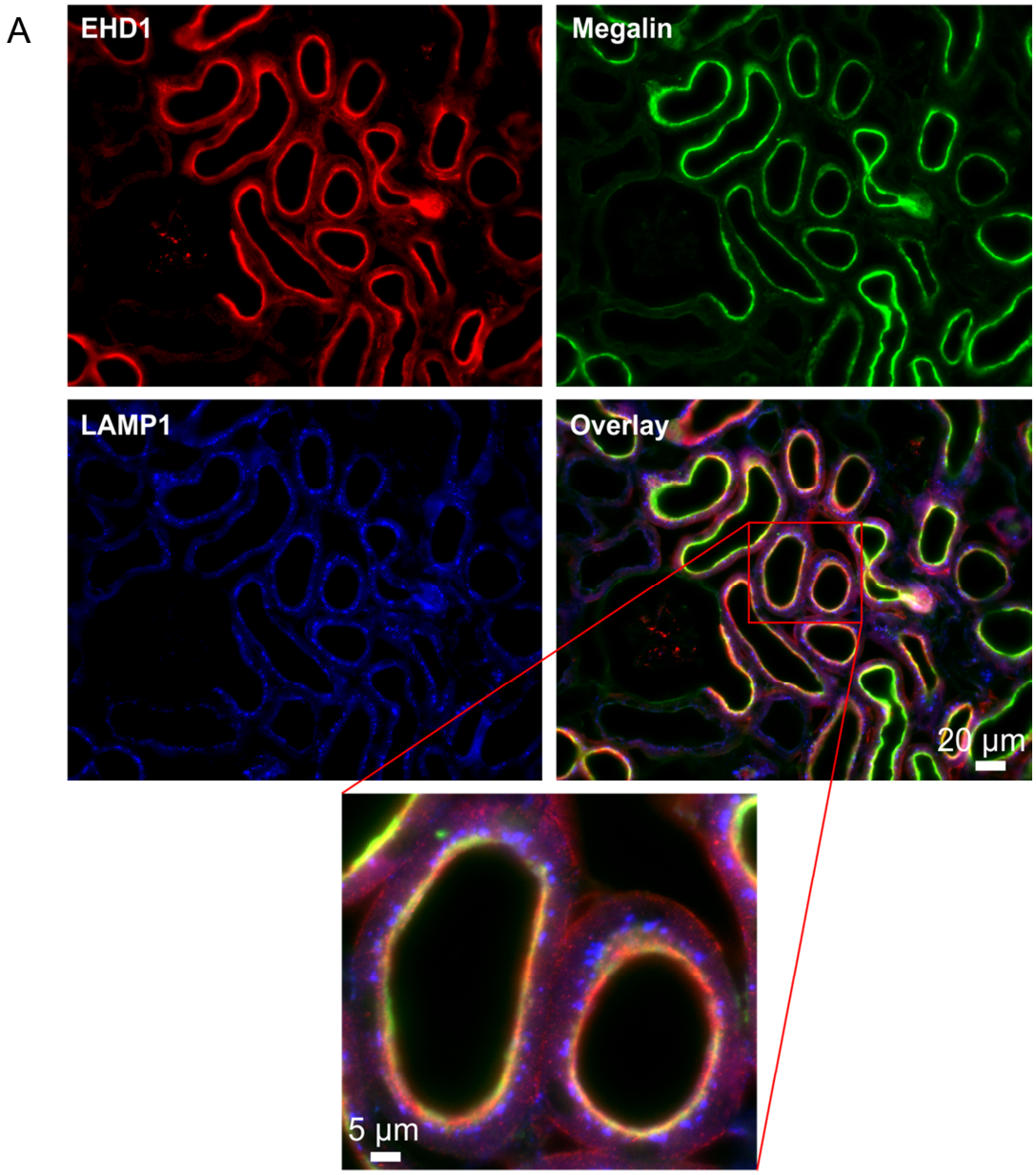
A
EHD1
Megalin
LAMP1
Overlay
20 µm
5 µm

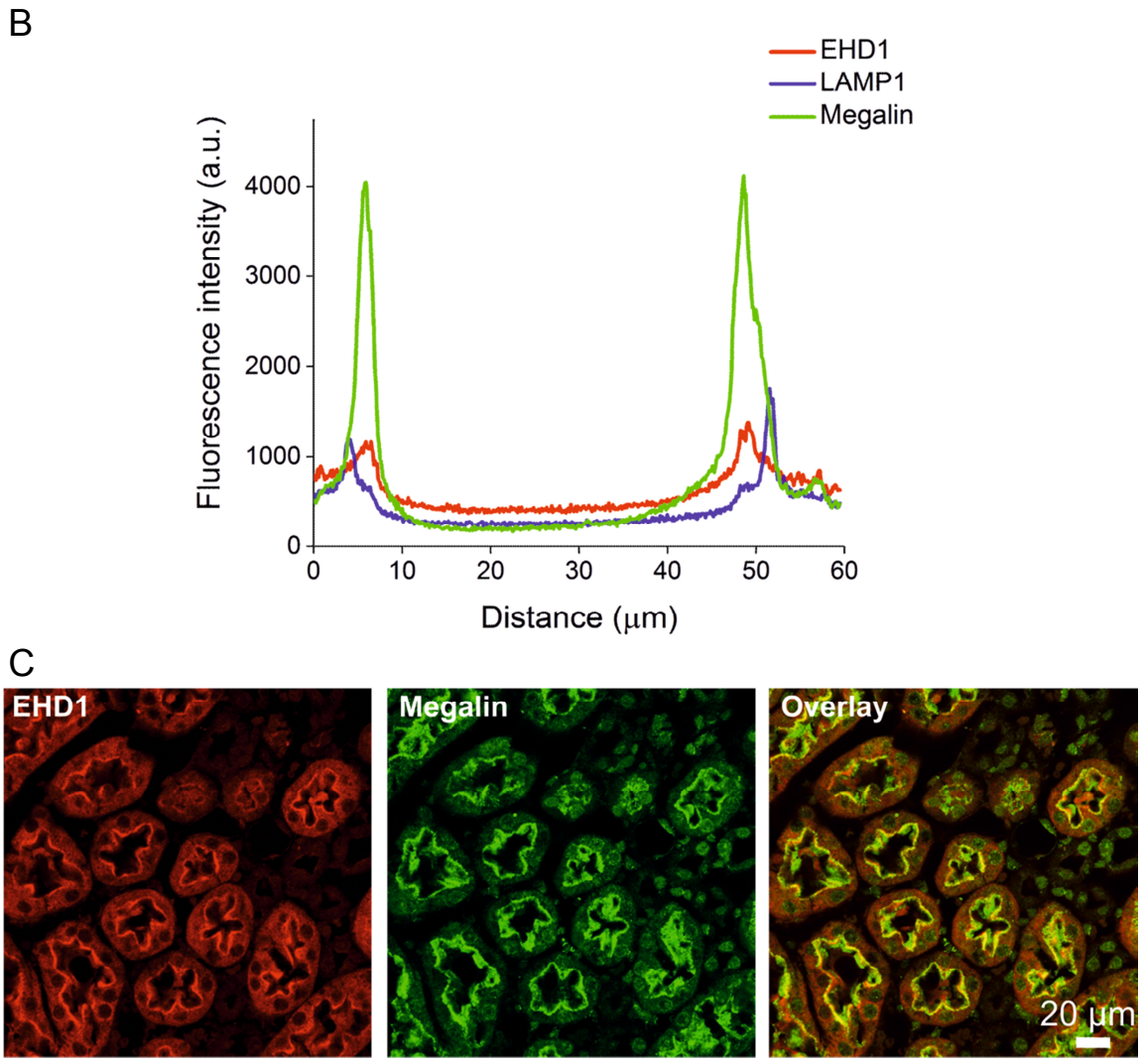

Figure 4.5: EHD1 colocalization with Megalin.
A, Immunofluorescence of EHD1 (red), megalin (green) and LAMP1 (blue) in cryo section of *Ehd1*$^{+/+}$ mouse kidney. B, Representative measurement of EHD1 and megalin colocalization. C, Immunofluorescence of EHD1 and megalin in paraffin section of human kidney.
EHD1 seemed to colocalize with megalin at the brush border of the proximal tubules in both mouse and human kidneys.

Due to the observed colocalization of megalin and EHD1, an interaction between these two proteins was assessed by performing a co-immunoprecipitation (Figure 4.6). Proteins were isolated from the mouse kidney tissue in non-denaturating conditions and submitted to the immunoprecipitation protocol. EHD1 and megalin were detected by Western blot in protein samples where megalin (Figure 4.6, left panel) and EHD1 (Figure 4.6, right panel), respectively, were immunoprecipitated. The observed co-immunoprecipitation confirms the interaction between EHD1 and megalin.

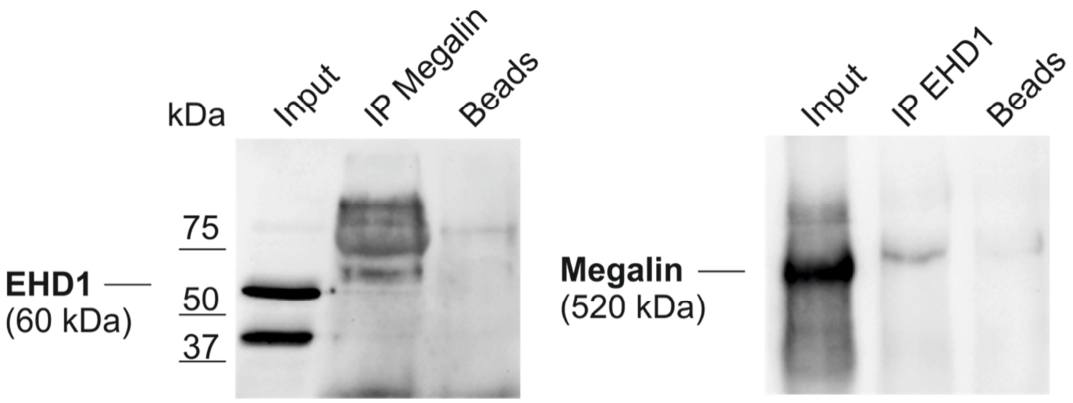

Figure 4.6: EHD1 interaction with megalin in *Ehd1*$^{+/+}$ mouse kidney.
Representative Western blot of co-immunoprecipitation of EHD1 (left) and megalin (right) in mouse kidney lysates (input). Pull down was performed with either anti-Megalin antibody (left) or anti-EHD1 antibody (right). As a negative control the mouse kidney lysate was incubated with protein-bound beads without the pull down antibody and submitted to the same protocol as the other probes. In both cases, interactions of EHD1 and megalin could be verified.

At the plasma membrane, EHD1 was also found to colocalize with cubilin, the other main receptor for protein endocytosis in the proximal tubules (Figure 4.7).

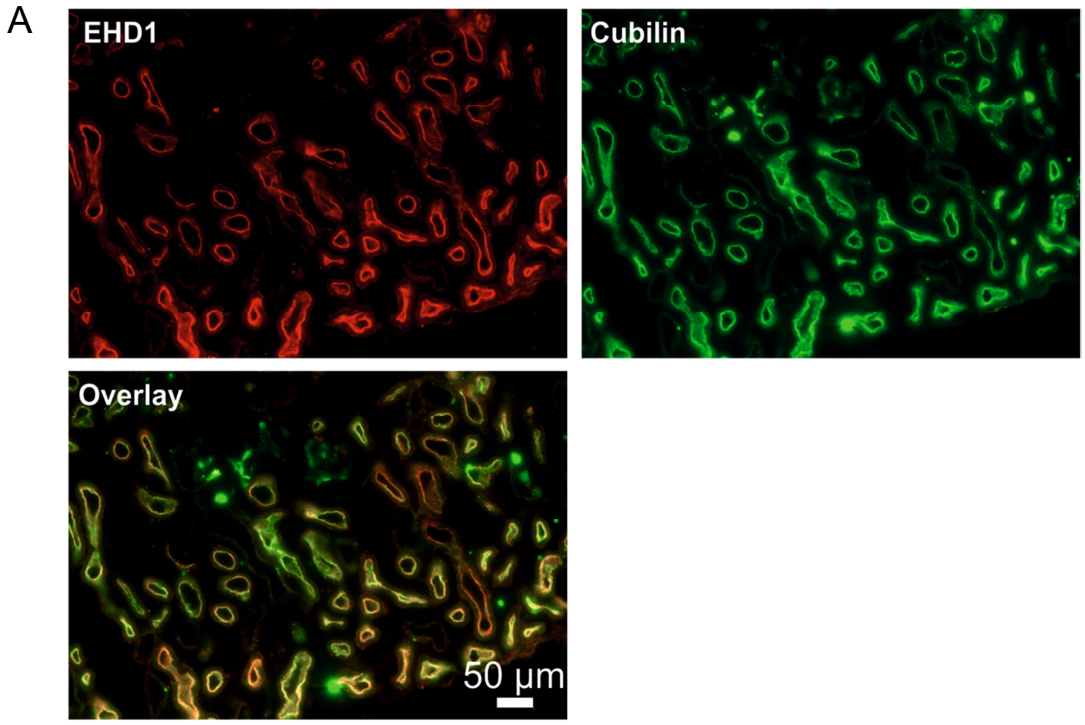

B

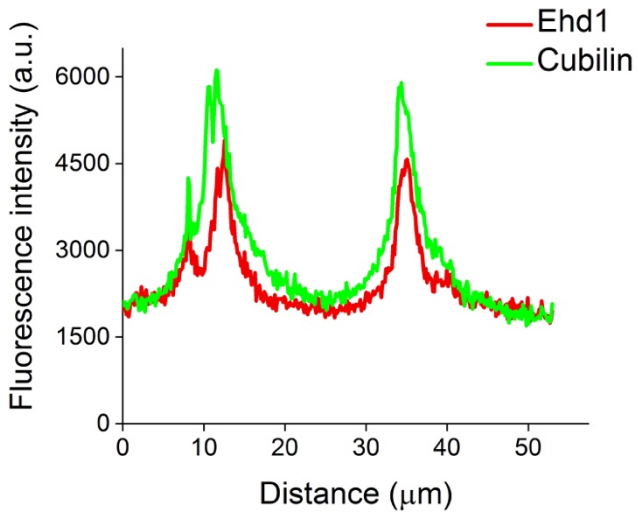

Figure 4.7: EHD1 colocalization with Cubilin
A, Immunofluorescence of EHD1 (red) and cubilin (green) in cryo section of *Ehd1*$^{+/+}$ mouse kidney. B, Representative measurement of EHD1 and cubilin colocalization.
EHD1 seemed to colocalize with cubilin at the brush border of the proximal tubules in mouse kidney.

4.2 Characterization of the *Ehd1*$^{-/-}$ mouse phenotype

The phenotype of the *Ehd1*$^{-/-}$ mouse is still a matter of controversial discussion. Two different mouse models were published displaying inconsistent phenotypes [54,77]. While one mouse presented no clear phenotype [54], the other showed a number of abnormalities, such as higher mortality rate, smaller size, male infertility and ocular defects [11,77]. It was further reported that the effect of EHD1 loss in the mouse phenotype is dependent on the mouse background [79], since the *Ehd1* knockout seemed lethal in a predominantly C57BL6 background but not on other strains. The C57BL6 *Ehd1*$^{-/-}$ mice displayed already at the embryonic level, severe problems in completing key developmental processes including neural tube closure, axial turning and patterning of the neural tube [79].
The *Ehd1*$^{-/-}$ mouse used in this project was a different model from the others already published. It was generated by deletion of the exon 2 of *Ehd1* and had a mixed C57BL6;129S background. The phenotype of this new mouse model was studied with the focus on inner ear function, testis and kidney.

4.2.1 Generation of *Ehd1*$^{-/-}$ mouse

The *Ehd1*$^{-/-}$ mouse was generated as described in Materials and Methods (Figure 3.1). A real time PCR analysis of genomic DNA using specific oligonucleotides for the wildtype and knockout alleles was used for the mice genotyping as heterozygous (*Ehd1*$^{+/-}$), homozygous deleted (*Ehd1*$^{-/-}$) or homozygous wildtype (*Ehd1*$^{+/+}$). The absence of *Ehd1*

mRNA transcript in the *Ehd1*$^{-/-}$ mouse was confirmed by real time PCR in several tissues in comparison to wildtype tissues (Figure 4.8). The lack of EHD1 protein in the testis (Figure 4.3 right) and kidney (Figure 4.4 right) was also observed using immunofluorescence.

These results demonstrated that the targeting strategy led to complete loss of EHD1 expression in *Ehd1*$^{-/-}$ mouse tissues.

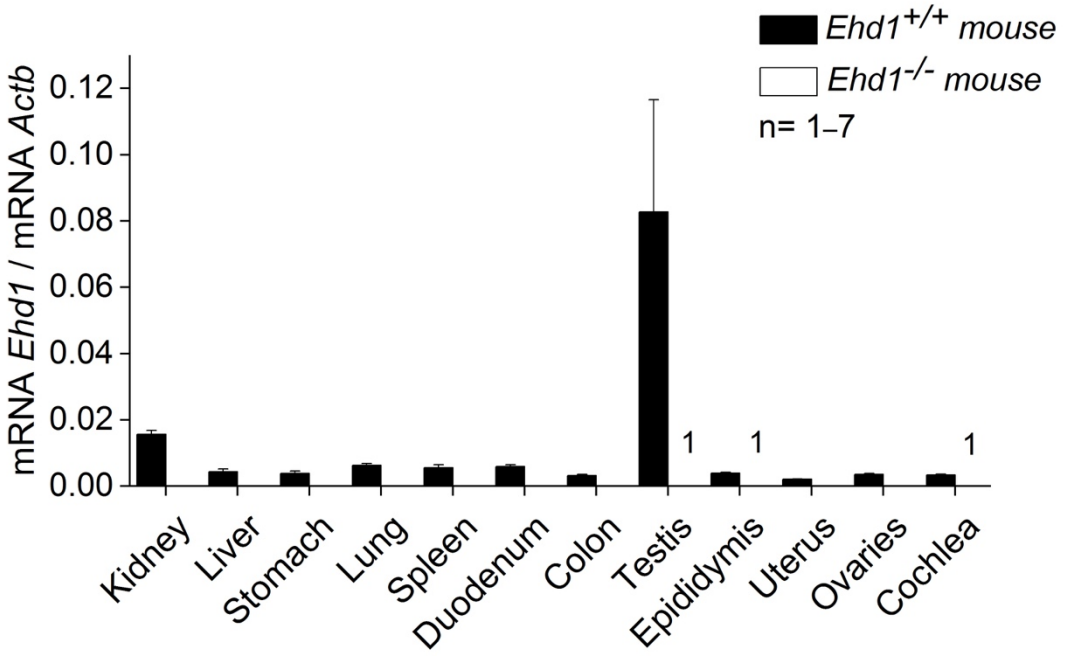

Figure 4.8: *Ehd1* mRNA levels in *Ehd1*$^{-/-}$ mouse tissues compared to *Ehd1*$^{+/+}$.
Ehd1 mRNA levels were quantified by real time PCR and normalized to β-actin mRNA levels. *Ehd1* mRNA is almost absent in the knockout tissues when comparing the levels to the wildtype. Values are expressed as the mean ± SEM. n= number of mice measured per tissue.

4.2.2 Basic phenotype of the *Ehd1*$^{-/-}$ mouse

The study of the *Ehd1*$^{-/-}$ mouse phenotype started with the investigation of the possible effect of EHD1 loss on animal survival. The progeny from *Ehd1*$^{+/-}$ breeding pairs on mixed C57BL6;129S background was 49% female and 51% male with the expected Mendelian ratios for *Ehd1*$^{+/-}$ and *Ehd1*$^{+/+}$ mice, indicating normal gender ratios and the absence of lethality when one copy of *Ehd1* was present (Table 4.1). However, the percentage of *Ehd1*$^{-/-}$ newborns was lower than the expected Mendelian ratio (10,3% instead of 25%; Table 4.1), but with normal gender ratios (55% males and 45% females). These results suggest that the *Ehd1* knockout is partially lethal, and that lethality is independent of the gender.

Table 4.1: Genotypes of pups obtained from *Ehd1* mutant mouse breeding pairs.

n	Female	Male	*Ehd1*$^{+/+}$ pups	*Ehd1*$^{+/-}$ pups	*Ehd1*$^{-/-}$ pups	Total pups
6	*Ehd1*$^{+/-}$	*Ehd1*$^{+/-}$	60 (28.0%)	132 (61.7%)	22 (10.3%)	214
1	*Ehd1*$^{-/-}$	*Ehd1*$^{+/-}$	0	4 (80.0%)	1 (20.0%)	5
3	*Ehd1*$^{+/+}$	*Ehd1*$^{-/-}$	0	0	0	0

n= number of breeding pairs, % was calculated for each genotype based on total pups for each breeding scheme.

Although EHD1 loss seemed to have a similar effect on both genders lethality, the effect on fertility was more severe in the male knockouts. The adult *Ehd1*$^{-/-}$ males were housed for 2 months with two adult females, that had already given birth before. However, the knockout male mice were not able to produce offspring, indicating that *Ehd1*$^{-/-}$ males were infertile (Table 4.1). On the other hand, the *Ehd1*$^{-/-}$ females showed to be fertile by producing offspring when crossed with *Ehd1*$^{+/-}$ males (Table 4.1).

The body weight of four-month-old male mice was also measured and compared between controls and knockouts (Figure 4.9). The *Ehd1*$^{-/-}$ mice exhibited only a small reduction in body weight that was not significantly different from the control mice.

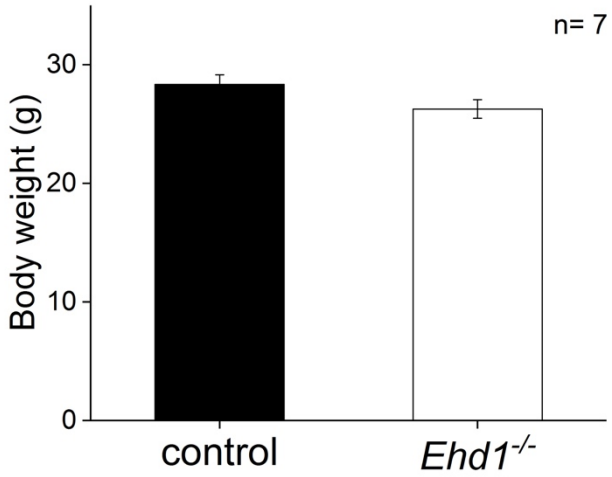

Figure 4.9: *Ehd1*$^{-/-}$ mice body weight compared to control mice.
The body weight of four-month-old male *Ehd1*$^{-/-}$ and control mice was measured and both groups exhibited a similar size, with the knockouts displaying only a small reduction in the body weight. Values are expressed as the mean ± SEM. n= number of mice measured per group. Unpaired Student's t-test was used for calculation of significance between groups.

4.2.3 Eye phenotype of the *Ehd1*$^{-/-}$ mouse

In this project, the eye phenotype was only briefly addressed. The knockout mice were checked for ocular abnormalities, which were then photographed for documentation. However, no further histological characterization of these abnormalities was performed. It

was observed that around $^1/_3$ of the knockout mice (13 animals in total were evaluated) exhibited eye problems, while no anomalies were displayed by the wildtype animals. These mice displayed abnormalities, such as anophthalmia, microphthalmia and cataracts (Figure 4.10). These observations suggest a similar eye phenotype to the one previously reported[11], although with lower frequency.

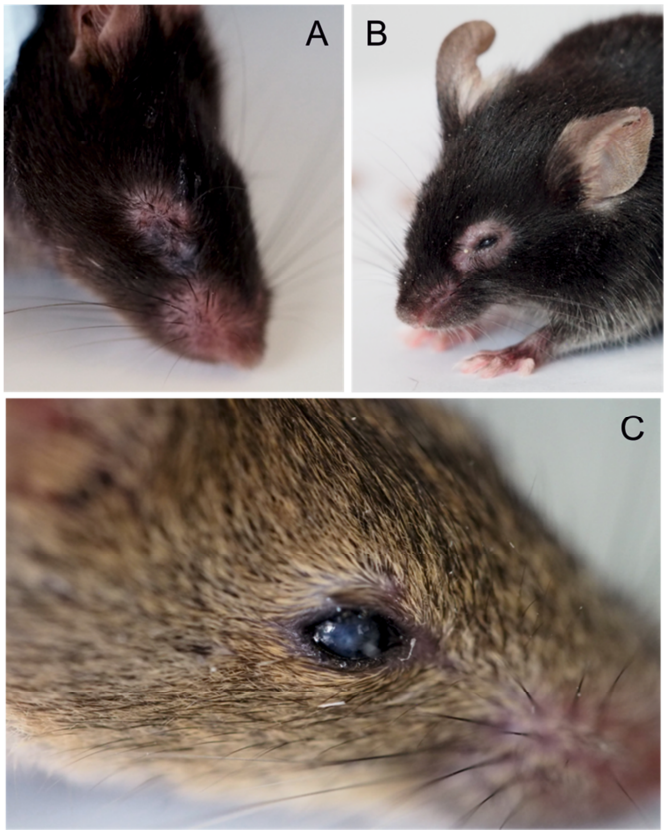

Figure 4.10: Ocular abnormalities in the *Ehd1*$^{-/-}$ mouse.
A, Anophthalmia, B, microphthalmia and C, cataracts observed in the *Ehd1*$^{-/-}$ mice. Representative ocular abnormalities that were observed in *Ehd1*$^{-/-}$ mice. $^1/_3$ of *Ehd1*$^{-/-}$ showed eye abnormalities like A, B and C while no significant anomalies were found in the wildtype mice.

4.2.4 Inner ear phenotype of the *Ehd1*$^{-/-}$ mouse

So far, no inner ear phenotype of the *Ehd1*$^{-/-}$ mice had been reported. The following experiments aimed to investigate the effect of *Ehd1* deletion on cochlea histology and hearing ability.

4.2.4.1 Histology of the cochlea in the *Ehd1*$^{-/-}$ mouse

A hematoxylin and eosin staining was used to compared the histology of the cochlea of the *Ehd1*$^{-/-}$ to the *Ehd1*$^{+/-}$ mouse (Figure 4.11). The cochleae of both mice seemed to present a similar histology. However, several complications that did not allow obtaining

cochlea slices of better quality and problems with EHD1 antibody specificity (Figure 4.12) prevented a more thorough analysis of histology and EHD1 localization in the inner ear.

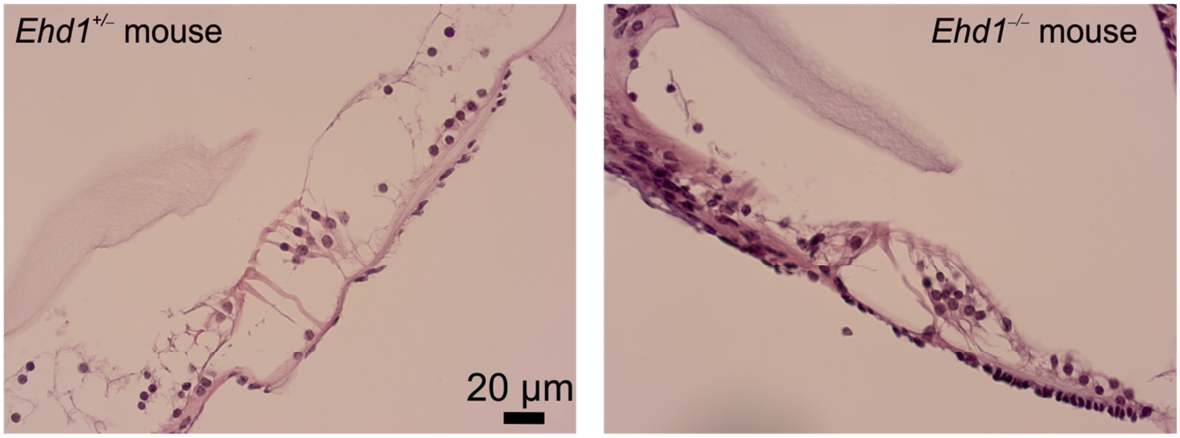

Figure 4.11: Histology of the cochlea in the *Ehd1*$^{-/-}$ mouse compared to the control.
Hematoxylin and eosin staining in paraffin sections of *Ehd1*$^{+/-}$ (left) and *Ehd1*$^{-/-}$ (right) mouse cochleae. The histology of the knockout cochlea seemed not to differ from the control mouse.

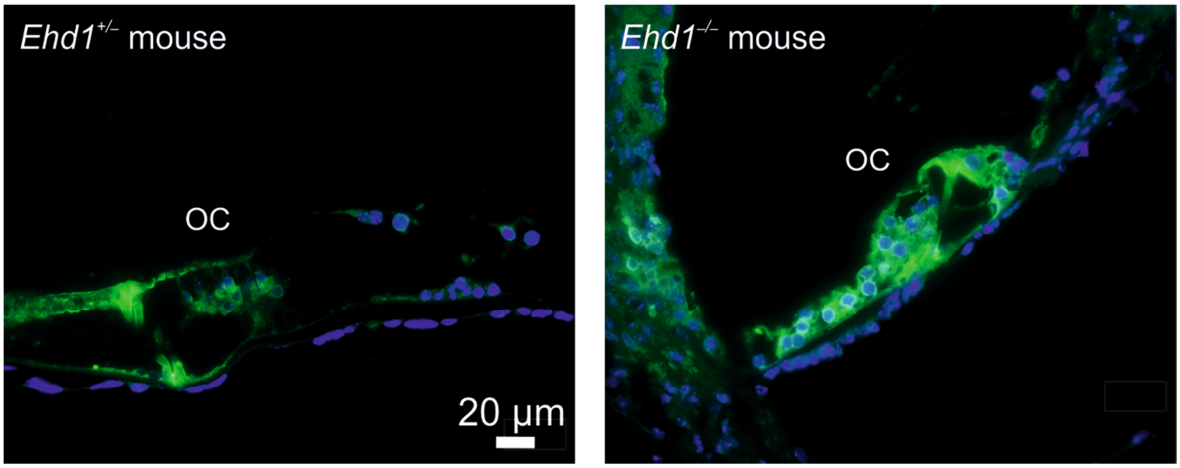

Figure 4.12: Unspecific EHD1 antibody binding in the mouse cochlea.
Immunofluorescence of EHD1 (green) in paraffin sections of *Ehd1*$^{+/-}$ (left) and *Ehd1*$^{-/-}$ (right) mouse cochleae. An unspecific binding of the EHD1 antibody in the organ of Corti (OC) was observed. Both *Ehd1*$^{+/-}$ and *Ehd1*$^{-/-}$ cochleae presented a fluorescent signal, however the absence of *Ehd1* mRNA in the cochlea of knockout mice was previously confirmed (Figure 4.8).

4.2.4.2 Measurement of the *Ehd1*$^{-/-}$ mouse hearing ability

The mice hearing ability was assessed using frequency-specific auditory brainstem response (f-ABR) measurements (Figure 4.13) in collaboration with the group of Prof. Dr. Holger Schulze (Department of Otorhinolaryngology-Head and Neck Surgery, University Hospital Erlangen). The f-ABR thresholds were evaluated at intermediate frequencies (11 and 22 kHz) and at a high frequency (32 kHz) in both control (*Ehd1*$^{+/+}$ + *Ehd1*$^{+/-}$) and *Ehd1*$^{-/-}$ groups. Both groups showed no difference in mean f-ABR thresholds for the tone frequencies at 11 and 22 kHz. However, at a higher frequency there was a tendency for the f-ABR threshold of the knockout mice to be higher than the control group, suggesting

potential hearing loss at high frequencies in the *Ehd1*$^{-/-}$ mice. This result is in agreement with the inner ear phenotype displayed by the human patients pointing to a possible role of EHD1 in the auditory pathway.

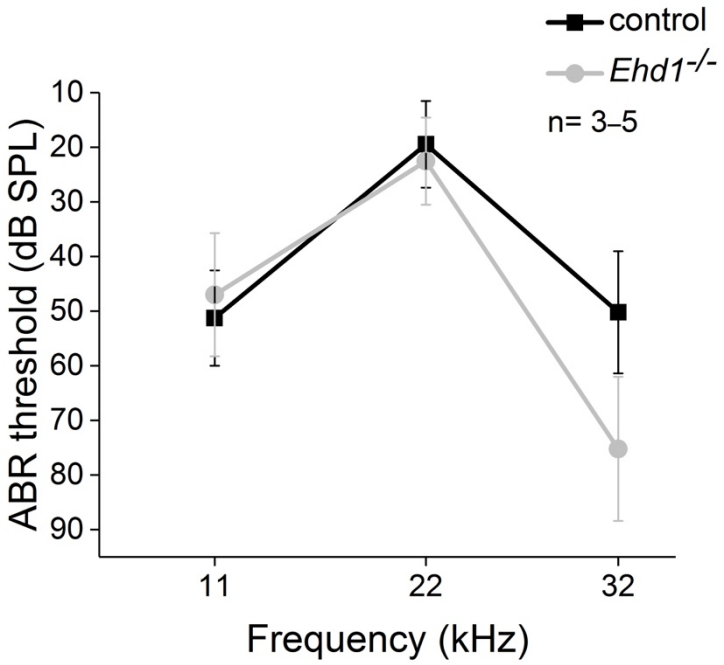

Figure 4.13: Comparison of hearing ability of the *Ehd1*$^{-/-}$ mouse to the control.
f-ABR hearing thresholds at 11, 22 and 32 kHz in *Ehd1*$^{-/-}$ and control mice. The knockout mice showed a tendency for hearing loss at high frequency when compared to the control mice. Values are expressed as the mean ± SEM. n= number of mice measured per frequency for each group. Unpaired Student's t-test was used for calculation of significance between groups.

4.2.4.3 Effect of *Ehd1* deletion on gene expression in the cochlea

The possibility of compensation of the EHD1 loss by another EHD homologue was investigated.

The effect of *Ehd1* deletion on the regulation of *Ehd3* gene expression was assessed by real time PCR (Figure 4.14). No significant upregulation of the *Ehd3* transcript in the *Ehd1*$^{-/-}$ mouse was observed. This suggests that EHD3 does not seem to compensate for EHD1 absence. The effect on *Ehd2* and *Ehd4* gene regulation still needs to be addressed.

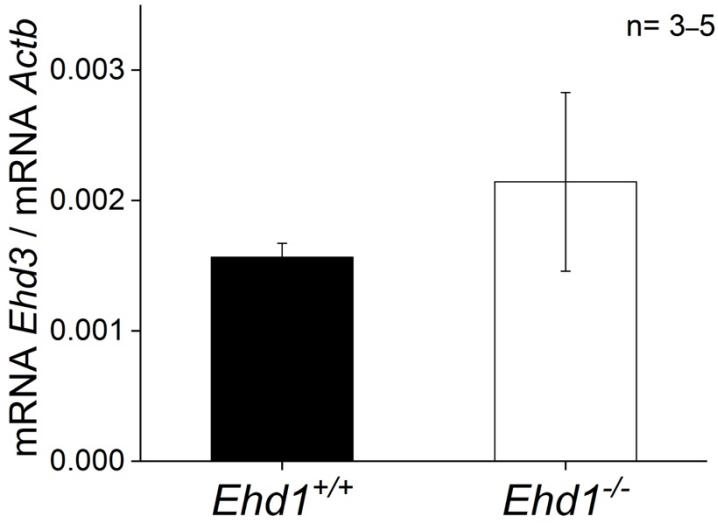

Figure 4.14: *Ehd3* mRNA levels in the *Ehd1*$^{-/-}$ mouse cochlea compared to the control. Quantification by real time PCR of *Ehd3* mRNA levels in the cochlea of *Ehd1*$^{-/-}$ and *Ehd1*$^{+/+}$ mice normalized to β-actin expression. In the cochlea, the absence of EHD1 did not seem to lead to a significant upregulation of the *Ehd3* gene. Values are expressed as the mean ± SEM. n= number of mice measured per group. Unpaired Student's t-test was used for calculation of significance between groups.

4.2.5 Testis and epididymis phenotype of the *Ehd1*$^{-/-}$ mouse

As previously mentioned, despite repeated attempts to mate male *Ehd1*$^{-/-}$ mice, no progeny was generated suggesting infertility of the knockouts. However, when breeding *Ehd1*$^{+/-}$ male with *Ehd1*$^{-/-}$ female mice, pups were born (Table 4.1). These results are similar to the ones already reported for another *Ehd1*$^{-/-}$ mouse line, where only male infertility was described [77]. In order to understand the reasons for male infertility, the histology of the testis and epididymis of the *Ehd1*$^{-/-}$ and control mice was further studied and compared, using Periodic acid–Schiff (PAS) staining and electron microscopy.

4.2.5.1 Size of the testes and epididymides in the *Ehd1*$^{-/-}$ mouse

The weight of testes and epididymides relative to mouse body weight was compared in adult *Ehd1*$^{-/-}$ mice and controls (Figure 4.15). The *Ehd1*$^{-/-}$ mice exhibited always smaller testes (Figure 4.15 right) and a lower weight for both testes and epididymides together (Figure 4.15 left).

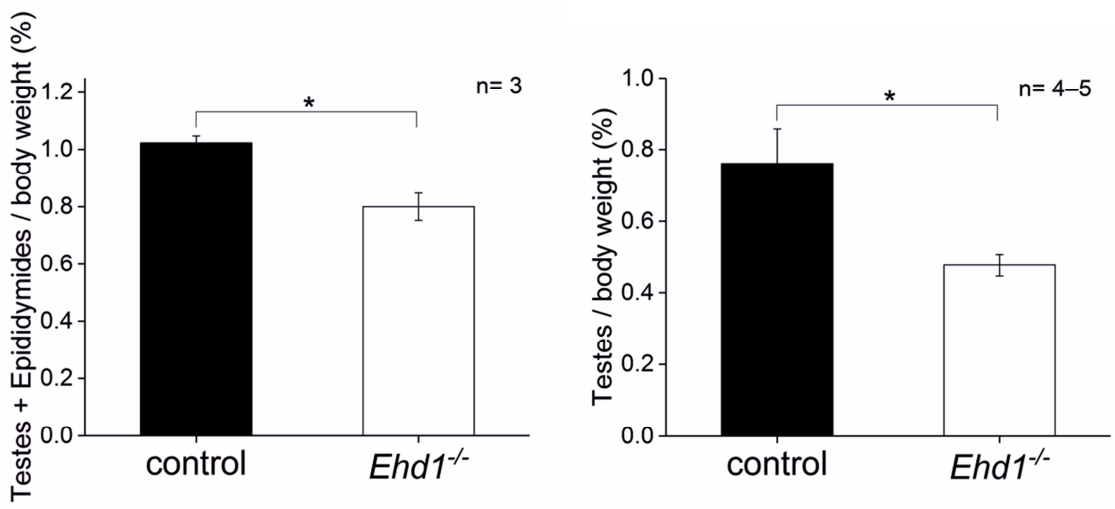

Figure 4.15: Testes and epididymides weight in *Ehd1*$^{-/-}$ mice compared to controls.
After retrograde arterial perfusion and tissue fixation, testis and epididymis were isolated and their weight was compared to the mouse body weight in *Ehd1*$^{-/-}$ and control mice. Both testes and epididymides as well as only testes weight was significantly lower in the knockout animals. Values are expressed as the mean ± SEM. * $p<0.05$, n= number of mice measured per group. Unpaired Student's t-test was used for calculation of significance between groups.

4.2.5.2 Histology of the testis and epididymis in the *Ehd1*$^{-/-}$ mouse

The PAS staining of the testis of the *Ehd1*$^{-/-}$ mouse revealed a very reduced number of elongated spermatids in the seminiferous tubules (Figure 4.16 F, white arrow), as well as Sertoli cell vacuolization (Figure 4.16 F, black arrow) and abnormal meiotic figures (Figure 4.16 F, enlarged region, black arrowhead). Several seminiferous tubules exhibited a disorganized structure, where the several stages of spermatogenesis could not be identified (Figure 4.16 F, seminiferous tubule on the right side). Also in the epididymis, spermatozoa were almost absent (Figure 4.16 E) and instead macrophages were observed (Figure 4.16 E, white arrowheads). The staining on the *Ehd1*$^{+/+}$ mouse exhibited, in contrast to the knockout, a high number of elongated spermatids in almost every seminiferous tubule (Figure 4.16 C, enlarged region, white arrow). Moreover, mature spermatozoa were easily detected in the epididymis (Figure 4.16 B, white arrow).

The spermatozoa motility was also investigated by rinsing the harvested epididymis in a saline buffer solution and observing the spermatozoa under a brightfield inverted microscope. The few spermatozoa obtained from the knockout mice showed no or strongly reduced motility, while the ones isolated from the wildtype epididymis where much more abundant and very active (data not shown). This data suggests a role of EHD1 in spermatogenesis and in sperm cells motility.

In order to identify the defect in spermatogenesis, the ultrastructure of the seminiferous tubules was examined by electron microscopy.

The electron microscopy of the *Ehd1*$^{-/-}$ mouse testis exhibited a somehow more disorganized structure near the lumen of the seminiferous tubules (Figure 4.17 D) when compared to the wildtype tubules structure (Figure 4.17 A). In the *Ehd1*$^{+/+}$ mouse, seminiferous tubules that contained elongated spermatids in the process of spermiation near the lumen were easily observed (Figure 4.17 A, white arrowhead), while in the *Ehd1*$^{-/-}$ mouse most of the spermatids examined presented a rounder or sickle-like shape, were not localized near the seminiferous tubule lumen and the acrosome was almost absent (Figure 4.17 F, white arrow heads). The structures corresponding to the different parts of the spermatozoa, such as end piece, principal piece (Figure 4.17 B) and midpiece (Figure 4.17 C) of the sperm tail were present in the *Ehd1*$^{+/+}$ mouse. However, the spermatozoon spotted in the *Ehd1*$^{-/-}$ mouse seemed to lack a normal midpiece structure, where the mitochondrial sheath is localized that has an important function for generating the energy for sperm flagellar motility.

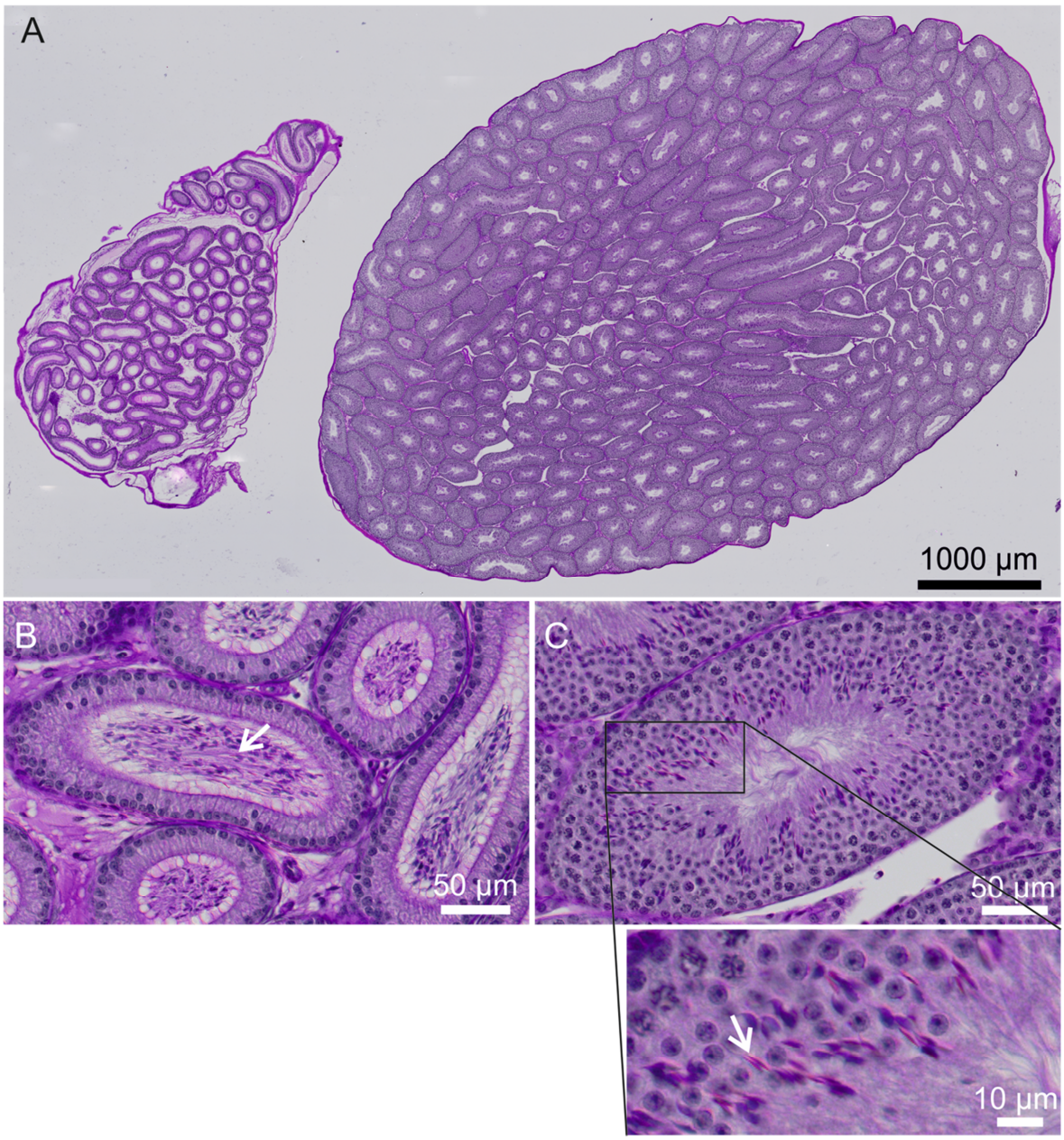
Ehd1$^{+/+}$ mouse
A
1000 µm
B
50 µm
C
50 µm
10 µm

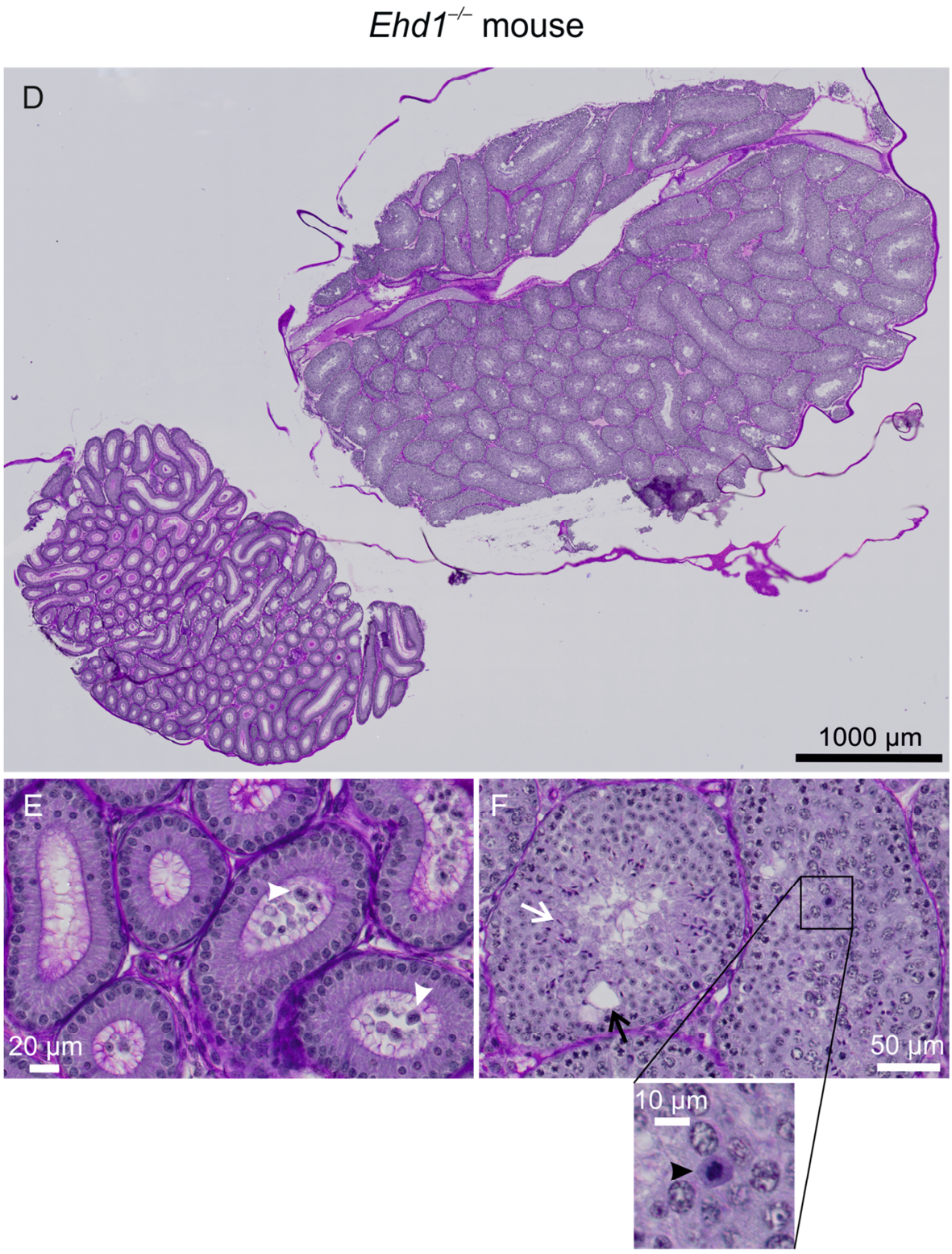

Figure 4.16: Histology of the testis and epididymis in the *Ehd1*$^{-/-}$ mouse compared to the control.
A, D, PAS staining of paraffin sections of *Ehd1*$^{+/+}$ and *Ehd1*$^{-/-}$ mouse testis (right) and epididymis (left). B, E Close up of PAS staining of *Ehd1*$^{+/+}$ and *Ehd1*$^{-/-}$ mouse epididymis. Mature spermatozoa (white arrow) were easily identified in *Ehd1*$^{+/+}$ mouse. In *Ehd1*$^{-/-}$ mouse, macrophages (white arrowheads) were observed instead. C, F, Close up of PAS staining of *Ehd1*$^{+/+}$ and *Ehd1*$^{-/-}$ mouse testis. Elongated spermatids were abundant in *Ehd1*$^{+/+}$ (enlarged region, white arrow) but rarely observed in *Ehd1*$^{-/-}$ mouse (white arrow). Sertoli cell vacuolization (black arrow) and abnormal meiotic figures (enlarged region, black arrowhead) were also detected in the *Ehd1*$^{-/-}$ testis. The

development of germ cells into elongated spermatids is almost absent in the *Ehd1*$^{-/-}$ mouse testis, therefore the number of spermatozoa stored in the epididymis is also reduced.

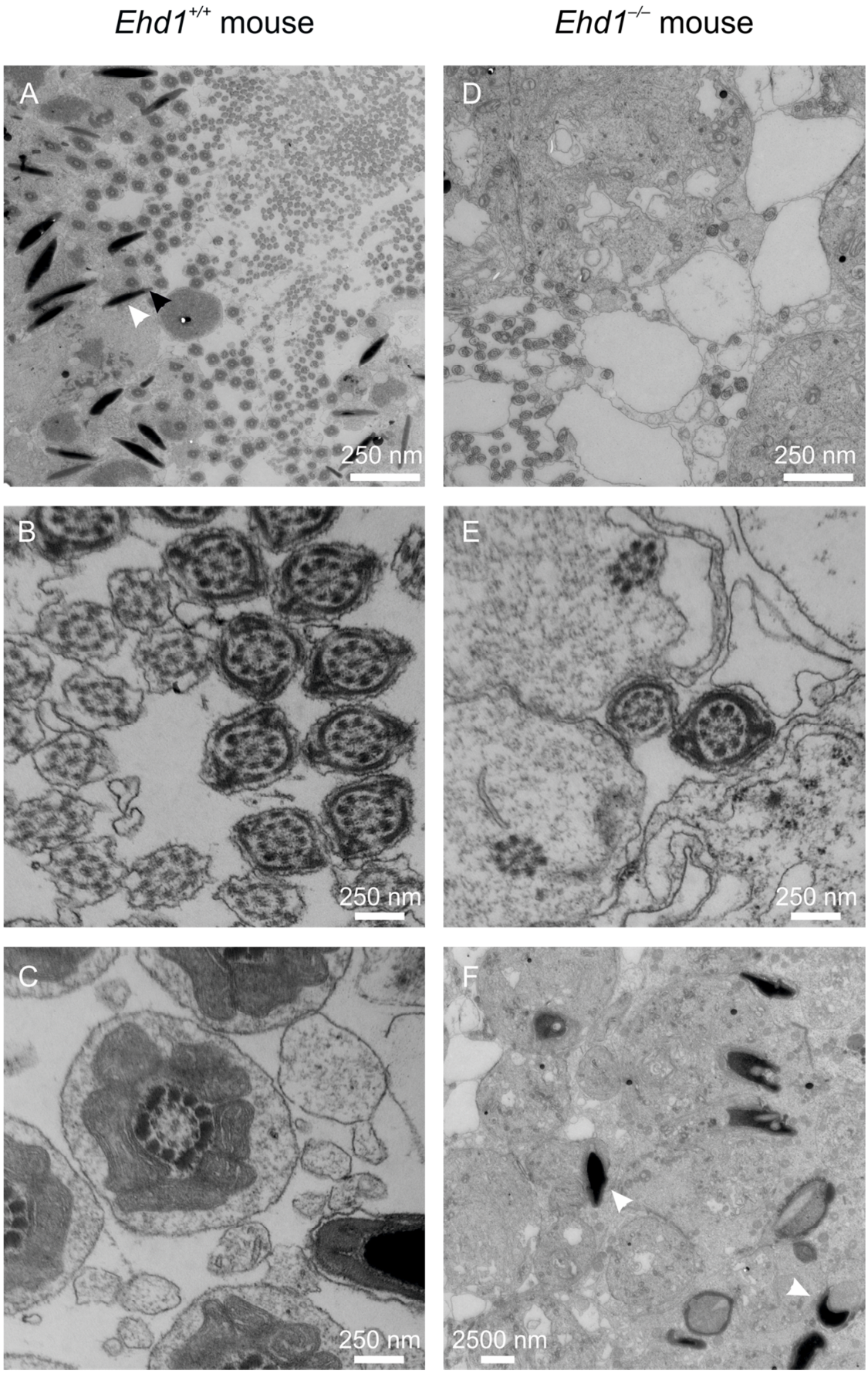

Figure 4.17: Electron micrographs of the seminiferous tubules in the *Ehd1*$^{-/-}$ mouse compared to the control.
A, Electron microscopy of ultra-thin sections of *Ehd1*$^{+/+}$ mouse testis, where elongated spermatids (white arrowhead) with a well defined acrosome (black arrowhead) were observed. B, C, Ultrastructure of the spermatozoa in the *Ehd1*$^{+/+}$ mouse. D, Electron microscopy of ultra-thin sections of *Ehd1*$^{-/-}$ mouse testis. E, Ultrastructure of the spermatozoa in the *Ehd1*$^{-/-}$ mouse. F, Ultrastructure of the seminiferous tubules, where spermatids with abnormal shape (white arrowheads) were observed. The seminiferous tubules in the knockout mouse presented a more disorganized structure than in the wildtype. The elongated spermatids were rarely observed in the *Ehd1*$^{-/-}$ mouse, presenting a rounder shape instead. The spermatozoa in the knockout mice seemed to lack the midpiece structure between the tail and the head, where the mitochondrial sheath is normally localized. Images acquired in collaboration with Prof. Dr. Ralph Witzgall (Institute for Anatomy, University of Regensburg).

4.2.5.3 Effect of *Ehd1* deletion on gene expression in the testis and epididymis

The effect of EHD1 loss on the regulation of *Ehd3* gene expression in the testis and epididymis was addressed by real time PCR (Figure 4.18). Although not enough *Ehd1*$^{-/-}$ mice were measured allowing a comparison between *Ehd1*$^{-/-}$ and *Ehd1*$^{+/+}$ for statistical differences, *Ehd3* transcript displayed a tendency for upregulation in the *Ehd1*$^{-/-}$ testis when compared to the control mice. In the epididymis, no significant difference was observed in *Ehd3* expression between the two groups.

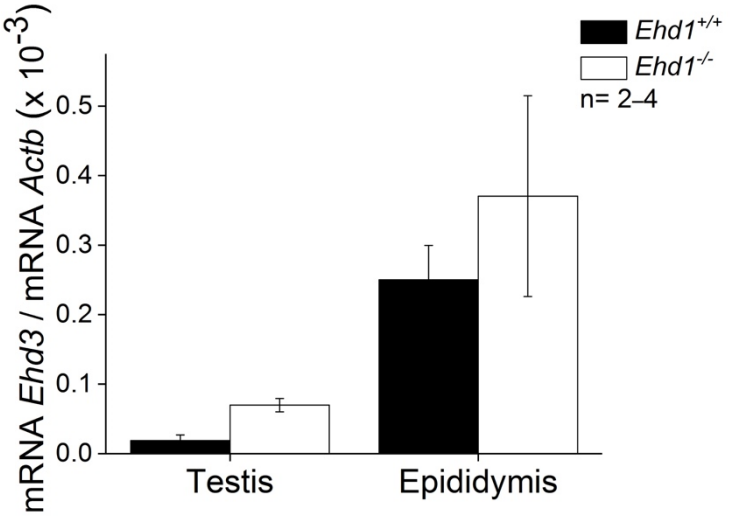

Figure 4.18: *Ehd3* mRNA levels in the *Ehd1*$^{-/-}$ mouse testis and epididymis compared to the control.
Quantification by real time PCR of *Ehd3* mRNA levels in the testis and epididymis of *Ehd1*$^{-/-}$ and *Ehd1*$^{+/+}$ mice normalized to β-actin expression. In the testis, the absence of EHD1 seemed to lead to an upregulation of the *Ehd3* gene. In the epididymis, no significant upregulation of *Ehd3* was observed. More *Ehd1*$^{-/-}$ mice need to be measured in order to compare the two groups for statistical differences. Values are expressed as the mean ± SEM. n= number of mice measured per group for each tissue.

4.2.6 Kidney phenotype of the *Ehd1*$^{-/-}$ mouse

The following set of experiments aimed to shed a light on the possible role of EHD1 in the kidney and to study the effects of *Ehd1* deletion in the mouse. In order to address these issues, immunofluorescence and electron microscopy were used to investigate kidney

histology and low-molecular-weight protein overload experiments were performed to check for the reabsorptive capacity of renal proximal tubules.

4.2.6.1 Histology of the kidney in the *Ehd1*$^{-/-}$ mouse

The electron microscopy of the mouse kidney revealed no obvious differences in proximal tubular histology between the *Ehd1*$^{-/-}$ (Figure 4.19 C, D) and the control mouse (Figure 4.19 A, B). Also, the Coomassie staining of the *Ehd1*$^{-/-}$ mouse urine showed no clear sign of proteinuria when compared to the control (data not shown). These results suggest that the lack of EHD1 in the kidney does not seem to have a severe effect.

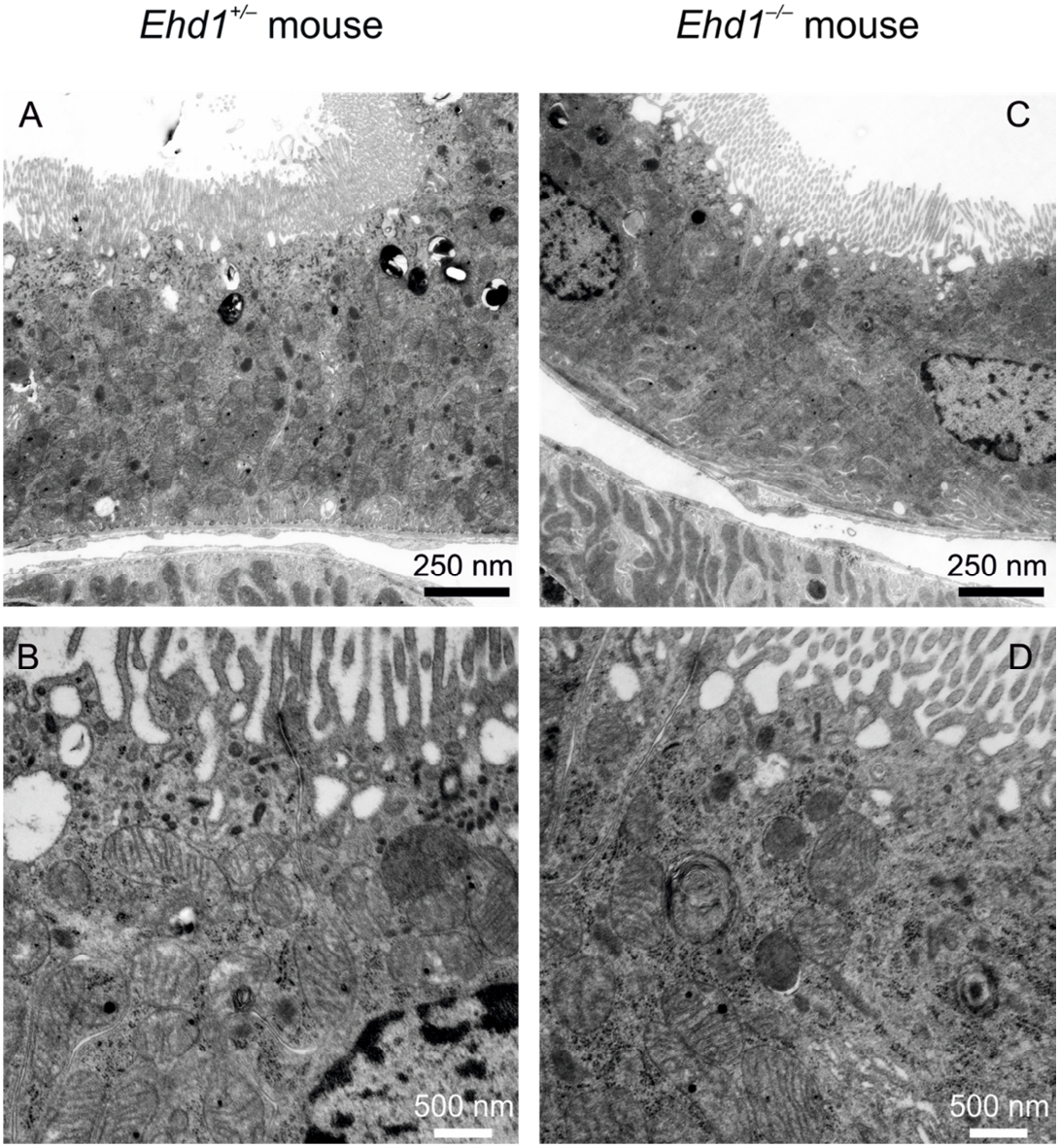

Figure 4.19: Electron micrographs of the renal proximal tubules in the *Ehd1*$^{-/-}$ mouse compared to the control.
A, B, Electron microscopy of the renal proximal tubule of *Ehd1*$^{+/-}$ mouse. C, D, Electron microscopy of the renal proximal tubule of *Ehd1*$^{-/-}$ mouse. The kidney histology of the knockout mouse does not differ from the control mouse. Images acquired in collaboration with Prof. Dr. Ralph Witzgall (Institute for Anatomy, University of Regensburg).

4.2.6.2 Test for low-molecular-weight proteinuria in the *Ehd1*$^{-/-}$ mouse

The EHD1 mutation in the human patients did not cause severe proteinuria, but only a mild form of low-molecular-weight proteinuria. Therefore, immunofluorescence of retinol binding protein (RBP) in the kidney was performed (Figure 4.20). RBP is a low-molecular-weight plasma protein known to carry vitamin A that is normally filtered in the renal glomeruli and completely reabsorbed by the proximal tubules. RBP is also a marker for low-molecular-weight proteinuria, being often excreted in the urine in cases of proximal tubular malfunction. Reabsorbed RBP was observed in the proximal tubular endosomes in *Ehd1*$^{+/+}$ mice (Figure 4.20 left, white arrows), but no signal for RBP was detected in the *Ehd1*$^{-/-}$ mouse kidney (Figure 4.20 right), indicating an impairment of proximal tubular protein uptake.

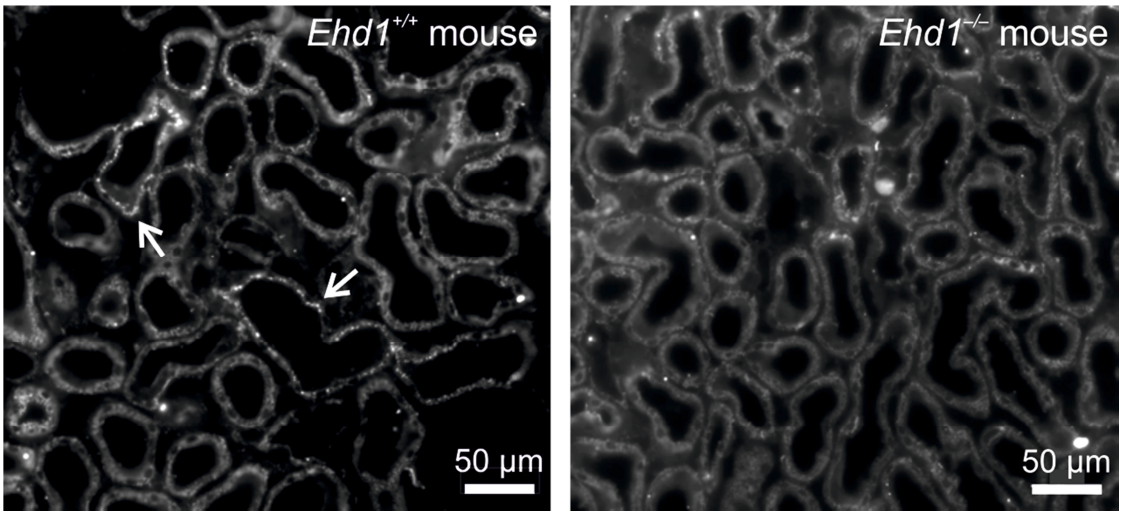

Figure 4.20: Retinol binding protein (RBP) absence in the *Ehd1*$^{-/-}$ mouse kidney.
Immunofluorescence of RBP in cryo sections of *Ehd1*$^{+/+}$ (left) and *Ehd1*$^{-/-}$ (right) mouse kidney. RBP was observed in the proximal tubules of the control mouse (white arrows), but no signal was detected in the knockout mouse.

Since the *Ehd1*$^{-/-}$ mice presented a defective proximal tubular reabsorption of RBP, the mice were then challenged with an overload of another low-molecular-weight protein, in order to quantify protein reabsorption by proximal tubules. To this end, β_2-microglobulin was used. β_2-microglobulin is a component of the MHC class I molecules and another protein marker for low-molecular-weight proteinuria. β_2-microglobulin was conjugated with a fluorescent tag, Alexa Fluor 546 (AF546), which allowed for protein quantification through fluorescence intensity measurements as well as detection in kidney sections. After β_2-microglobulin-AF546 injection through the femoral vein and a period of 30 min incubation, urine and blood were collected, retrograde arterial perfusion and tissue fixation were performed and the kidneys were harvested. The obtained kidney sections revealed a different β_2-microglobulin-AF546 localization in the *Ehd1*$^{-/-}$ mouse when compared to the

control mouse (Figure 4.21). In the *Ehd1*$^{+/+}$ mouse, the β_2-microglobulin-AF546 was localized mainly in the early proximal tubules (Figure 4.21 A, B), while in the knockout the protein presented a broader distribution, extended also to the late proximal tubules (Figure 4.21 C, D). This may suggest that the early segments of the *Ehd1*$^{-/-}$ mouse proximal tubules are not as efficient and/or present a lower reabsorption capacity than the early segments in the *Ehd1*$^{+/+}$ mouse. Therefore, the β_2-microglobulin-AF546 must be further endocytosed by the later segments of the proximal tubules.

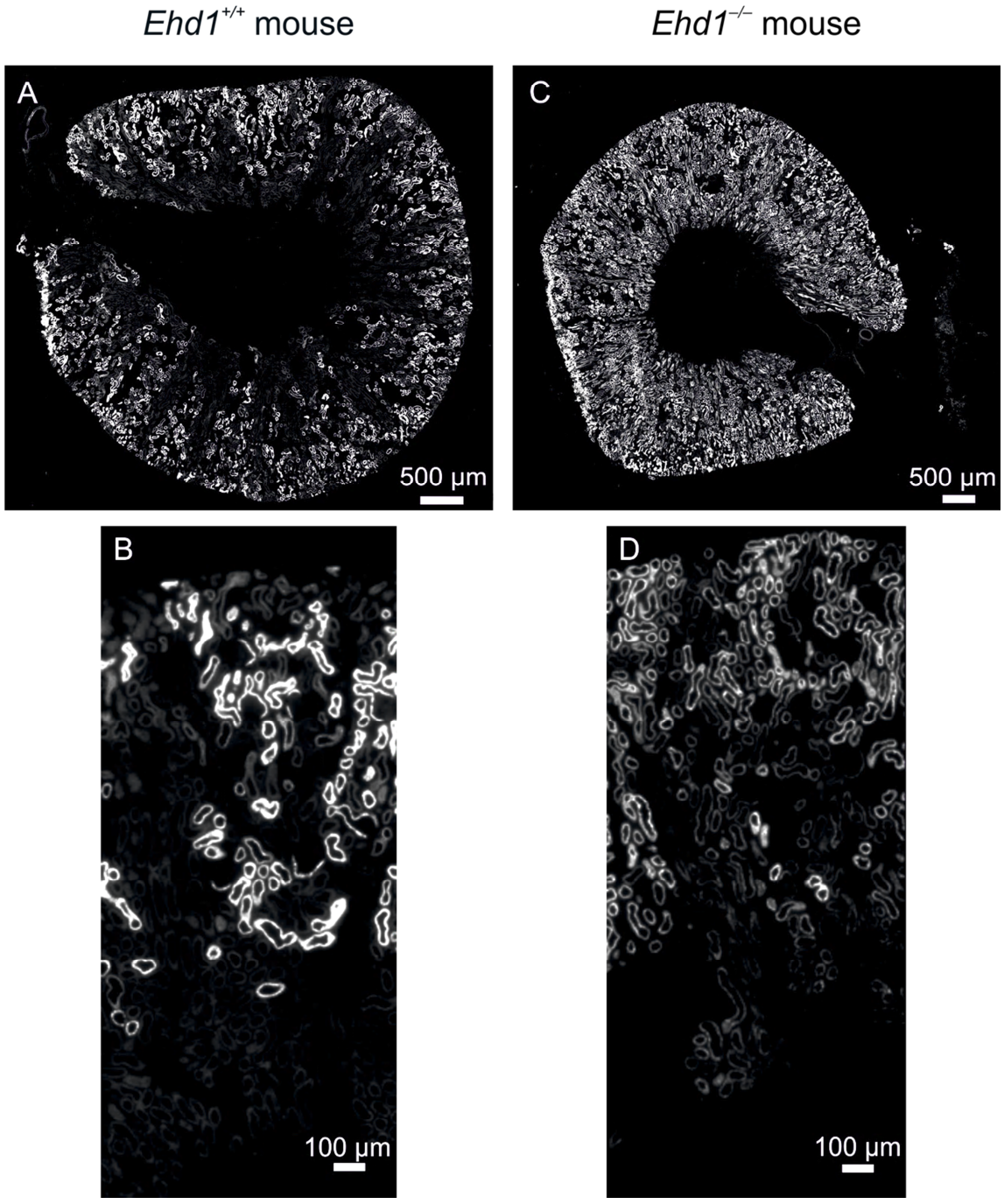

Figure 4.21: β_2-microglobulin proximal tubular localization in the *Ehd1*$^{-/-}$ mouse compared to the control.

A, C, Overview of β_2-microglobulin-Alexa Fluor 546 (AF546) localization in cryo sections of *Ehd1*$^{+/+}$ and *Ehd1*$^{-/-}$ mouse kidneys, respectively. B, D, Close up of β_2-microglobulin-AF546 localization in the *Ehd1*$^{+/+}$ and *Ehd1*$^{-/-}$ mouse kidneys, respectively. The β_2-microglobulin was mainly reabsorbed by the early proximal tubules in the *Ehd1*$^{+/+}$ mouse, while in the *Ehd1*$^{-/-}$ mouse a broader reabsorption by both early and late proximal tubules was observed.

The kidney protein reabsorption efficiency was then examined by quantification of the β_2-microglobulin-AF546 fluorescence in the collected samples, namely kidney homogenate, urine and plasma, and compared between *Ehd1*$^{-/-}$ and control mice (Figure 4.22). The similar values of β_2-microglobulin observed in the plasma indicated that the amount of protein injected was comparable in the two groups (Figure 4.22 A). The β_2-microglobulin values in the kidney (Figure 4.22 B) and in the urine (Figure 4.22 C) after normalization to plasma values demonstrated that the control kidneys were able of a more efficient β_2-microglobulin uptake, while significantly more β_2-microglobulin was excreted in the urine of the *Ehd1*$^{-/-}$ mice.

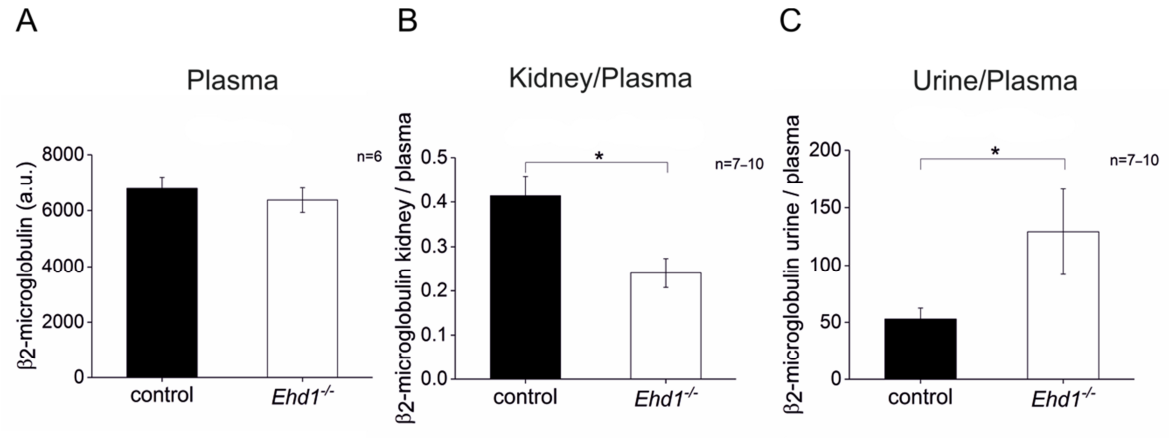

Figure 4.22: Quantification of β_2-microglobulin levels in plasma, kidney and urine of the *Ehd1*$^{-/-}$ mouse compared to the control.
A, Quantification of β_2-microglobulin-Alexa Fluor 546 (AF546) fluorescence in plasma of *Ehd1*$^{-/-}$ and control mice. B, Normalization of β_2-microglobulin-AF546 fluorescence in the kidney to plasma values. C, Normalization of β_2-microglobulin-AF546 fluorescence in the urine to plasma values. The *Ehd1*$^{-/-}$ mice excreted significantly more β_2-microglobulin and had a reduced reabsorption capacity when compared to the control mice. Values are expressed as the mean ± SEM. * $p<0.05$, n= number of mice measured per group for each parameter. Unpaired Student's t-test was used for calculation of significance between groups.

4.2.6.3 β_2-microglobulin internalization by renal proximal tubules in the *Ehd1*$^{-/-}$ mouse

In order to further understand the difference in β_2-microglobulin endocytosis between the *Ehd1*$^{-/-}$ and control mice, the obtained kidney sections were investigated using a confocal microscope (Figure 4.23 A). After comparing the β_2-microglobulin fluorescent signal in the proximal tubules, the endocytosed protein seemed to be localized closer to the plasma membrane in the knockout mice (Figure 4.23 A, lower panel), while exhibiting a higher degree of internalization and endosome processing in the wildtype mouse (Figure 4.23 A,

upper panel). The degree of β_2-microglobulin internalization was then quantified in both groups by measuring the distance between the fluorescence intensity peaks for β_2-microglobulin and megalin (brush border marker) in images from the kidney sections obtained from mice injected with the fluorescent β_2-microglobulin (Figure 4.23 B, C). The β_2-microglobulin and megalin fluorescent signals displayed a much higher degree of colocalization in the *Ehd1*$^{-/-}$ than in the *Ehd1*$^{+/+}$ mouse. The peak for the β_2-microglobulin signal was very often found more distant of the megalin signal, displaying a more cytoplasmic localization in the wildtype mouse when compared to the knockout. This data indicates that in the *Ehd1*$^{-/-}$ the endocytic process in the proximal tubules seems to be somehow impaired by the EHD1 absence.

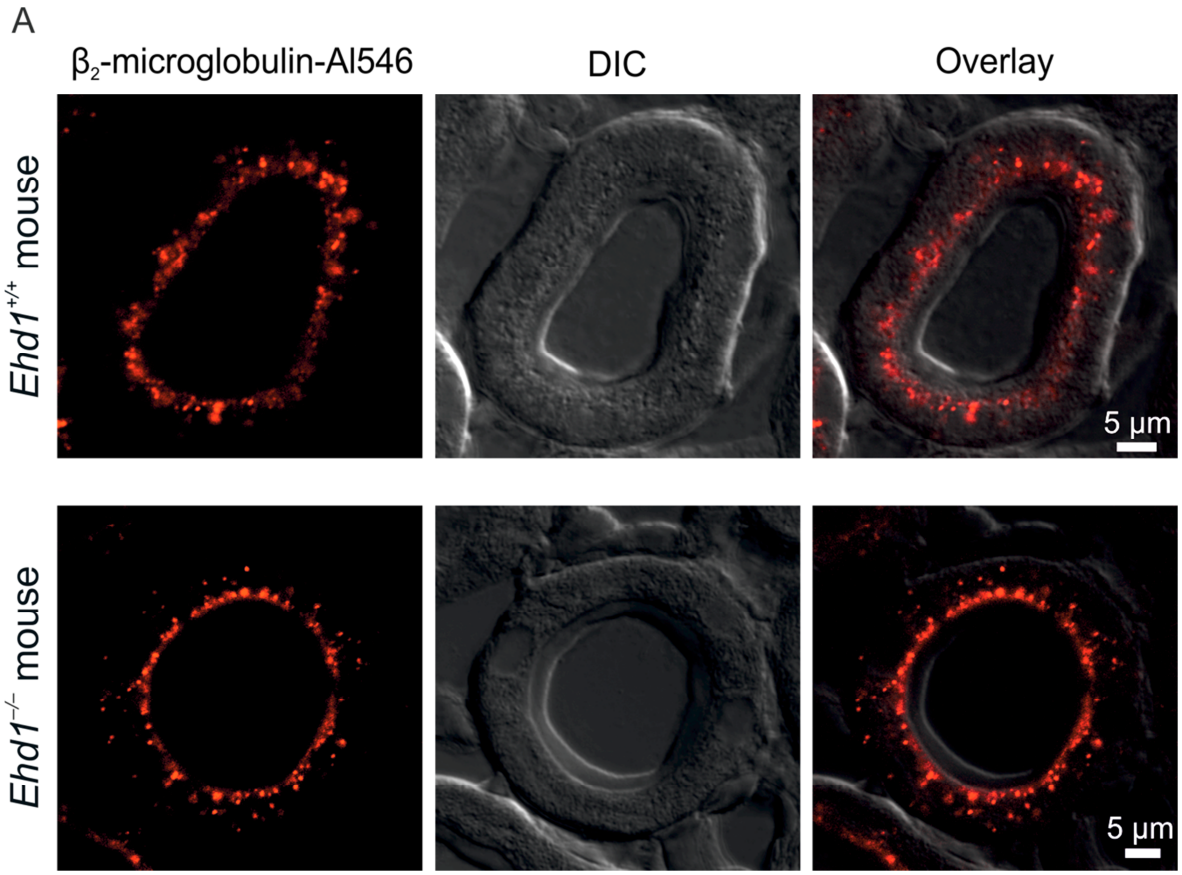

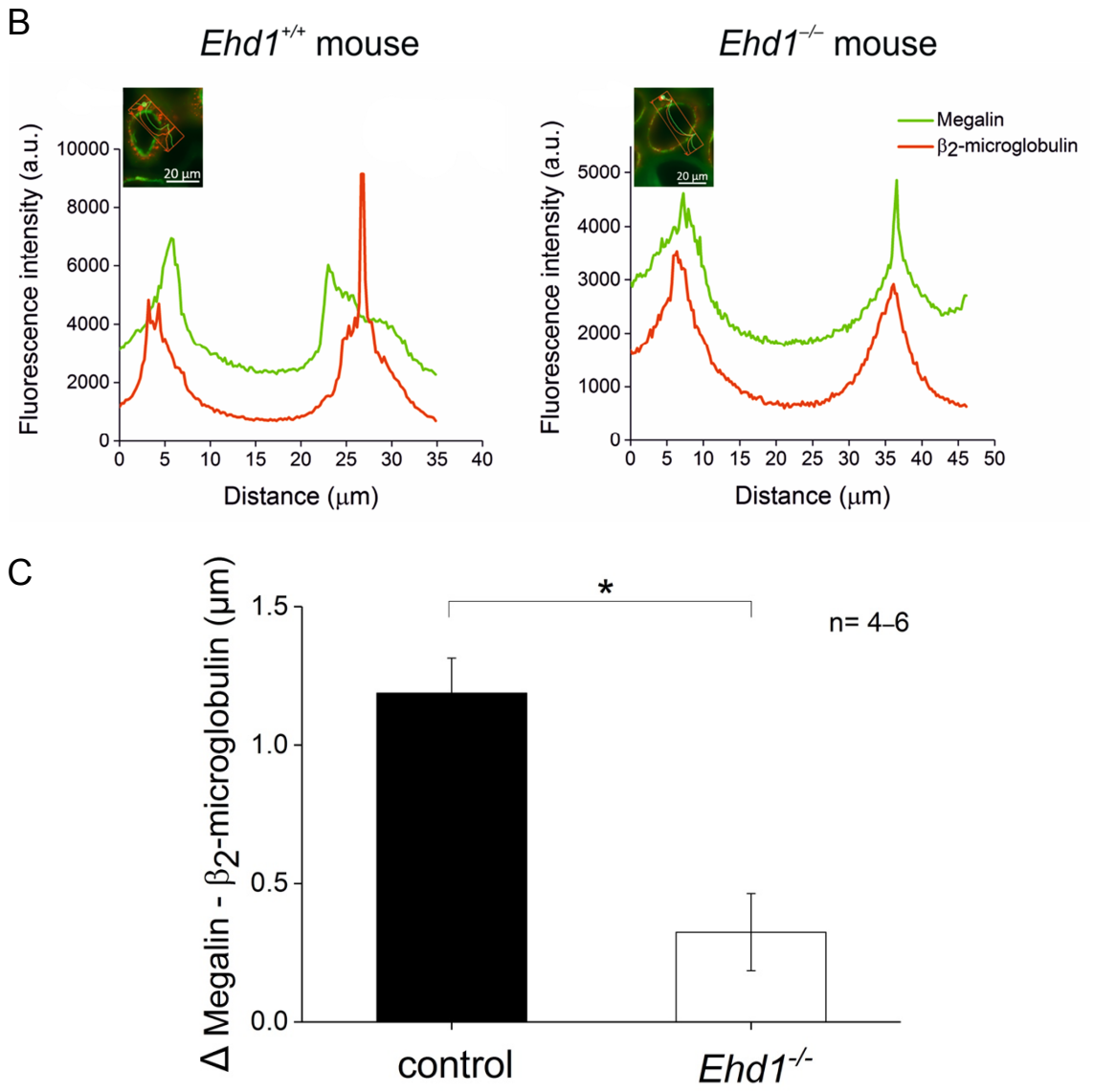

Figure 4.23: β_2-microglobulin endocytosis by proximal tubular cells in the *Ehd1*$^{-/-}$ mouse compared to the control.
A, Confocal microscopy of β_2-microglobulin-Alexa Fluor 546 (AF546) in the proximal tubules of the *Ehd1*$^{-/-}$ and *Ehd1*$^{+/+}$ mice. B, Representative quantification of the fluorescent signals corresponding to megalin and β_2-microglobulin-AF546 in the proximal tubules of *Ehd1*$^{-/-}$ (right) and *Ehd1*$^{+/+}$ (left) mice. C, Distance between megalin and β_2-microglobulin-AF546 localization in the proximal tubules of *Ehd1*$^{-/-}$ and control mice. Control mice seemed to display a more efficient endocytosis and endosome processing than knockout mice, since β_2-microglobulin was more retained in close proximity to the plasma membrane in the knockouts compared to controls. Values are expressed as the mean ± SEM. * $p<0.05$, n= number of mice measured per group. Unpaired Student's t-test was used for calculation of significance between groups.

4.2.6.4 Live-imaging of β_2-microglobulin endocytosis in the *Ehd1*$^{-/-}$ mouse kidney

Finally, in collaboration with Dr. Ina Schießl (Institute for Physiology, University of Regensburg) the reabsorption capacity and endocytosis rate in the proximal tubules of the *Ehd1*$^{-/-}$ mouse were examined overtime using multiphoton microscopy to follow the uptake of β_2-microglobulin-AF546 after injection. To this end, β_2-microglobulin-AF546 (pink) was injected through the jugular vein and the endocytosis by the proximal tubules was followed

during 40 min (Figure 4.24 A). FITC–Dextran 500 kDa (green) was used to label the vasculature in order to control the viability of the mice during the procedure.

For each time point, the fluorescence intensity of β_2-microglobulin-AF546 in the proximal tubules was calculated. A total of 3–6 proximal tubules per mouse were measured and six mice per group (control and *Ehd1*$^{-/-}$) were submitted to the protocol. The proximal tubular reabsorption capacity was compared after 2, 4 and 40 min of β_2-microglobulin injection (Figure 4.24 B). The proximal tubules of control mice exhibited a significantly higher protein uptake in the first four minutes indicating a faster reabsorption dynamics than the ones of *Ehd1*$^{-/-}$ mice. However, at 40 min the β_2-microglobulin reabsorption was no longer statistically different between the groups. The control tubules displayed the maximal tubular fluorescence earlier in time than the tubules of *Ehd1*$^{-/-}$, which often showed increasing fluorescence until the end of the experimental period (Supplements, Figure 11.1).

This data suggests that *Ehd1* deletion leads to a mild impairment of the endocytic process, with the knockout tubules displaying a less efficient reabsorption and maybe impaired intracellular transport of cargo-containing endosomes (Figure 4.23).

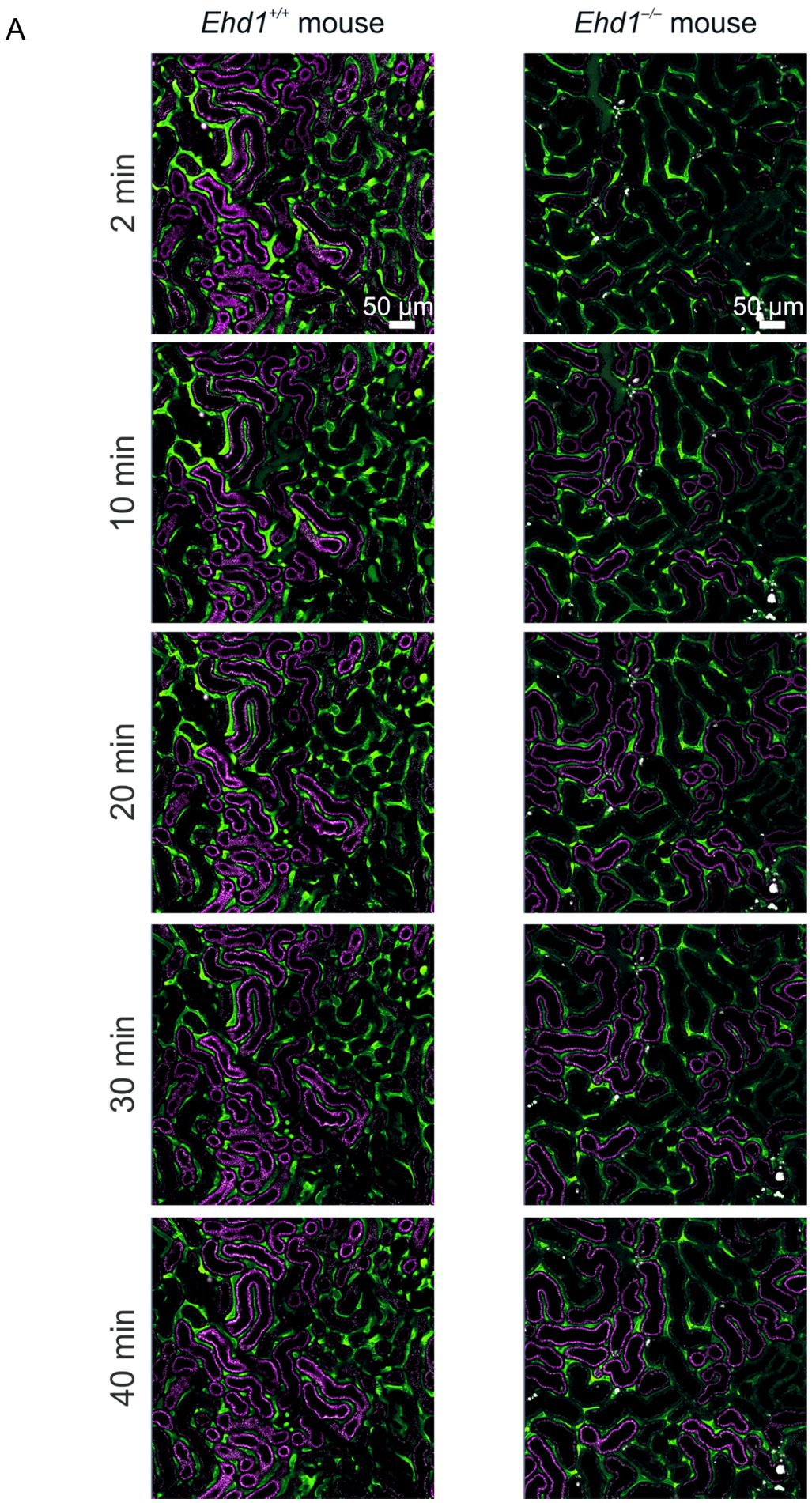
A
Ehd1+/+ mouse
Ehd1−/− mouse
2 min
10 min
20 min
30 min
40 min
50 µm
50 µm

B

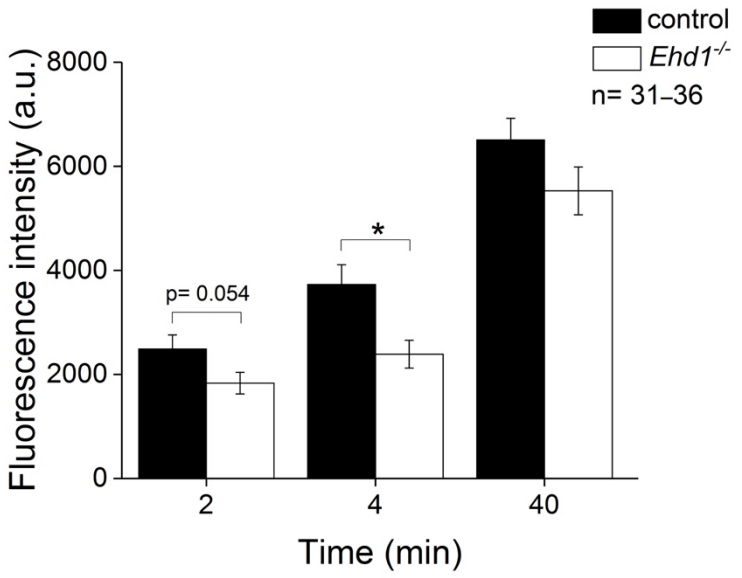

Figure 4.24: Live-imaging of β_2-microglobulin endocytosis by the proximal tubules in the *Ehd1*$^{-/-}$ mouse compared to the control.
A, Representative images of multiphoton microscopy of β_2-microglobulin-Alexa Fluor 546 (AF546; pink) uptake by renal proximal tubules in the *Ehd1*$^{-/-}$ (right) and *Ehd1*$^{+/+}$ (left) mouse for 40 min. FITC–Dextran 500 kDa (green) was used as a vasculature dye. B, β_2-microglobulin-AF546 fluorescence intensity in the proximal tubule after 2, 4 and 40 min of endocytosis in the *Ehd1*$^{-/-}$ and control mice. The proximal tubular endocytosis capacity in the first minutes seemed to be reduced in the knockout. However, the reabsorption capacity is no longer statistically different between *Ehd1*$^{-/-}$ and control mice by the end of the experimental period. Values are expressed as the mean ± SEM. * $p<0.05$, n= number of proximal tubules measured per group, 6 mice were measured per group. Unpaired Student's t-test was used for calculation of significance between groups.

4.2.6.5 Effect of *Ehd1* deletion on gene expression and protein localization in the kidney

Previous reports already studied interactions of EHD1 with several proteins involved in the endocytic pathway, such as MICAL-L1 [52], Syndapin-2 [65], Rabenosyn-5 [34], SNAP29 [63], EHD3 [66] or EHD4 [67], and as previously showed, also with megalin (Figure 4.6). Therefore, the next set of experiments aimed to study the effect of EHD1 loss on the regulation of gene expression and protein localization in some of these potential partners, as well as for other proteins essential for endocytosis in the kidney.

The mRNA levels of *Lrp2*, *Cubn* and *Amn*, which encode for the main receptors in the proximal tubules, megalin, cubilin and amnionless, respectively, were examined using real time PCR (Figure 4.25 A). The *Ehd1* deletion seemed not to have any effect on the regulation of these genes expression, since the mRNA levels detected in both *Ehd1*$^{-/-}$ and *Ehd1*$^{+/+}$ mouse kidneys were similar. The mRNA levels of other known EHD1 partners were also found unaltered in the *Ehd1*$^{-/-}$ kidney (Figure 4.25 B).

Finally, to investigate if EHD1 absence was compensated by another EHD homologue the mRNA levels were quantified (Figure 4.25 C). The *Ehd2–4* mRNA expression was similar

in both *Ehd1*$^{+/+}$ and *Ehd1*$^{-/-}$ mice, with exception of *Ehd4* that presented a reduced expression in comparison to the *Ehd1*$^{+/+}$ kidney, however more measurements need to be performed in order to conclude about the significance of this observation. This data suggests that the absence of EHD1 in the kidney is not compensated by the upregulation of the other *Ehd* transcripts.

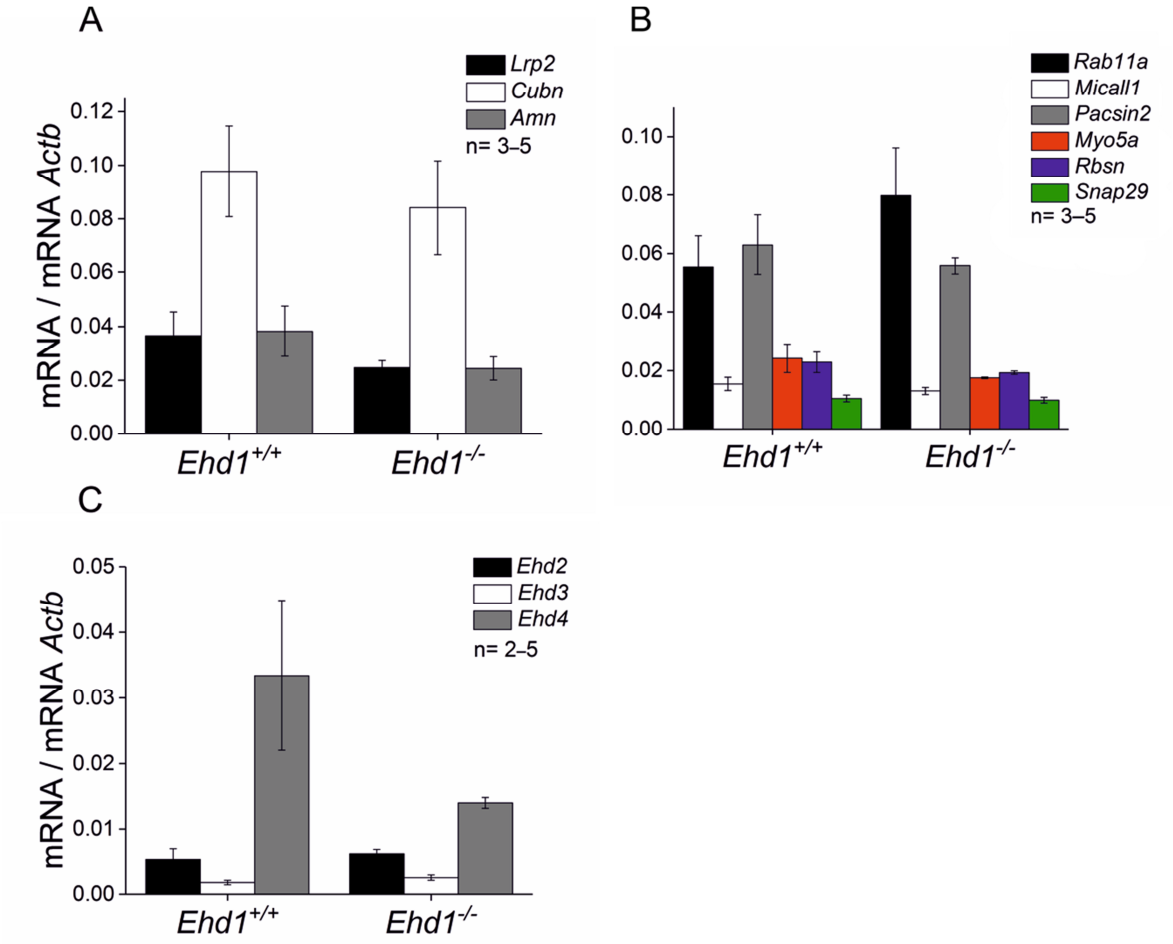

Figure 4.25: mRNA levels of EHD1 potential partners in the *Ehd1*$^{-/-}$ mouse kidney compared to the control.
A, Quantification by real time PCR of mRNA levels of *Lrp2* (megalin), *Cubn* (cubilin) and *Amn* (amnionless) in the kidney of *Ehd1*$^{-/-}$ mouse compared to wildtype. B, Real time PCR quantification of mRNA levels of *Rab11a*, *Micall1*, *Pacsin2* (Syndapin-2), *Myo5a* (Myosin-Va), *Rbsn* (Rabenosyn-5) and *Snap29* in the kidney of *Ehd1*$^{-/-}$ mice compared to *Ehd1*$^{+/+}$. C, Quantification by real time PCR of mRNA levels of *Ehd2*, *Ehd3* and *Ehd4* in the kidney. In the kidney, the absence of EHD1 does not seem to have an effect on the gene expression of interaction partners or in the major receptors responsible for endocytosis. EHD1 loss does not appear to be compensated by upregulation of other EHD homologues. Values are expressed as the mean ± SEM. n= number of mice measured per gene. Unpaired Student's t-test was used for calculation of significance between groups.

Afterwards, the effect of the EHD1 loss on the localization of megalin and cubilin was investigated using immunofluorescence (Figure 4.26). Although an interaction between EHD1 and megalin was previously detected in mouse kidney (Figure 4.6), the protein

localization observed in the knockout kidney was similar to the one in the wildtype for both megalin and cubilin.

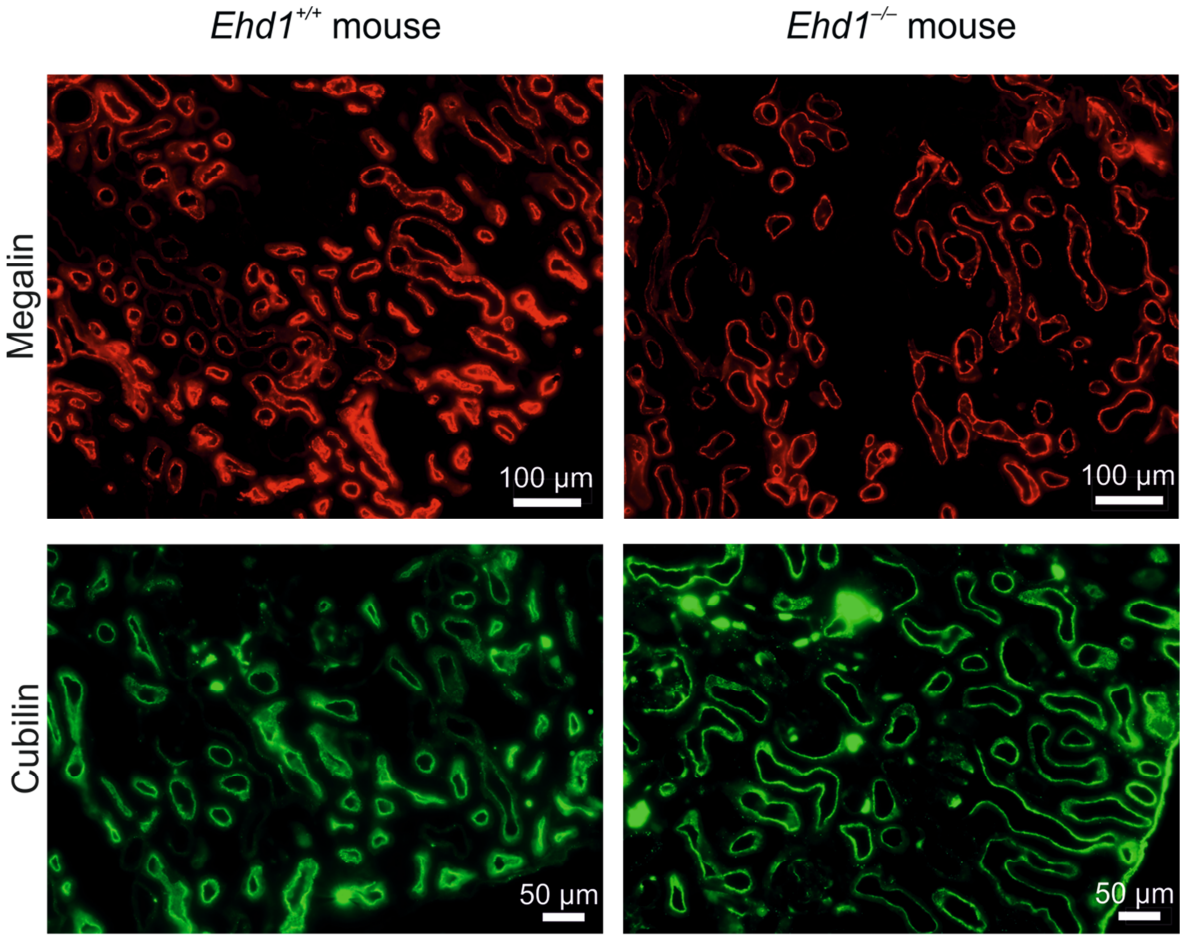

Figure 4.26: Localization of megalin and cubilin in the *Ehd1*$^{-/-}$ mouse kidney compared to the control.
In control and *Ehd1*$^{-/-}$ kidneys megalin and cubilin localized to the brush border of proximal tubules. This suggests that the loss of the interaction partner EHD1 does not affect their localization or to such a small extent that it could not be detected by the method used.

4.3 LLC-PK1 inducible cell lines

To analyze the effect of the R398W mutation found in the human patients, inducible cell lines derived from pig renal proximal tubular cells, known as LLC-PK1, were investigated. These cells stably expressed either the wildtype form of human EHD1 (WT-hEHD1) or the mutant variant (R398W-hEHD1) under the control of a Tet-On-System. The following experiments examined the effect of the newly discovered mutation on EHD1 cellular localization, protein stability and function.

4.3.1 WT- and R398W-EHD1 cellular localization

The EHD1 immunofluorescence in the LLC-PK1 inducible cells revealed a different subcellular distribution of the wildtype EHD1 when compared to the mutant (Figure 4.27).

The WT-hEHD1 displayed a more cytoplasmic localization, around vesicle-like structures (Figure 4.27 A left, B), while the R398W-hEHD1 was localized mainly at the cell borders and in small tubular structures (Figure 4.27 A right, C). This data suggests that the R398W mutation has an influence on protein trafficking and subcellular localization.

A

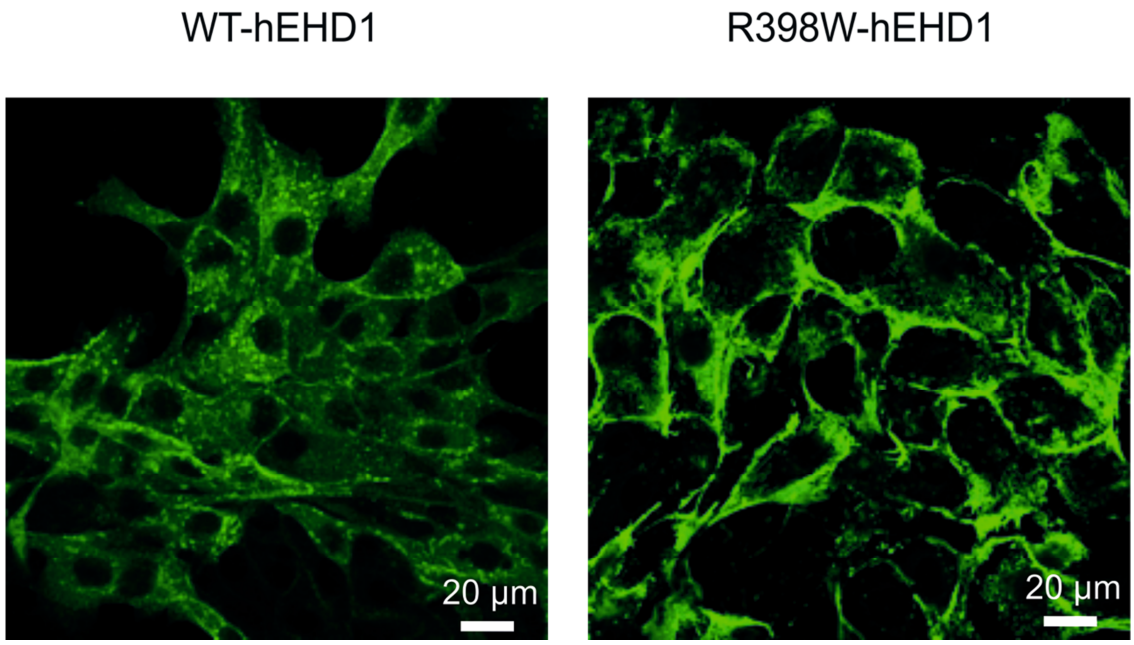

B

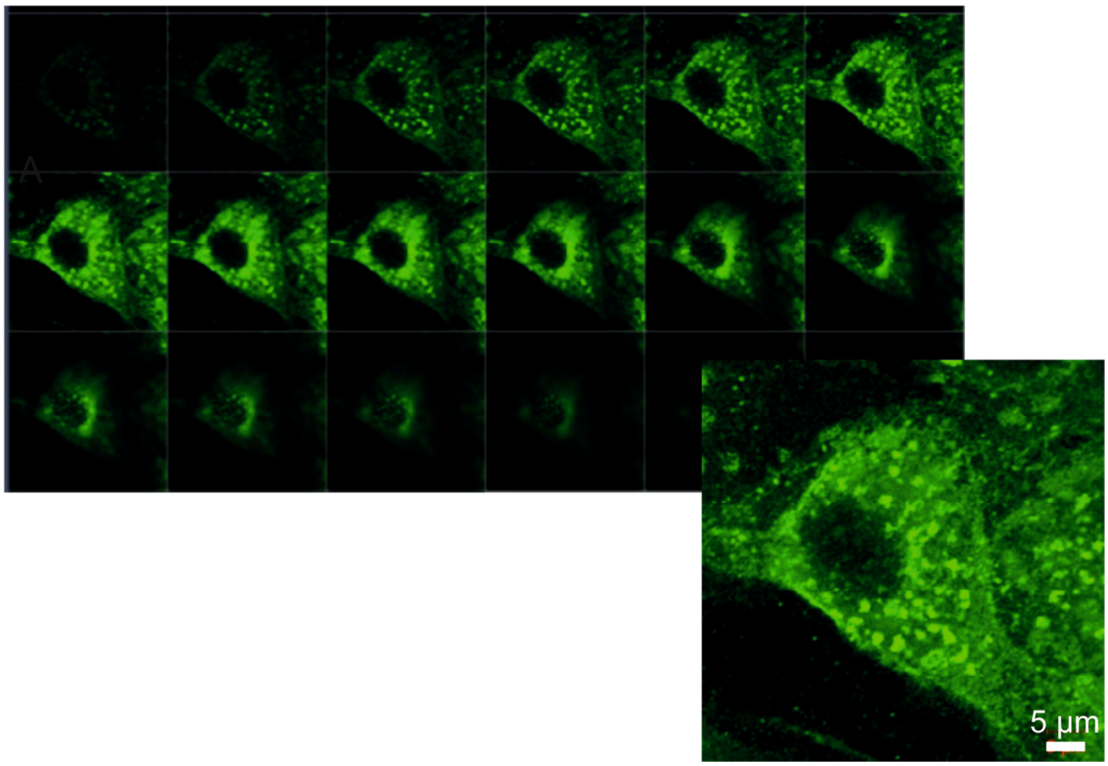

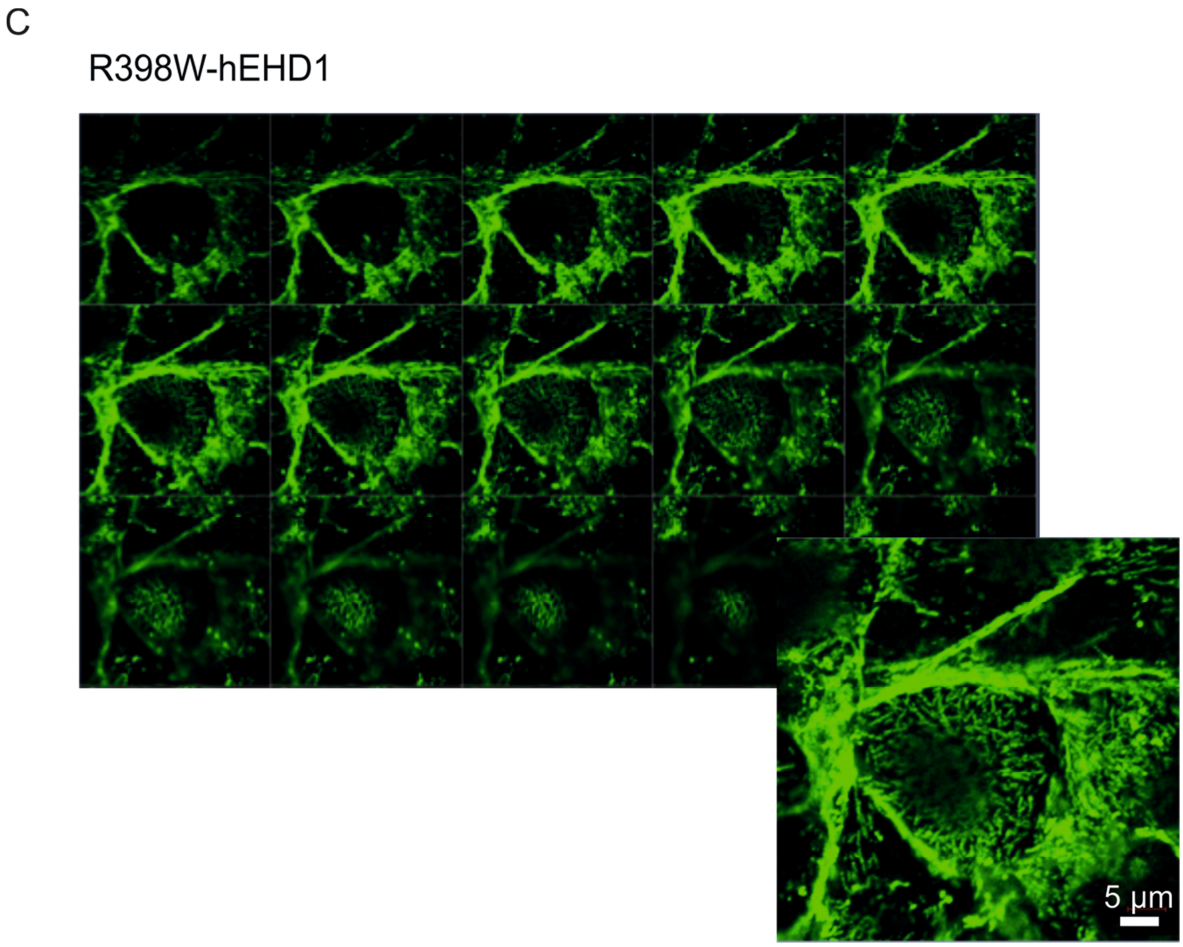

Figure: 4.27: Different subcellular localization of WT-hEHD1 and R398W-hEHD1.
A, Confocal microscopy of WT- (left) and R398W-hEHD1 (right) immunofluorescence in LLC-PK1 inducible cells. B, Z-stack of WT-hEHD1 in LLC-PK1 inducible cells, with close up of WT-hEHD1 subcellular localization. C, Z-stack of R398W-hEHD1 in LLC-PK1 inducible cells, with close up of R398W-hEHD1 subcellular localization. The WT-EHD1 was localized around vesicle-like structures, while the R398W-EHD1 displayed a more cell border localization and in tubulus-like structures.

4.3.2 WT- and R398W-EHD1 protein stability

The effect of the R398W mutation on protein stability was addressed by quantifying the amount of EHD1 protein after ceasing the induction with tetracycline (Figure 4.28). Western blot and quantification of the bands with normalization to actin expression showed that the WT-EHD1 was expressed at high levels for 5 days, while the mutant cells displayed already a great reduction in protein abundance after 2 days, indicating that the mutation reduced the EHD1 stability, probably by accelerating its degradation.

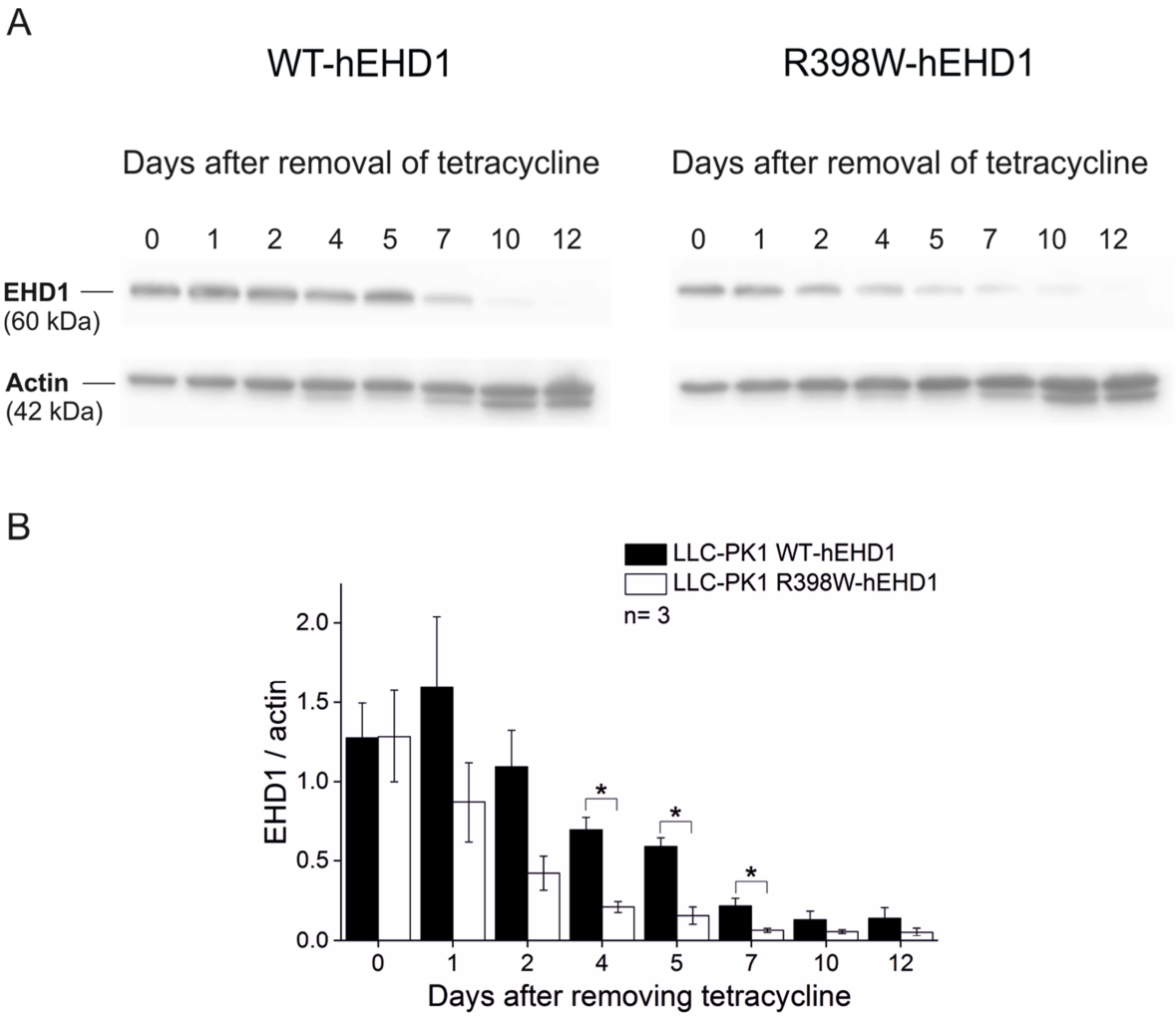

Figure 4.28: Comparison of WT-hEHD1 and R398W-hEHD1 protein stability.
A, Western blot of EHD1 and actin from protein samples isolated from LLC-PK1 WT-hEHD1 (left) and LLC-PK1 R398W-hEHD1 (right) cells during several days after removal of tetracycline induction. B, Quantification of the Western blot with normalization of EHD1 values to actin. The WT-hEHD1 seemed to be more stable than the mutant form, suggesting accelerated degradation of the mutant protein. Values are expressed as the mean ± SEM. * $p<0.05$, n= number of protein samples measured per group for each day. Unpaired Student's t-test was used for calculation of significance between groups.

4.3.3 WT- and R398W-EHD1 protein function

In order to test if the mutation was somehow altering the EHD1 function in endocytosis, the transepithelial transport of a fluorescently labelled bovine serum albumin (BSA) in induced polarized LLC-PK1 cells was measured (Figure 4.29). The amount of FITC-BSA transported from the apical to the basolateral side was similar for both wildtype and mutant cells, suggesting that the mutation does not severely affect endocytosis in LLC-PK1 cells.

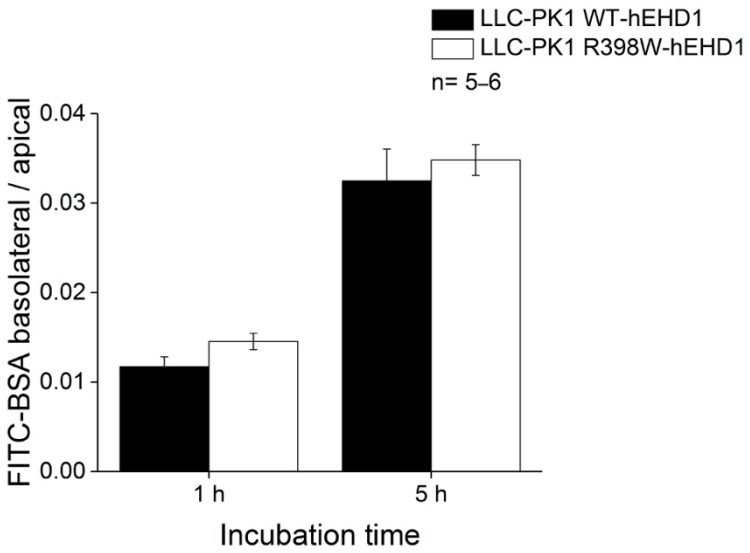

Figure 4.29: Bovine serum albumin transepithelial transport by polarized LLC-PK1 inducible cells.
Quantification of the FITC-Bovine serum albumin (BSA) fluorescence on the basolateral side relative to the fluorescence present in the apical side over time. No difference in transepithelial BSA transport capacity was observed between LLC-PK1 WT-hEHD1 and R398W-hEHD1 cells. Values are expressed as the mean ± SEM. n= number of samples measured per group for each incubation time. Unpaired Student's t-test was used for calculation of significance between groups.

Since a difference in β_2-microglobulin uptake between control and *Ehd1*$^{-/-}$ mice was previously observed, the β_2-microglobulin-AF546 transepithelial transport was also measured in wildtype and mutant cells. To this end, the induced and polarized LLC-PK1 cells were incubated for 5 h with β_2-microglobulin-AF546 on the apical side, then the β_2-microglobulin fluorescence on the basolateral side was measured. However, no β_2-microglobulin-AF546 was detected on the basolateral side on both wildtype and mutant cells. It is possible that the fluorescent tag was degraded during passage of the lysosomal pathway and/or the rate of endocytosis in the cells is below the detection limit. Therefore, the proteins were isolated from the cells in filters and β_2-microglobulin was quantified by Western blot in order to investigate cellular protein uptake (Figure 4.30). The Western blot revealed that indeed these cells were able to take up β_2-microglobulin, however the amount of β_2-microglobulin endocytosed by both cell lines was similar, revealing no difference in uptake efficiency between wildtype and mutant cells.

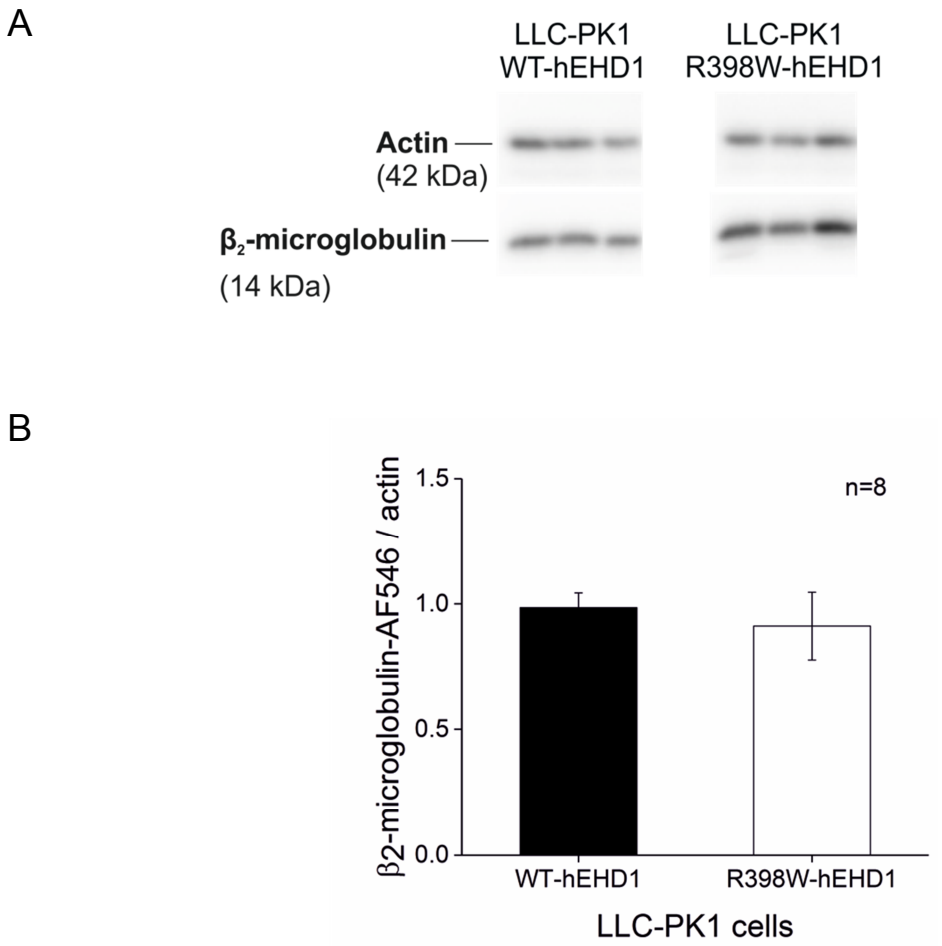

Figure 4.30: β_2-microglobulin-Alexa Fluor 546 uptake by polarized LLC-PK1 inducible cells. A, Western blot of β_2-microglobulin from protein samples isolated from LLC-PK1 WT- (left) and R398W-hEHD1 (right) after 5 h incubation with β_2-microglobulin-Alexa Fluor 546 (AF546). β_2-microglobulin was detected with an antibody against β_2-microglobulin. B, Quantification of the Western blot with normalization of the β_2-microglobulin values to actin. No difference in uptake efficiency was observed between wildtype and mutant cells. Values are expressed as the mean ± SEM. n= number of protein samples measured per group. Unpaired Student's t-test was used for calculation of significance between groups.

4.3.4 Gene expression in WT- and R398W-EHD1 LLC-PK1 cells

The gene expression of some of the EHD1 known and potential partners was also examined by real time PCR and compared in non-stimulated and tetracycline stimulated wildtype and mutant cells (Figure 4.31). The mRNA levels of *EHD3, RAB8A, RAB11A, MICALL1* and *TFRC* were similar in non-stimulated cells and cells overexpressing the WT-hEHD1 (Figure 4.31 left) and R398W-hEHD1 (Figure 4.31 right). This suggests that the overexpression of EHD1 displayed no major effect on levels of the studied mRNAs. Furthermore, both wildtype and mutant cells presented a mRNA expression within the same range of values. No significant up or downregulation of the transcripts was observed, suggesting that EHD1 expression has no effect on the transcriptional regulation of its partners.

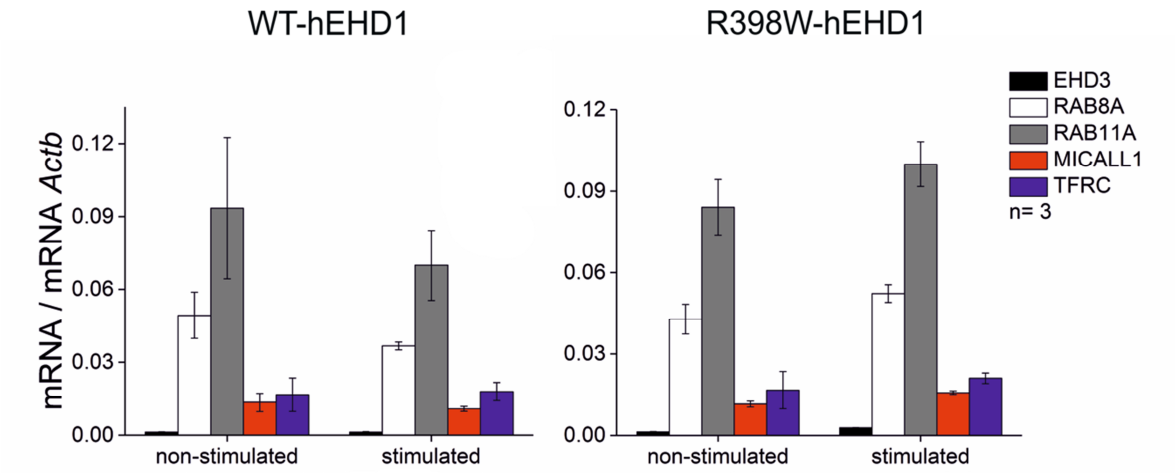

Figure 4.31: mRNA levels of EHD1 partners in the LLC-PK1 inducible cells.
Real time PCR was used to quantify *EHD3, RAB8A, RAB11A, MIICALL1* and *TFRC* mRNA levels in LLC-PK1 WT- (left) and R398W-hEHD1 (right) cells stimulated vs non-stimulated with tetracycline. There was no significant difference in mRNA levels between stimulated and non-stimulated cells for both wildtype and mutant cells. This suggests that the overexpression of both proteins has no effect on the regulation of mRNA levels of EHD1 potential partners. Values are expressed as the mean ± SEM. n= number of samples measured per mRNA for each condition. Unpaired Student's t-test was used for calculation of significance between groups.

5. Discussion

The idea for this dissertation started in Israel, where Dr. Naomi Issler examined 6 patients, 7–15 years of age, presenting tubular proteinuria (1-2 g per day) and hearing loss at a high frequency range. By linkage analysis and DNA sequencing, Prof. Dr. Robert Kleta (University College London) identified in all patients a homozygous missense mutation — R398W — in the EHD1 protein. It has been proposed already some 20 years ago that the four human EHD proteins (EHD1–4) have a function in the endocytic pathway and are involved in receptor recycling. However, the specific roles of the EHD proteins have not yet been elucidated. This thesis aimed at investigating the physiological function of EHD1 — especially in renal proximal tubules and inner ear — and its role in human disease using a knockout mouse and cell lines expressing wildtype and mutant EHD1 as models.

5.1 *Ehd1* deletion and mouse lethality

The *Ehd1*$^{-/-}$ mouse used in this project was generated by deletion of the second exon in the *Ehd1* gene. This strategy is different from the ones used in previously published mouse lines, where EHD1 inactivation was achieved either by deletion of the first exon [77] or deletion of part of the third exon and exons 4 and 5 [54]. The *Ehd1* deletion in our mice, showed an enhanced prenatal lethality, with only 10% *Ehd1*$^{-/-}$ mice being born instead of the expected 25% (Table 4.1). This was also observed by Rainey and co-workers [77], who obtained only 8% of knockout progeny, but not by Rapaport [54], who observed no overt phenotype in their *Ehd1* knockout mice. Moreover, we witnessed a further decrease in the percentage of viable knockouts overtime until we obtained no more knockout mice. This wide spectrum of phenotypes could be explained by a very recent report from Bhattacharyya and co-workers [79]. They observed that the severity of the phenotype resulting from the *Ehd1* deletion is dependent on the mouse strain. In a mostly C57BL6 background, the knockout led to mid-gestational embryonic lethality with major developmental defects, but in a C57BL6;129S mixed background the phenotype was less severe and lethality was reduced. Our mice had a C57BL6;129S mixed background. With increased backcross to the C57BL6 background, lethality of knockout mice increased to almost 100%. Unlike Rainey and co-workers [77], we did not observe a significant reduction in *Ehd1*$^{-/-}$ mice body weight. Interestingly, the mice used in the study from Rapaport and co-workers [54] had a 129/SvEv and were never crossed with C57BL6 mice, which probably explains the absence of a severe phenotype. Therefore, we started with a backcross into the 129S background. Already after one generation of backcross, viable knockouts were produced supporting the hypothesis of Bhattacharyya et al [79] (data not shown).

5.2 *Ehd1*$^{-/-}$ mouse and eye abnormalities

The study of the eye phenotype in our *Ehd1*$^{-/-}$ mouse revealed that around $^{1}/_{3}$ of the adult knockouts presented eye problems while no abnormalities were observed in control animals (Figure 4.10). These ocular abnormalities included anophthalmia, microphthalmia and cataracts. A similar eye phenotype was also reported by Arya and co-workers [11]. They observed ocular abnormalities in 56% of the knockouts and by performing a conditional *Ehd1* deletion in the lens, they detected developmental defects that included thin epithelial layers, small lenses and absence of corneal endothelium. Reduced lens epithelial proliferation and survival, together with corneal endothelial differentiation defects were also observed. These findings suggest a role for EHD1 in early lens and eye development.

5.3 *Ehd1*$^{-/-}$ mouse and hearing deficiency

Little is known about the function of EHD proteins in the inner ear. To our knowledge, only one study addressing the role of EHD4 in the inner ear was performed [10]. Sengupta and co-workers reported that EHD4 is localized in the cochlear hair cells and colocalizes with Cadherin 23 (CDH23; a transmembrane protein essential for auditory signal transduction). The interaction was mediated through the EH domain of EHD1 in a calcium-sensitive manner. However, *Ehd4*$^{-/-}$ mice displayed a normal hearing sensitivity at frequencies between 2–10 kHz. In our studies, the auditory brainstem response measurements showed a tendency for reduced hearing ability of the *Ehd1*$^{-/-}$ mouse at high frequencies (Figure 4.13), although the cochlea histology appeared to be normal (Figure 4.11). At lower frequencies, more similar to the ones tested in the *Ehd4*$^{-/-}$ mice, the wildtype and the *Ehd1*$^{-/-}$ mouse presented similar audiograms (Figure 4.13). Due to unspecific antibody binding to cochlear structures we were unable to determine the protein localization (Figure 4.12); the *Ehd1* mRNA presence in the cochlea, however, was verified (Figure 4.1). Since the hearing deficiency in humans and mice is restricted to the high frequency range, it is possible that EHD1 plays a role in receptor recycling in the hair cells of the lower part of the cochlea, which perceive the high frequency sounds. It is also possible that the inner ear phenotype is only mild due to functional compensation by other EHDs, as suggested by Sengupta and co-workers [10]. Sengupta and co-workers [10] observed an upregulation of the EHD1 protein expression in the cochlea of *Ehd4*$^{-/-}$ mice. In the *Ehd1*$^{-/-}$ mouse cochlea we observed no significant upregulation of the *Ehd3* transcript (Figure 4.14), but expression of *Ehd2* and *Ehd4* still has to be investigated. In order to understand the role of EHD1 in the auditory pathway, it would be interesting to investigate the possibility of an interaction between EHD1 and CDH23 and to test if EHD1 is involved in CDH23 recycling.

5.4 *Ehd1*$^{-/-}$ mouse and male infertility

The testis was the tissue among the ones tested that displayed the highest *Ehd1* mRNA levels (Figure 4.1). EHD1 was detected in the seminiferous tubules of adult mice, mostly in cells at a late stage of spermatogenesis, namely elongated spermatids (Figure 4.3). Furthermore, our X-Gal staining in the epididymis showed that EHD1 is localized in the mature spermatozoa (Figure 4.2).

Spermatogenesis is a complex process where spermatogonia develop into mature spermatozoa able to fertilize the ovum. Spermatogenesis occurs in the seminiferous tubules in the testes. Here, the Sertoli cells nurse the developing germ cells, remaining attached throughout this process, until the elongated spermatids develop into polarized spermatozoa and are released into the lumen of the tubules, in a process called spermiation. The mature spermatozoa are later stored in the epididymis.

Male *Ehd1*$^{-/-}$ mice presented signs of infertility when we tried for several times, without success, the breeding with *Ehd1*$^{+/+}$ females (Table 4.1). The *Ehd1*$^{-/-}$ mice exhibited smaller testes (Figure 4.15) and the few spermatozoa isolated from the epididymis were not motile. The extremely reduced number of spermatozoa in the epididymis was also confirmed by PAS staining (Figure 4.16 E). Moreover, several anomalies were detected in the testis histology of *Ehd1*$^{-/-}$. The seminiferous tubules had a reduced number of elongated spermatids (Figure 4.16 F, white arrow), displayed Sertoli cell vacuolization (Figure 4.16 F, black arrow) and abnormal meiotic figures (Figure 4.16 F, enlarged region, black arrowhead). Several seminiferous tubules also presented a very disorganized structure (Figure 4.16 F, tubule on the right side). In the epididymis, spermatozoa were almost absent and macrophages were observed instead (Figure 4.16 E, white arrowheads), suggesting the digestion of the malformed spermatozoa. The electron micrographs of the seminiferous tubules revealed abnormal spermatids morphology, displaying a rounder or sickle-like shape (Figure 4.17 F) instead of the normal elongated shape and practically no spermatids were localized near the tubules lumen and ready for spermiation (Figure 4.17 D). Also, the spermatids acrosome, a cap-like structure derived from the Golgi apparatus that contains digestive enzymes, was almost undetectable when compared with the wildtype where it was well defined (Figure 4.17 A, black arrowhead).

Rainey and co-workers [77] previously reported a similar testicular phenotype that led to infertility of the *Ehd1*$^{-/-}$ mice. They also observed that the knockout mice were unable to generate offspring and exhibited a reduced size of the testes. After a thorough histological study, those authors concluded that the *Ehd1*$^{-/-}$ mice exhibited an impaired acrosomal development in round spermatids and that normal elongated spermatids were absent. Furthermore, Rainey and co-workers observed an abnormal phagocytosis of elongated

spermatids by Sertoli cells in *Ehd1*$^{-/-}$ mice. They were also unable to detect mature spermatozoa in the epididymis of the knockouts.

Taken together, Rainey's and our work are pointing to an essential role of EHD1 in acrosome development and in spermatozoa maturation. Furthermore, endocytosis and recycling of integral membrane proteins was already shown to be an important regulator of spermatogenesis [128]. Since EHD proteins are known to regulate endocytic recycling in other systems, a role for EHD1 in endocytic recycling during spermatogenesis can be suggested.

Very interestingly, we also observed that the spermatozoon midpiece structure, where the mitochondrial sheath is localized, was absent in the *Ehd1*$^{-/-}$ mouse. The mitochondria are essential for the production of ATP, that will be used by the dynein motor proteins for flagellar movement. The absence of those mitochondria might explain the asthenozoospermia of the few spermatozoa found in the epididymis.

Very recently, studies in cell lines proposed a new role of EHD1 as a regulator for mitochondrial fission [75]. The fusion and fission process is essential to control mitochondrial size and shape, the number of mitochondria for inheritance in dividing cells, and many mitochondrial functions such as respiration and cell survival [129]. EHD1 and Rabankyrin-5 appeared to interact with the retromer complex and to influence mitochondrial dynamics likely by inducing VPS35-mediated removal of inactive Drp1, a dynamin-related GTPase, from mitochondrial membranes. Drp1 was found to be strongly expressed in the round and elongating spermatids in the seminiferous tubules of the rat [130], and it was reported in *Drosophila* that its absence led to abnormal clustering of mitochondria in mature primary spermatocytes and aberrant unfurling of the mitochondrial derivatives in early Drp1 spermatids undergoing axonemal elongation [131]. Our observations in the mouse together with the previously reported data suggest that EHD1 may have a role in the mitochondrial sheath development with its absence leading to dysregulation of the fusion and fission mitochondrial process. On the other hand, the importance of EHD1 for these processes is probably restricted to some tissues since *Ehd1*$^{-/-}$ mice do not present symptoms similar to other known mitochondriopathies.

Other EHDs, namely EHD4, also seem to have a role in spermatogenesis. George and co-workers [53] observed a reduced testis weight in *Ehd4*$^{-/-}$ mice, an increase in germ cell proliferation and apoptosis, a progressive reduction in seminiferous tubule diameter, dysregulation of seminiferous epithelium and head abnormalities in elongated spermatids. These abnormalities resulted in lower sperm counts and reduced fertility. However, the *Ehd4* deletion also led to increased EHD1 levels in adult *Ehd4*$^{-/-}$ testis. This

compensation by EHD1 seemed to prevent the development of severe fertility defects in the adult mice. We also found enhanced *Ehd3* mRNA levels in the *Ehd1*$^{-/-}$ testis compared to the wildtype (Figure 4.18), suggesting that EHD1 is not the only EHD exerting a role in the testis. The inability of the *Ehd1*$^{-/-}$ mice to overcome the abnormalities in spermatogenesis and the fact that male knockouts were infertile indicate that the other EHD proteins were unable to fully compensate for the EHD1 absence. This points to an essential and unique role of EHD1 in spermatogenesis.

In agreement with the female *Ehd1*$^{-/-}$ mice phenotype, the examined human female patients proved to be fertile, since they were able to give birth to healthy children. Of the few male patients however, so far no progeny is known but also no fertility test has yet been performed. Therefore, it is not yet possible to say if the patients with the mutant EHD1 have a reduced fertility.

5.5 *Ehd1*$^{-/-}$ mouse and impaired proximal tubule endocytosis

The mouse kidney exhibited the second highest abundance of *Ehd1* mRNA levels (Figure 4.1). Within mouse kidney, EHD1 colocalizes with megalin (Figure 4.5) and cubilin (Figure 4.7) at the brush border of proximal tubules. EHD1 colocalization with megalin was also observed in the human kidney (Figure 4.5 C). Megalin and cubilin are the major players of endocytic processes in the proximal tubules, where the proteins filtered in renal glomeruli are removed from the tubular fluid thereby preventing low-molecular-weight proteinuria [114]. Due to the known role of EHD1 in the endocytic recycling pathway in other tissues, a role of EHD1 in the regulation of endocytic processes in the kidney seems likely. This hypothesis is strengthened by the observation of mild low-molecular-weight proteinuria in patients with the EHD1 R398W mutation. However, no abnormal kidney histology was observed in the *Ehd1*$^{-/-}$ (Figure 4.19) and no signs of proteinuria were detected after analysis of the urinary protein profile by a Coomassie staining. Since affected humans displayed only a mild proteinuria, it is possible that the same occurs with the mice and our assay was not sensitive enough to detect the proteinuria. Therefore, we examined the presence of the low-molecular-weight protein RBP (retinol binding protein) in the kidney. RBP is usually endocytosed in proximal tubules and a marker for low-molecular-weight proteinuria. Indeed, RBP was found in endosomes of the proximal tubules of the wildtype mice, but no RBP was observed in *Ehd1*$^{-/-}$ kidneys (Figure 4.20). This indicates that the *Ehd1*$^{-/-}$ proximal tubules were unable to reabsorb the RBP after its filtration in the glomerulus, being most likely excreted in the urine. To test the protein reabsorption ability of the kidney in more detail, we challenged the mice by injecting β_2-microglobulin, another protein marker for low-molecular-weight proteinuria, conjugated with Alexa Fluor 546

(AF546). After 30 min incubation, we quantified the amount of β_2-microglobulin-dependent fluorescence signal in plasma, kidney tissue and urine and its localization in the kidney was measured by fluorescence microscopy. Whilst β_2-microglobulin-AF546 was mainly localized in the early proximal tubules of control mice (Figure 4.21 A, B), the protein presented a broader distribution in knockout kidneys, being also present in the late proximal tubules (Figure 4.21 C, D). The difference of β_2-microglobulin distribution in the kidney could be explained by the reduced efficiency and/or lower reabsorption capacity of the early segments of the *Ehd1*$^{-/-}$ mouse proximal tubules leading to an "overflow" of β_2-microglobulin and consecutive reabsorption in later segments. In addition, the β_2-microglobulin-containing vesicles were farther moved away from the apical membrane in wildtype mice and closer to the apical membrane in knockout proximal tubules (Figure 4.23), suggesting a defect in vesicular transport and processing.
The quantification of β_2-microglobulin in the plasma, kidney and urine (Figure 4.22) revealed that the values in *Ehd1*$^{-/-}$ kidney tissue were lower when compared to the control (Figure 4.22 B), while more β_2-microglobulin was detected in the urine of the knockouts (Figure 4.22 C). This suggests that indeed the *Ehd1*$^{-/-}$ kidneys were less efficient in taking up β_2-microglobulin.

Finally, using *in vivo* imaging of β_2-microglobulin-AF546, we were able to investigate the proximal tubular reabsorption capacity in real time. The *Ehd1*$^{-/-}$ mice exhibited a reduced reabsorption capacity in the first minutes of endocytosis, with the tubules taking up less protein (Figure 4.24). The control tubules displayed the maximal tubular fluorescence much earlier in time than the *Ehd1*$^{-/-}$, which were often found not completely saturated but still displaying a slow protein uptake (Supplements, Figure 11.1). This suggests that *Ehd1* deletion leads to a mild impairment of the endocytic process, with the knockout tubules displaying a less efficient and slower reabsorption dynamics and possibly an impaired intracellular trafficking of cargo-containing endosomes (Figure 4.23). It is also possible that the endocytosis dynamics is being influenced by the rate of protein processing and transepithelial transport of the endocytosed β_2-microglobulin. The lack of EHD1, known for its role in vesicle fission [12], could lead to a delayed vesicular transport and reduced outflow of protein that in turn would cause intracellular accumulation of β_2-microglobulin, slowing down the endocytosis. However, this hypothesis must still be tested.

All these data point to a function of EHD1 in the endocytic pathway in the renal proximal tubules. Deletion of EHD1 in mice leads to a reduced reabsorption capacity and slower proximal tubular endocytosis dynamics making them prone to low-molecular-weight proteinuria. The kidneys of knockout mice partially compensate the impairment in

reabsorption extending protein uptake to the later part of the proximal tubules. But clearly, proximal tubular protein reabsorption in mice is only mildly impaired by the *Ehd1* knockout. Presumably, a more severe phenotype is prevented by compensatory mechanisms that might involve other members of the EHD family, however this compensation does not seem to be transcriptionally regulated (Figure 4.25 C). Since megalin, cubilin and amnionless are the main receptors in the proximal tubules responsible for endocytosis, we also examined the possibility of *Ehd1* deletion leading to changes in gene expression and protein localization, but both mRNA levels (Figure 4.25 A) and protein cellular localization (Figure 4.26) appeared unaltered. However, we observed a physical interaction between EHD1 and megalin in the mouse kidney using co-immunoprecipitation (Figure 4.6). After protein endocytosis, megalin normally returns to the cell surface from endocytic recycling compartment (ERC) in what is called “slow recycling”, but its transport directly from early endosomes (EE) to the plasma membrane, “fast recycling”, was also observed [132]. This “fast recycling” of megalin is dependent on Rab35 and connecdenn 2 [132]. The role of EHD1 in vesicle scission and receptor recycling from the ERC to the plasma membrane is very well documented [33,34], however no direct link between EHD1 and megalin was reported until now. Furthermore, EHD1 was also found to be recruited to the EE via Rab35 and connecdenn 1 [51]. This functional interaction between EHD1 and Rab35 was further confirmed by Kobayashi and co-workers, when they showed that active Rab35 forms a tripartite complex binding directly to MICAL-L1 and another Rab35 effector ACAP2, which then co-operatively recruits EHD1 for tubule formation [72]. More studies about megalin recycling must be performed to establish a link with EHD1, but those and our data strongly suggest an involvement of EHD1 in the recycling of megalin. Due to the great importance of megalin in proximal tubule endocytosis, it could be expected that impairment of megalin recycling would lead to a more severe phenotype. However, when we compared our *Ehd1*$^{-/-}$ mice phenotype with the one from *Lrp2*$^{-/-}$ mice (*Lrp2* is the gene encoding megalin) [117], several similarities were observed. The lack of megalin also did not affect the overall architecture of the epithelial cells or the appearance of the brush border surface. The histology of other renal tissues such as glomeruli, distal tubules and collecting ducts was also indistinguishable from control mice. Surprisingly, the absence of megalin did result in a significant reduction in the number of coated pits, endosomes, and lysosomes as compared to wildtype cells [117]. The analysis of the protein profile in urine from *Lrp2*$^{-/-}$ mice revealed the presence of low-molecular-weight proteins, such as vitamin D-binding protein, β_1-microglobulin and both RBP and β_2-microglobulin, indicating a phenotype for low-molecular-weight proteinuria, slightly more severe than in our mice but not as severe as expected. The differences observed in these two phenotypes could be explained by redundancy of protein function in

the endocytic pathway, which would compensate for EHD1 or megalin loss and reduce the severity of the phenotypes.

Only a few other studies about the EHD proteins in the kidney have been reported in the literature so far. An *Ehd3*$^{-/-}$ mouse was generated by George and co-workers [91] with the aim to study the renal role of EHD3, which was reported to be specifically expressed in the glomerular endothelium [133,134]. Although the authors confirmed the localization of EHD3 in the glomerular endothelial cells, the *Ehd3*$^{-/-}$ mouse displayed no glomerular abnormalities and no clear kidney phenotype [91]. Because EHD4 expression was found elevated in the glomerular endothelium suggesting a functional compensation, George and co-workers generated a *Ehd3*$^{-/-}$; *Ehd4*$^{-/-}$ double knockout mouse [91]. These mice presented a smaller size, possessed smaller and paler kidneys, were proteinuric and died between 3–24 weeks of age. Further histological analysis of the kidneys demonstrated microangiopathy-like glomerular lesions including thickening and duplication of glomerular basement membrane, endothelial swelling and loss of fenestrations. Segmental podocyte foot process effacement, mesangial interposition, and abnormal podocytic and mesangial marker expression were also observed. Finally, the glomerular endothelial VEGFR2 expression and localization was found altered in the absence of EHD3 and EHD4. These data obtained by George and co-workers suggest that EHD3 and EHD4 have roles in the endocytic traffic of key surface receptors such as VEGFR2, which is essential for physiological control of glomerular function.

Very recently, a study in a *Ehd4*$^{-/-}$ mouse with the objective to understand the role of EHD4 in the kidney was reported [95]. Rahman and co-workers observed that EHD4 is mainly expressed in the inner medullary collecting ducts, which suggests a potential role in both final urine formation and concentration. And in fact, *Ehd4*$^{-/-}$ mice produced higher volumes of dilute urine than control mice under baseline conditions. *Ehd4* deletion also led to a decreased accumulation of glycosylated AQP2 in the apical membrane of cultured principal cells. Rahman and co-workers further tested the role of EHD4 in renal water handling independent of voluntary water intake, by subjecting the mice to an acute water load with intraperitoneal injection. *Ehd4*$^{-/-}$ mice excreted almost 75% of the water load, whereas control mice excreted less than 50%. Rahman's data indicate that EHD4 may play an important role in the regulation of water homeostasis.

In summary, EHD proteins display high levels of amino acid sequence-similarity and -identity and presumably all of them are known to be involved in the endocytic pathway. In the kidney, EHD proteins have specific expression profiles that only partially overlap. In agreement with that, they appear to play distinct physiological functions in the kidney. EHD3 and EHD4 appear to be essential for control of glomerular function, EHD1 is important for protein reabsorption in proximal tubules, and EHD4 probably plays a role in

regulation of water homeostasis in the collecting ducts. More studies will be necessary to understand the molecular mechanisms behind these putative roles. However, the importance of EHD proteins in the regulation of kidney function seems to be undeniable.

5.6 R398W-EHD1 presents an altered cellular localization

To address the question whether the R398W mutation would indeed result in EHD1 loss-of-function, we used a proximal tubular cell line, LLC-PK1, stably expressing either the wildtype form of human EHD1 (WT-hEHD1) or the mutant variant found in the human patients (R398W-hEHD1) in order to investigate the cellular effects of the EHD1 mutation.
Interestingly, the mutation led to altered subcellular localization of EHD1. Whilst the WT-hEHD1 displayed a more cytoplasmic localization, around vesicle-like structures, the R398W-hEHD1 was localized mainly at the cell borders and in tubular structures (Figure 4.27). Furthermore, the R398W mutation also had an effect on protein stability and led to faster protein degradation (Figure 4.28). The R398W mutation leads to an amino acid substitution in the predicted linker region of the protein. The modified subcellular localization and, presumably, aggregation of the mutant EHD1 is possibly caused by misfolding of the EHD1 protein, which also led to activation of the quality control machinery of the cell that recognized the R398W-hEHD1 as defective and promoted its degradation.
Unfortunately, our attempts to quantify protein reabsorption in these LLC-PK1 cell lines revealed only small rates of transport irrespective of the kind of EHD1 expressed. This absence of a clear functional phenotype, although EHD1 appears mislocalized in the mutant cells, could be explained by efficient compensation by other proteins or a poor signal to noise ratio in a cell system that only reabsorbs small amounts of protein via endocytosis. It is also possible that the endogenous expression of the functional EHD1 in LLC-PK1 cells (Supplements, Figure 11.2) masks the defective function of the transfected R398W-hEHD1. Therefore, the functional assays need to be repeated in cells where the endogenous EHD1 is knocked-down in order to fully understand the effect of the mutation on protein function.

Although milder in nature, the renal phenotype of the *Ehd1*$^{-/-}$ mouse and the tendency for hearing deficiency at high frequencies recapitulates the low-molecular-weight proteinuria and the hearing loss observed in the human patients carrying the EHD1 R398W mutation. Together with the recessive inheritance of the human disorder, these data point to a "loss-of-function" as disease-causing mechanism. The abnormal subcellular localization of the R398W mutant in LLC-PK1 cells, however, would be in agreement with an additional gain-of-function component. Further studies are needed to address the consequences of the human EHD1 mutation, especially if the R398W mutant is mislocalized in patients' tissues or quickly degraded. As a model to further elaborate the pathophysiology of the EHD1 R398W protein and its fate in native tissues, our collaborator Ben Davies (University of Oxford) has generated a knockin mouse model. We have now started breeding these animals and will analyze their phenotype in 2018.

Due to recent reports about the essential role of EHD1 in ciliogenesis [76,79] we briefly addressed cilia formation in the kidney tissue of the *Ehd1*$^{-/-}$ mouse (Supplements, Figure 11.3). Cilia could me observed in both control and knockout mice, and also the human patients did not exhibit common symptoms of ciliopathies. The role of EHD1 in ciliogenesis will be further studied in the newly generated knockin mouse using more sophisticated methods.

6. Summary

Our co-worker Robert Kleta (University College London) examined 6 patients displaying hereditary mild low-molecular-weight proteinuria and hearing loss at high frequency range. Using linkage analysis and sequencing, Robert Kleta identified a new autosomal recessive mutation leading to a single amino acid substitution — R398W — in the C-terminal Eps15 homology domain (EHD) 1 protein. In mammals, EHD1 belongs to a family of four homologous proteins — EHD1–4 — that are presumably associated with the recycling of membrane cargo from the endocytic recycling compartment to the plasma membrane by fission of intracellular vesicles.

The objectives of this dissertation were i) to characterize the phenotype of a *Ehd1*$^{-/-}$ mouse model with the focus on the testis, inner ear and kidney and ii) to investigate the phenotype of the R398W mutant in a proximal tubular cell model.

In agreement with previous observations, our *Ehd1*$^{-/-}$ mice displayed enhanced prenatal lethality and male infertility, due to abnormal spermatogenesis that resulted in a low number of mature spermatozoa and impaired sperm motility. The study of the inner ear by auditory brainstem response measurements revealed a diminished hearing capacity at high frequency in the *Ehd1*$^{-/-}$ mice. *In vivo* assays of renal proximal tubular endocytosis in knockout mice exhibited a reduced protein reabsorption capacity and slower endocytosis rate that made the mice prone to low-molecular-weight proteinuria.

Both the renal and the inner ear phenotypes of the *Ehd1*$^{-/-}$ mouse recapitulate the low-molecular-weight proteinuria and the hearing loss observed in the human patients carrying the EHD1 R398W mutation. These data together with the recessive inheritance of the human disorder point to a “loss-of-function” as disease-causing mechanism. However, in a proximal tubular cell model a striking mislocalization of the R398W mutant was observed. This would be in agreement with an additional “gain-of-function” component. To further improve the understanding of the pathophysiology of the EHD1 R398W mutant protein in native tissues the phenotype of a knockin mouse model will be analyzed.

Taken together, the findings presented in this thesis provide novel insights in particular into the physiological roles of EHD1 in the kidney and the inner ear. These findings lay the foundations for future studies of our laboratory addressing the cellular and molecular pathomechanisms leading to EHD1-associated human diseases.

7. Zusammenfassung

Unser Kooperationspartner Robert Kleta, University College London, hat sechs Patienten mit familiärer "low molecular weight" Proteinurie und beeinträchtigtem Hörvermögen klinisch und genetisch untersucht. Mittels Kopplungsanalysen und DNA-Sequenzierung gelang es ihm, eine krankheitsassoziierte, autosomal rezessive Mutation (R398W) im C-Terminus des "Eps15 Homology Domain (EHD) 1"-Proteins zu identifizieren. Die EHD-Proteinfamilie hat bei Säugetieren vier Mitglieder (EHD1-4). Man geht davon aus, dass diese Proteine am Recycling von Membranproteinen aus intrazellulären Membrankompartimenten zur Plasmamembran beteiligt sind, indem sie das Abschnüren von Vesikeln aus den "Endocytic Recycling"-Kompartiment fördern.

Das Ziel dieser Doktorarbeit war es, 1.) den Nieren-, Innenohr- und Hoden-Phänotyp der *Ehd1*$^{-/-}$-Maus zu untersuchen und 2.) die Auswirkungen der R398W-Mutation in einem Zellmodell des renalen proximalen Tubulus zu erforschen.

In Übereinstimmung mit publizierten Daten zeigten unsere *Ehd1*$^{-/-}$-Mäuse eine erhöhte perinatale Letalität und Infertilität von männlichen Tieren, wobei letztere durch eine abnorme Spermatogenese und eine konsekutiv erniedrigte Anzahl reifer Spermien und eine beeinträchtigte Spermienmotilität bedingt war.

Bei "Auditory Brainstem Response"-Messungen zeigte sich, dass ähnlich den Patienten auch die *Ehd1*$^{-/-}$-Mäuse eine Hörminderung bei hohen Frequenzen aufweisen. In Untersuchungen an lebenden *Ehd1*$^{-/-}$-Mäusen beobachteten wir außerdem eine - wenn auch gering - eingeschränkte Kapazität zur Proteinresorption in proximalen Tubuli der Niere.

Somit rekapituliert die *Ehd1*$^{-/-}$-Maus hinsichtlich des Innenohrphänotyps und der Neigung zur Proteinurie den klinischen Phänotyp der Patienten. Gemeinsam mit der Tatsache, dass die Erkrankung autosomal rezessiv vererbt wird, spricht dies für den "Loss-of-Function"-Charakter der R398W-Mutation. Jedoch wird diese Schlussfolgerung durch Befunde an unserem proximal tubulären Zellmodell eingeschränkt, wo die R398W-Mutante eine pathologische subzelluläre Verteilung aufwies und damit zusätzlich eine "Gain-of-Function"-Komponente hinzukommen könnte. Um die Pathophysiologie der R398W besser zu verstehen, werden wir zukünftig eine R398W-Knockin-Maus untersuchen, die gegenwärtig bei uns gezüchtet wird.

Zusammenfassend lässt sich sagen, dass die in dieser Dissertation vorgestellten Daten neue Erkenntnisse zur physiologischen Bedeutung von EHD1 insbesondere in der Niere und dem Innenohr geliefert haben. Diese Resultate stellen eine wichtige Basis für

zukünftige Studien unseres Labors dar, die zum Ziel haben, die zellulären und molekularen Pathomechanismen EHD1-assoziierter Erkrankungen zu untersuchen.

8. References

1. Mintz, L. *et al.* EHD1--an EH-domain-containing protein with a specific expression pattern. *Genomics* **59,** 66–76 (1999).

2. Pohl, U. *et al.* EHD2, EHD3, and EHD4 encode novel members of a highly conserved family of EH domain-containing proteins. *Genomics* **63,** 255–62 (2000).

3. www.uniprot.org.

4. Naslavsky, N. & Caplan, S. C-terminal EH-domain-containing proteins: consensus for a role in endocytic trafficking, EH? *J. Cell Sci.* **118,** 4093–101 (2005).

5. Grant, B. D. & Caplan, S. Mechanisms of EHD/RME-1 protein function in endocytic transport. *Traffic* **9,** 2043–52 (2008).

6. Grant, B. *et al.* Evidence that RME-1, a conserved C. elegans EH-domain protein, functions in endocytic recycling. *Nat. Cell Biol.* **3,** 573–9 (2001).

7. Smith, C. A., Dho, S. E., Donaldson, J., Tepass, U. & McGlade, C. J. The cell fate determinant numb interacts with EHD/Rme-1 family proteins and has a role in endocytic recycling. *Mol. Biol. Cell* **15,** 3698–708 (2004).

8. Blume, J. J., Halbach, A., Behrendt, D., Paulsson, M. & Plomann, M. EHD proteins are associated with tubular and vesicular compartments and interact with specific phospholipids. *Exp. Cell Res.* **313,** 219–231 (2007).

9. George, M. *et al.* Shared as well as distinct roles of EHD proteins revealed by biochemical and functional comparisons in mammalian cells and C. elegans. *BMC Cell Biol.* **8,** 3 (2007).

10. Sengupta, S. *et al.* EHD4 and CDH23 are interacting partners in cochlear hair cells. *J. Biol. Chem.* **284,** 20121–9 (2009).

11. Arya, P. *et al.* The endocytic recycling regulatory protein EHD1 Is required for ocular lens development. *Dev. Biol.* **408,** 41–55 (2015).

12. Naslavsky, N. & Caplan, S. EHD proteins: key conductors of endocytic transport. *Trends Cell Biol.* **21,** 122–31 (2011).

13. Daumke, O. *et al.* Architectural and mechanistic insights into an EHD ATPase involved in membrane remodelling. *Nature* **449,** 923–7 (2007).

14. Melo, A. A. *et al.* Structural insights into the activation mechanism of dynamin-like EHD ATPases. *Proc. Natl. Acad. Sci. U. S. A.* **114,** 5629–5634 (2017).

15. Confalonieri, S. & Di Fiore, P. P. The Eps15 homology (EH) domain. *FEBS Lett.* **513,** 24–29 (2002).

16. Fazioli, F., Minichiello, L., Matoskova, B., Wong, W. T. & Di Fiore, P. P. Eps15, a Novel Tyrosine Kinase Substrate, Exhibits Transforming Activity. *Mol. Cell. Biol.* **13,** 5814–5828 (1993).

17. Wong, W. T. *et al.* A protein-binding domain, EH, identified in the receptor tyrosine kinase substrate Eps15 and conserved in evolution. *Proc. Natl. Acad. Sci. U. S. A.* **92,** 9530–9534 (1995).

18. Whitehead, B., Tessari, M., Carotenuto, A., van Bergen en Henegouwen, P. M. & Vuister, G. W. The EH1 domain of Eps15 is structurally classified as a member of the S100 subclass of EF-hand-containing proteins. *Biochemistry* **38,** 11271–7 (1999).

19. de Beer, T., Carter, R. E., Lobel-Rice, K. E., Sorkin, A. & Overduin, M. Structure and Asn-Pro-Phe binding pocket of the Eps15 homology domain. *Science* **281,** 1357–60 (1998).

20. Enmon, J. L., de Beer, T. & Overduin, M. Solution structure of Eps15's third EH domain reveals coincident Phe-Trp and Asn-Pro-Phe binding sites. *Biochemistry* **39,** 4309–19 (2000).

21. Koshiba, S., Kigawa, T., Iwahara, J., Kikuchi, A. & Yokoyama, S. Solution structure of the Eps15 homology domain of a human POB1 (partner of RalBP1). *FEBS Lett.* **442,** 138–42 (1999).

22. Kim, S., Cullis, D. N., Feig, L. A. & Baleja, J. D. Solution structure of the Reps1 EH domain and characterization of its binding to NPF target sequences. *Biochemistry* **40,** 6776–85 (2001).

23. Kieken, F., Jović, M., Naslavsky, N., Caplan, S. & Sorgen, P. L. EH domain of EHD1. *J. Biomol. NMR* **39,** 323–9 (2007).

24. Polo, S., Confalonieri, S., Salcini, A. E. & Di Fiore, P. P. EH and UIM: endocytosis and more. *Sci. STKE* **2003,** re17 (2003).

25. Strynadka, N. C. & James, M. N. Crystal structures of the helix-loop-helix calcium-binding proteins. *Annu. Rev. Biochem.* **58,** 951–98 (1989).

26. Lewit-Bentley, A. & Réty, S. EF-hand calcium-binding proteins. *Curr. Opin. Struct. Biol.* **10,** 637–43 (2000).

27. Naslavsky, N., Rahajeng, J., Chenavas, S., Sorgen, P. L. & Caplan, S. EHD1 and Eps15 interact with phosphatidylinositols via their Eps15 homology domains. *J. Biol. Chem.* **282,** 16612–22 (2007).

28. Salcini, A. E. *et al.* Binding specificity and in vivo targets of the EH domain, a novel protein-protein interaction module. *Genes Dev.* **11,** 2239–49 (1997).

29. Paoluzi, S. *et al.* Recognition specificity of individual EH domains of mammals and yeast. *EMBO J.* **17,** 6541–50 (1998).

30. Henry, G. D., Corrigan, D. J., Dineen, J. V & Baleja, J. D. Charge effects in the selection of NPF motifs by the EH domain of EHD1. *Biochemistry* **49,** 3381–92 (2010).

31. Kieken, F. *et al.* Mechanism for the selective interaction of C-terminal Eps15 homology domain proteins with specific Asn-Pro-Phe-containing partners. *J. Biol. Chem.* **285,** 8687–94 (2010).

32. Xu, Y., Shi, H., Wei, S., Wong, S. H. & Hong, W. Mutually exclusive interactions of EHD1 with GS32 and syndapin II. *Mol. Membr. Biol.* **21,** 269–277 (2004).

33. Guilherme, A., Soriano, N. a., Furcinitti, P. S. & Czech, M. P. Role of EHD1 and EHBP1 in perinuclear sorting and insulin-regulated GLUT4 recycling in 3T3-L1 adipocytes. *J. Biol. Chem.* **279,** 40062–75 (2004).

34. Naslavsky, N., Boehm, M., Backlund, P. S. & Caplan, S. Rabenosyn-5 and EHD1 interact and sequentially regulate protein recycling to the plasma membrane. *Mol. Biol. Cell* **15,** 2410–22 (2004).

35. Naslavsky, N., Rahajeng, J., Sharma, M., Jovic, M. & Caplan, S. Interactions between EHD proteins and Rab11-FIP2: a role for EHD3 in early endosomal transport. *Mol. Biol. Cell* **17,** 163–77 (2006).

36. Kieken, F. *et al.* Structural insight into the interaction of proteins containing NPF, DPF, and GPF motifs with the C-terminal EH-domain of EHD1. *Protein Sci.* **18,** 2471–9 (2009).

37. Caplan, S. *et al.* A tubular EHD1-containing compartment involved in the recycling of major histocompatibility complex class I molecules to the plasma membrane. *EMBO J.* **21,** 2557–67 (2002).

38. Lee, D. *et al.* ATP binding regulates oligomerization and endosome association of RME-1 family proteins. *J. Biol. Chem.* **280,** 17213–20 (2005).

39. Conner, S. D. & Schmid, S. L. Regulated portals of entry into the cell. *Nature* **422,** 37–44 (2003).

40. Di Fiore, P. P. & von Zastrow, M. Endocytosis, signaling, and beyond. *Cold Spring Harb. Perspect. Biol.* **6,** (2014).

41. Grant, B. D. & Donaldson, J. G. Pathways and mechanisms of endocytic recycling. *Nat. Rev. Mol. Cell Biol.* **10,** 597–608 (2009).

42. Doherty, G. J. & McMahon, H. T. Mechanisms of endocytosis. *Annu. Rev. Biochem.* **78,** 857–902 (2009).

43. Goldenring, J. R. Recycling endosomes. *Curr. Opin. Cell Biol.* **35,** 117–22 (2015).

44. Zhang, J., Naslavsky, N. & Caplan, S. Rabs and EHDs: alternate modes for traffic control. *Biosci. Rep.* **32,** 17–23 (2012).

45. Stenmark, H. Rab GTPases as coordinators of vesicle traffic. *Nat. Rev. Mol. Cell Biol.* **10,** 513–25 (2009).

46. McLauchlan, H. *et al.* A novel role for Rab5-GDI in ligand sequestration into clathrin-coated pits. *Curr. Biol.* **8,** 34–45 (1998).

47. Lanzetti, L. *et al.* The Eps8 protein coordinates EGF receptor signalling through Rac and trafficking through Rab5. *Nature* **408,** 374–7 (2000).

48. Delevoye, C. *et al.* Recycling endosome tubule morphogenesis from sorting endosomes requires the kinesin motor KIF13A. *Cell Rep.* **6,** 445–54 (2014).

49. Baetz, N. W. & Goldenring, J. R. Rab11-family interacting proteins define spatially and temporally distinct regions within the dynamic Rab11a-dependent recycling system. *Mol. Biol. Cell* **24,** 643–58 (2013).

50. Roland, J. T., Kenworthy, A. K., Peranen, J., Caplan, S. & Goldenring, J. R. Myosin Vb interacts with Rab8a on a tubular network containing EHD1 and EHD3. *Mol. Biol. Cell* **18,** 2828–37 (2007).

51. Allaire, P. D. *et al.* The Connecdenn DENN domain: a GEF for Rab35 mediating cargo-specific exit from early endosomes. *Mol. Cell* **37,** 370–82 (2010).

52. Sharma, M., Giridharan, S. S. P., Rahajeng, J., Naslavsky, N. & Caplan, S. MICAL-L1 links EHD1 to tubular recycling endosomes and regulates receptor recycling. *Mol. Biol. Cell* **20,** 5181–94 (2009).

53. George, M. *et al.* Ehd4 is required to attain normal prepubertal testis size but dispensable for fertility in male mice. *Genesis* **48,** 328–342 (2010).

54. Rapaport, D. *et al.* Recycling to the plasma membrane is delayed in EHD1 knockout mice. *Traffic* **7,** 52–60 (2006).

55. Picciano, J. A., Ameen, N., Grant, B. D. & Bradbury, N. A. Rme-1 regulates the recycling of the cystic fibrosis transmembrane conductance regulator. *Am. J. Physiol. Cell Physiol.* **285,** C1009-18 (2003).

56. Lin, S. X., Grant, B., Hirsh, D. & Maxfield, F. R. Rme-1 regulates the distribution and function of the endocytic recycling compartment in mammalian cells. *Nat. Cell Biol.* **3,** 567–72 (2001).

57. Park, M., Penick, E. C., Edwards, J. G., Kauer, J. A. & Ehlers, M. D. Recycling endosomes supply AMPA receptors for LTP. *Science* **305,** 1972–5 (2004).

58. Walseng, E., Bakke, O. & Roche, P. A. Major histocompatibility complex class II-peptide complexes internalize using a clathrin- and dynamin-independent endocytosis pathway. *J. Biol. Chem.* **283,** 14717–27 (2008).

59. Jović, M., Naslavsky, N., Rapaport, D., Horowitz, M. & Caplan, S. EHD1 regulates beta1 integrin endosomal transport: effects on focal adhesions, cell spreading and migration. *J. Cell Sci.* **120,** 802–14 (2007).

60. Chung, H. J., Qian, X., Ehlers, M., Jan, Y. N. & Jan, L. Y. Neuronal activity regulates phosphorylation-dependent surface delivery of G protein-activated inwardly rectifying potassium channels. *Proc. Natl. Acad. Sci. U. S. A.* **106,** 629–34 (2009).

61. Gao, Y. *et al.* Recycling of the Ca2+-activated K+ channel, KCa2.3, is dependent upon RME-1, Rab35/EPI64C, and an N-terminal domain. *J. Biol. Chem.* **285,** 17938–53 (2010).

62. Cai, B., Katafiasz, D., Horejsi, V. & Naslavsky, N. Pre-sorting endosomal transport of the GPI-anchored protein, CD59, is regulated by EHD1. *Traffic* **12,** 102–120 (2011).

63. Rotem-Yehudar, R., Galperin, E. & Horowitz, M. Association of insulin-like growth factor 1 receptor with EHD1 and SNAP29. *J. Biol. Chem.* **276,** 33054–60 (2001).

64. Cai, B., Xie, S., Caplan, S. & Naslavsky, N. GRAF1 forms a complex with MICAL-L1 and EHD1 to cooperate in tubular recycling endosome vesiculation. *Front. Cell Dev. Biol.* **2,** 1–14 (2014).

65. Giridharan, S. S. P., Cai, B., Vitale, N., Naslavsky, N. & Caplan, S. Cooperation of MICAL-L1, syndapin2, and phosphatidic acid in tubular recycling endosome biogenesis. *Mol. Biol. Cell* **24,** 1776–90, S1-15 (2013).

66. Galperin, E. *et al.* EHD3: a protein that resides in recycling tubular and vesicular membrane

structures and interacts with EHD1. *Traffic* **3,** 575–89 (2002).

67. Sharma, M., Naslavsky, N. & Caplan, S. A role for EHD4 in the regulation of early endosomal transport. *Traffic* **9,** 995–1018 (2008).

68. Cai, B. *et al.* Differential roles of C-terminal Eps15 homology domain proteins as vesiculators and tubulators of recycling endosomes. *J. Biol. Chem.* **288,** 30172–80 (2013).

69. Lee, S. *et al.* Transport through recycling endosomes requires EHD1 recruitment by a phosphatidylserine translocase. *EMBO J.* **34,** 669–88 (2015).

70. Reinecke, J. B., Katafiasz, D., Naslavsky, N. & Caplan, S. Regulation of Src trafficking and activation by the endocytic regulatory proteins MICAL-L1 and EHD1. *J. Cell Sci.* **127,** 1684–98 (2014).

71. Yap, C. C. C., Lasiecka, Z. M., Caplan, S. & Winckler, B. Alterations of EHD1/EHD4 protein levels interfere with L1/NgCAM endocytosis in neurons and disrupt axonal targeting. *J. Neurosci.* **30,** 6646–6657 (2010).

72. Kobayashi, H. & Fukuda, M. Rab35 establishes the EHD1-association site by coordinating two distinct effectors during neurite outgrowth. *J. Cell Sci.* **126,** 2424–35 (2013).

73. Wu, C. *et al.* The importance of EHD1 in neurite outgrowth contributing to the functional recovery after spinal cord injury. *Int. J. Dev. Neurosci.* **52,** 24–32 (2016).

74. Naslavsky, N., Rahajeng, J., Rapaport, D., Horowitz, M. & Caplan, S. EHD1 regulates cholesterol homeostasis and lipid droplet storage. *Biochem. Biophys. Res. Commun.* **357,** 792–9 (2007).

75. Farmer, T. *et al.* Control of mitochondrial homeostasis by endocytic regulatory proteins. *J. Cell Sci.* (2017). doi:10.1242/jcs.204537

76. Lu, Q. *et al.* Early steps in primary cilium assembly require EHD1/EHD3-dependent ciliary vesicle formation. *Nat. Cell Biol.* **17,** 228–40 (2015).

77. Rainey, M. a *et al.* The endocytic recycling regulator EHD1 is essential for spermatogenesis and male fertility in mice. *BMC Dev. Biol.* **10,** 37 (2010).

78. Posey, A. D. *et al.* EHD1 mediates vesicle trafficking required for normal muscle growth and transverse tubule development. *Dev. Biol.* **387,** 179–90 (2014).

79. Bhattacharyya, S. *et al.* Endocytic recycling protein EHD1 regulates primary cilia morphogenesis and SHH signaling during neural tube development. *Sci. Rep.* **6,** 20727 (2016).

80. Guilherme, A. *et al.* EHD2 and the Novel EH Domain Binding Protein EHBP1 Couple Endocytosis to the Actin Cytoskeleton. *J. Biol. Chem.* **279,** 10593–10605 (2004).

81. Doherty, K. R. *et al.* The endocytic recycling protein EHD2 interacts with myoferlin to regulate myoblast fusion. *J. Biol. Chem.* **283,** 20252–60 (2008).

82. Morén, B. *et al.* EHD2 regulates caveolar dynamics via ATP-driven targeting and oligomerization. *Mol. Biol. Cell* **23,** 1316–29 (2012).

83. Hoernke, M. *et al.* EHD2 restrains dynamics of caveolae by an ATP-dependent, membrane-bound, open conformation. *Proc. Natl. Acad. Sci. U. S. A.* 201614066 (2017). doi:10.1073/pnas.1614066114

84. Shvets, E., Ludwig, A. & Nichols, B. J. News from the caves: Update on the structure and function of caveolae. *Curr. Opin. Cell Biol.* **29,** 99–106 (2014).

85. Naslavsky, N., McKenzie, J., Altan-Bonnet, N., Sheff, D. & Caplan, S. EHD3 regulates early-endosome-to-Golgi transport and preserves Golgi morphology. *J. Cell Sci.* **122,** 389–400 (2009).

86. Bahl, K. *et al.* EHD3 Protein Is Required for Tubular Recycling Endosome Stabilization, and an Asparagine-Glutamic Acid Residue Pair within Its Eps15 Homology (EH) Domain Dictates Its Selective Binding to NPF Peptides. *J. Biol. Chem.* **291,** 13465–78 (2016).

87. Cabasso, O., Pekar, O. & Horowitz, M. SUMOylation of EHD3 Modulates Tubulation of the Endocytic Recycling Compartment. *PLoS One* **10,** e0134053 (2015).

88. Reinecke, J. B., Katafiasz, D., Naslavsky, N. & Caplan, S. Novel functions for the endocytic regulatory proteins MICAL-L1 and EHD1 in mitosis. *Traffic* **16,** 48–67 (2015).

89. Curran, J. *et al.* EHD3-dependent endosome pathway regulates cardiac membrane excitability and physiology. *Circ. Res.* **115,** 68–78 (2014).

90. Gudmundsson, H. *et al.* EH domain proteins regulate cardiac membrane protein targeting. *Circ. Res.* **107,** 84–95 (2010).

91. George, M. *et al.* Renal thrombotic microangiopathy in mice with combined deletion of endocytic recycling regulators EHD3 and EHD4. *PLoS One* **6,** e17838 (2011).

92. Shao, Y. *et al.* Pincher, a pinocytic chaperone for nerve growth factor/TrkA signaling endosomes. *J. Cell Biol.* **157,** 679–91 (2002).

93. Valdez, G. *et al.* Pincher-mediated macroendocytosis underlies retrograde signaling by

neurotrophin receptors. *J. Neurosci.* **25,** 5236–47 (2005).

94. Joset, A., Dodd, D. A., Halegoua, S. & Schwab, M. E. Pincher-generated Nogo-A endosomes mediate growth cone collapse and retrograde signaling. *J. Cell Biol.* **188,** 271–285 (2010).

95. Rahman, S. S. *et al.* EHD4 is a novel regulator of urinary water homeostasis. *FASEB J.* fj.201601182RR (2017). doi:10.1096/fj.201601182RR

96. Dervan, E. W. *et al.* Protein macroarray profiling of serum autoantibodies in pseudoexfoliation glaucoma. *Invest. Ophthalmol. Vis. Sci.* **51,** 2968–75 (2010).

97. Cortez, K. J. *et al.* Functional genomics of innate host defense molecules in normal human monocytes in response to Aspergillus fumigatus. *Infect. Immun.* **74,** 2353–65 (2006).

98. Hansel, D. E. *et al.* Met proto-oncogene and insulin-like growth factor binding protein 3 overexpression correlates with metastatic ability in well-differentiated pancreatic endocrine neoplasms. *Clin. Cancer Res.* **10,** 6152–6158 (2004).

99. Ammann, L. P. & Goodman, S. R. Cluster analysis for the impact of sickle cell disease on the human erythrocyte protein interactome. *Exp. Biol. Med. (Maywood).* **234,** 703–11 (2009).

100. Galindo, C. L. *et al.* Identification of Aeromonas hydrophila cytotoxic enterotoxin-induced genes in macrophages using microarrays. *J. Biol. Chem.* **278,** 40198–40212 (2003).

101. Tripathi, A. K., Sha, W., Shulaev, V., Stins, M. F. & Sullivan, D. J. Plasmodium falciparum-infected erythrocytes induce NF-kappaB regulated inflammatory pathways in human cerebral endothelium. *Blood* **114,** 4243–52 (2009).

102. Jansen, F. H. *et al.* Exosomal secretion of cytoplasmic prostate cancer xenograft-derived proteins. *Mol Cell Proteomics* **8,** 1192–1205 (2009).

103. Shin, J. *et al.* Lesional gene expression profiling in cutaneous T-cell lymphoma reveals natural clusters associated with disease outcome. *Blood* **110,** 3015–27 (2007).

104. Tong, D. *et al.* Increased Eps15 homology domain 1 and RAB11FIP3 expression regulate breast cancer progression via promoting epithelial growth factor receptor recycling. *Tumour Biol.* **39,** 1010428317691010 (2017).

105. Meng, Q. *et al.* Mammalian Eps15 homology domain 1 promotes metastasis in non-small cell lung cancer by inducing epithelial-mesenchymal transition. *Oncotarget* **8,** 22433–22442 (2017).

106. Buggia-Prévot, V. *et al.* A function for EHD family proteins in unidirectional retrograde dendritic transport of BACE1 and Alzheimer's disease Aβ production. *Cell Rep.* **5,** 1552–63 (2013).

107. Maher, E. A. *et al.* Malignant glioma: Genetics and biology of a grave matter. *Genes Dev.* **15,** 1311–1333 (2001).

108. Yohannes, E., Chang, J., Christ, G. J., Davies, K. P. & Chance, M. R. Proteomics analysis identifies molecular targets related to diabetes mellitus-associated bladder dysfunction. *Mol Cell Proteomics* **7,** 1270–1285 (2008).

109. Chen, C. *et al.* Gene expression profiling identifies genes predictive of oral squamous cell carcinoma. *Cancer Epidemiol. Biomarkers Prev.* **17,** 2152–2162 (2008).

110. Taniwaki, M. *et al.* Gene expression profiles of small-cell lung cancers: Molecular signatures of lung cancer. *Int. J. Oncol.* **29,** 567–575 (2006).

111. Desmond, J. C. *et al.* Discovery of epigenetically silenced genes in acute myeloid leukemias. *Leuk. Off. J. Leuk. Soc. Am. Leuk. Res. Fund, U.K* **21,** 1026–1034 (2007).

112. Chukkapalli, S. *et al.* Ehd3, a regulator of vesicular trafficking, is silenced in gliomas and functions as a tumor suppressor by controlling cell cycle arrest and apoptosis. *Carcinogenesis* **35,** 877–885 (2014).

113. Allantaz, F. *et al.* Blood leukocyte microarrays to diagnose systemic onset juvenile idiopathic arthritis and follow the response to IL-1 blockade. *J. Exp. Med.* **204,** 2131–44 (2007).

114. Christensen, E. I., Verroust, P. J. & Nielsen, R. Receptor-mediated endocytosis in renal proximal tubule. *Pflugers Arch.* **458,** 1039–48 (2009).

115. Christensen, E. I. Rapid membrane recycling in renal proximal tubule cells. *Eur. J. Cell Biol.* **29,** 43–9 (1982).

116. Christensen, E. I. & Birn, H. Megalin and cubilin: multifunctional endocytic receptors. *Nat. Rev. Mol. Cell Biol.* **3,** 256–66 (2002).

117. Leheste, J. R. *et al.* Megalin knockout mice as an animal model of low molecular weight proteinuria. *Am. J. Pathol.* **155,** 1361–70 (1999).

118. Heffner, H. E. & Heffner, R. S. Hearing ranges of laboratory animals. *J. Am. Assoc. Lab. Anim. Sci.* **46,** 20–2 (2007).

119. Skarnes, W. C. *et al.* A conditional knockout resource for the genome-wide study of mouse

gene function. *Nature* **474,** 337–42 (2011).

120. Pettitt, S. J. *et al.* Agouti C57BL/6N embryonic stem cells for mouse genetic resources. *Nat. Methods* **6,** 493–5 (2009).

121. Sauer, B. & Henderson, N. Site-specific DNA recombination in mammalian cells by the Cre recombinase of bacteriophage P1. *Proc. Natl. Acad. Sci. U. S. A.* **85,** 5166–70 (1988).

122. Nielsen, R. *et al.* Characterization of a kidney proximal tubule cell line, LLC-PK1, expressing endocytotic active megalin. *J. Am. Soc. Nephrol.* **9,** 1767–76 (1998).

123. Vikhe Patil, K., Canlon, B. & Cederroth, C. R. High quality RNA extraction of the mammalian cochlea for qRT-PCR and transcriptome analyses. *Hear. Res.* **325,** 42–48 (2015).

124. Tziridis, K., Buerbank, S., Eulenburg, V., Dlugaiczyk, J. & Schulze, H. Deficit in acoustic signal-in-noise detection in glycine receptor α3 subunit knockout mice. *Eur. J. Neurosci.* **45,** 581–586 (2017).

125. Krauss, P., Tziridis, K., Buerbank, S., Schilling, A. & Schulze, H. Therapeutic Value of Ginkgo biloba Extract EGb 761® in an Animal Model (Meriones unguiculatus) for Noise Trauma Induced Hearing Loss and Tinnitus. *PLoS One* **11,** e0157574 (2016).

126. Henry, K. R. Auditory brainstem volume-conducted responses: origins in the laboratory mouse. *J. Am. Aud. Soc.* **4,** 173–8 (1979).

127. Phillips, D. M. Comparative analysis of mammalian sperm motility. *J. Cell Biol.* **53,** 561–573 (1972).

128. Yan, H. H. N., Mruk, D. D., Lee, W. M. & Cheng, C. Y. Blood-testis barrier dynamics are regulated by testosterone and cytokines via their differential effects on the kinetics of protein endocytosis and recycling in Sertoli cells. *FASEB J.* **22,** 1945–59 (2008).

129. Chan, D. C. Fusion and fission: interlinked processes critical for mitochondrial health. *Annu. Rev. Genet.* **46,** 265–87 (2012).

130. Honda, S. & Hirose, S. Stage-specific enhanced expression of mitochondrial fusion and fission factors during spermatogenesis in rat testis. *Biochem. Biophys. Res. Commun.* **311,** 424–32 (2003).

131. Aldridge, A. C. *et al.* Roles for Drp1, a dynamin-related protein, and milton, a kinesin-associated protein, in mitochondrial segregation, unfurling and elongation during Drosophila spermatogenesis. *Fly (Austin).* **1,** 38–46 (2007).

132. Shah, M., Baterina, O. Y., Taupin, V. & Farquhar, M. G. ARH directs megalin to the endocytic recycling compartment to regulate its proteolysis and gene expression. *J. Cell Biol.* **202,** 113–27 (2013).

133. Patrakka, J. *et al.* Expression and subcellular distribution of novel glomerulus-associated proteins dendrin, ehd3, sh2d4a, plekhh2, and 2310066E14Rik. *J. Am. Soc. Nephrol.* **18,** 689–97 (2007).

134. Brunskill, E. W. & Potter, S. S. Gene expression programs of mouse endothelial cells in kidney development and disease. *PLoS One* **5,** e12034 (2010).

9. List of Figures

Figure 1.1: Representative audiogram from one of the patients. 5
Figure 1.2: Pedigrees of the four families of the examined patients. 6
Figure 1.3: Diagram of EHD domain architecture. 8
Figure 1.4: The structure of mouse EHD2 dimer. 8
Figure 1.5: Proposed model of EHD proteins function. 11
Figure 1.6: Regulation of endocytic transport by EHD proteins, Rabs and effectors. 12
Figure 1.7: Schematic model of a nephron. 21
Figure 1.8: Schematic model of the Organ of Corti. 23
Figure 1.9: Seminiferous tubule. 24
Figure 3.1: Different alleles for *Ehd1* locus. 39
Figure 4.1: *Ehd1* mRNA levels in wildtype mouse tissues. 57
Figure 4.2: *Ehd1* promotor-driven X-Gal staining in adult *Ehd1*$^{+/-}$ mouse tissues. 58
Figure 4.3: EHD1 localization in the seminiferous tubules of adult mice. 59
Figure 4.4: EHD1 localization in the renal proximal tubules of adult mice. 60
Figure 4.5: EHD1 colocalization with Megalin. 62
Figure 4.6: EHD1 interaction with megalin in *Ehd1*$^{+/+}$ mouse kidney. 63
Figure 4.7: EHD1 colocalization with Cubilin 64
Figure 4.8: *Ehd1* mRNA levels in *Ehd1*$^{-/-}$ mouse tissues compared to *Ehd1*$^{+/+}$. 65
Figure 4.9: *Ehd1*$^{-/-}$ mice body weight compared to control mice. 66
Figure 4.10: Ocular abnormalities in the *Ehd1*$^{-/-}$ mouse. 67
Figure 4.11: Histology of the cochlea in the *Ehd1*$^{-/-}$ mouse compared to the control. 68
Figure 4.12: Unspecific EHD1 antibody binding in the mouse cochlea. 68
Figure 4.13: Comparison of hearing ability of the *Ehd1*$^{-/-}$ mouse to the control. 69
Figure 4.14: *Ehd3* mRNA levels in the *Ehd1*$^{-/-}$ mouse cochlea compared to the control. 70
Figure 4.15: Testes and epididymides weight in *Ehd1*$^{-/-}$ mice compared to controls. 71
Figure 4.16: Histology of the testis and epididymis in the *Ehd1*$^{-/-}$ mouse compared to the control. 74
Figure 4.17: Electron micrographs of the seminiferous tubules in the *Ehd1*$^{-/-}$ mouse compared to the control. 76
Figure 4.18: *Ehd3* mRNA levels in the *Ehd1*$^{-/-}$ mouse testis and epididymis compared to the control. 76
Figure 4.19: Electron micrographs of the renal proximal tubules in the *Ehd1*$^{-/-}$ mouse compared to the control. 77
Figure 4.20: Retinol binding protein (RBP) absence in the *Ehd1*$^{-/-}$ mouse kidney. 78

Figure 4.21: β_2-microglobulin proximal tubular localization in the *Ehd1*$^{-/-}$ mouse compared to the control. 79
Figure 4.22: Quantification of β_2-microglobulin levels in plasma, kidney and urine of the *Ehd1*$^{-/-}$ mouse compared to the control. 80
Figure 4.23: β_2-microglobulin endocytosis by proximal tubular cells in the *Ehd1*$^{-/-}$ mouse compared to the control. 82
Figure 4.24: Live-imaging of β_2-microglobulin endocytosis by the proximal tubules in the *Ehd1*$^{-/-}$ mouse compared to the control. 85
Figure 4.25: mRNA levels of EHD1 potential partners in the *Ehd1*$^{-/-}$ mouse kidney compared to the control. 86
Figure 4.26: Localization of megalin and cubilin in the *Ehd1*$^{-/-}$ mouse kidney compared to the control. 87
Figure: 4.27: Different subcellular localization of WT-hEHD1 and R398W-hEHD1. 89
Figure 4.28: Comparison of WT-hEHD1 and R398W-hEHD1 protein stability. 90
Figure 4.29: Bovine serum albumin transepithelial transport by polarized LLC-PK1 inducible cells. 91
Figure 4.30: β_2-microglobulin-Alexa Fluor 546 uptake by polarized LLC-PK1 inducible cells. 92
Figure 4.31: mRNA levels of EHD1 partners in the LLC-PK1 inducible cells. 93
Figure 11.1: Representative quantification of the endocytosed β_2-microglobulin-Alexa 546 by a proximal tubule over 40 min. 121
Figure 11.2: EHD1 endogenous expression in non-induced WT- and R398W-hEHD1 LLC-PK1 cell lines. 121
Figure 11.3: Immunofluorescence of acetylated tubulin in mouse kidney tissue. 122

10. List of Tables

Table 1.1: Expression of EHD proteins in the mouse tissues. 7
Table 1.2: Relationship of EHD proteins with human disease. 20
Table 4.1: Genotypes of pups obtained from *Ehd1* mutant mouse breeding pairs.....66

11. Supplements

11.1 Figures

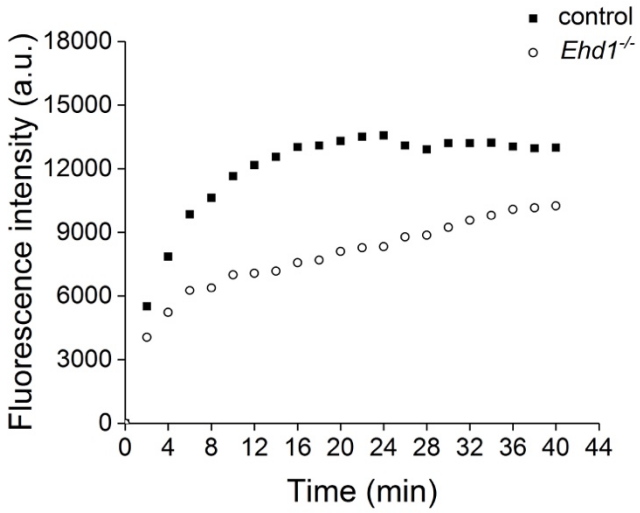

Figure 11.1: Representative quantification of the endocytosed β_2-microglobulin-Alexa 546 by a proximal tubule over 40 min.

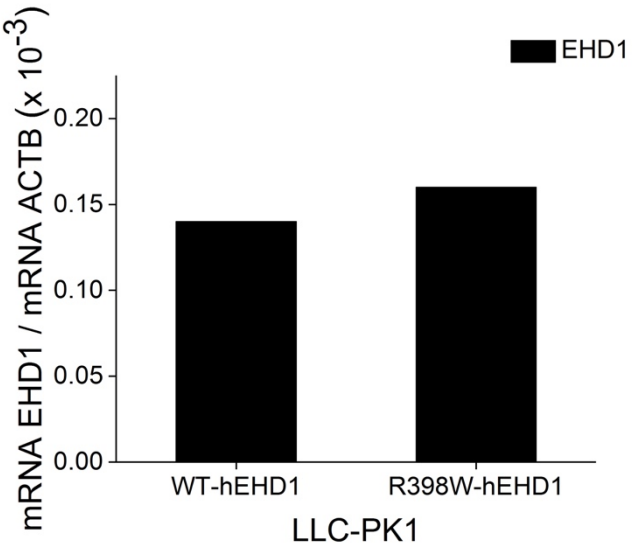

Figure 11.2: EHD1 endogenous expression in non-induced WT- and R398W-hEHD1 LLC-PK1 cell lines.

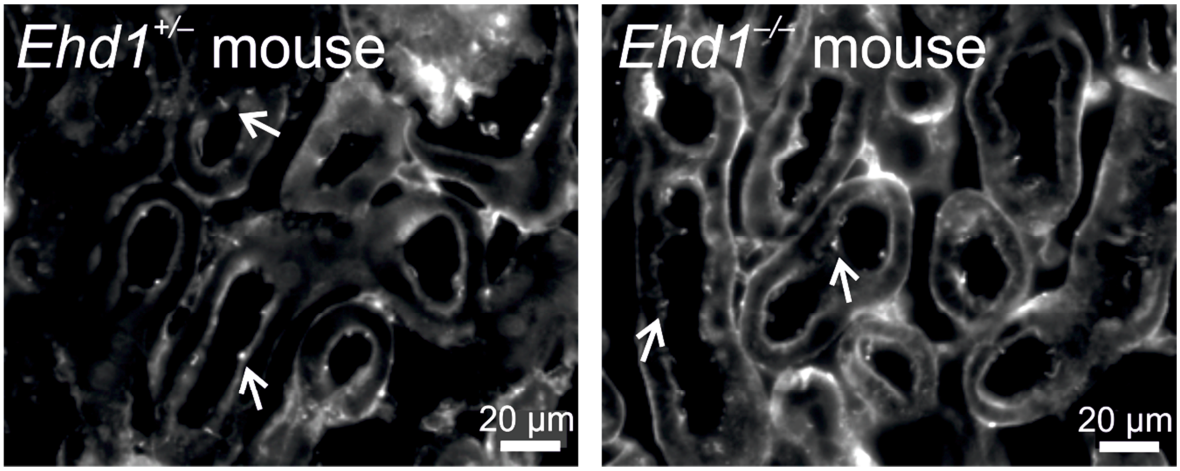

Figure 11.3: Immunofluorescence of acetylated tubulin in mouse kidney tissue.
Cilia (white arrows) were observed in both control and *Ehd1*$^{-/-}$ kidneys.

11.2 Publications in preparation

Afonso S., Issler N., Sterner C., Klootwijk E.D., Tziridis K., Schilling A., Schulze H., Witzgall R., Warth R., Kleta R.

EHD1, a role in proximal tubule endocytosis

11.3 Presentations at scientific conferences

“Expression and localization of KCNJ16 in various mouse tissues”, Poster presentation at 95th Annual Meeting of the German Physiological Society 2016 in Lübeck

“A role of the inwardly rectifying potassium channel Kir4.1 in the regulation of water homeostasis?”, Poster presentation at 96th Annual Meeting of the German Physiological Society 2017 in Greifswald

11.4 Eidesstattliche Erklärung

Ich erkläre hiermit an Eides statt, dass ich die vorliegende Arbeit ohne unzulässige Hilfe Dritter und ohne Benutzung anderer als den angegebenen Hilfsmitteln angefertigt habe. Die aus anderen Quellen direkt oder indirekt übernommenen Daten und Konzepte sind unter Angabe des Literaturzitats gekennzeichnet.

Die im Methodenteil, im Resultateteil und in der Danksagung aufgeführten Personen haben mir in der jeweils beschriebenen Weise unentgeldlich geholfen.

Weitere Personen waren an der inhaltlich-materiellen Herstellung der vorliegenden Arbeit nicht beteiligt. Insbesondere habe ich hierfür nicht die entgeldliche Hilfe eines Promotionsberaters oder anderer Personen in Anspruch genommen. Niemand hat von mir weder unmittelbar noch mittelbar geldwerte Leistungen für Arbeiten erhalten, die im Zusammenhang mit dem Inhalt der vorgelegten Dissertation stehen.

Diese Arbeit wurde bisher weder im In- noch im Ausland in gleicher oder ähnlicher Form einer anderen Prüfungsbehörde vorgelegt.

…….

Sara Cerqueira Afonso

12. Acknowledgments

Here, I would like to express my gratitude to everyone who contributed to the success of this work.
First I would like to thank my supervisor Prof. Dr. Richard Warth for the guidance throughout my PhD. For all the great ideas and his constant excitement about this project. For showing me that although science is not always kind to us, it is something that we were born to love.

A huge thank you to all the people in the Warth's lab. With them I shared endless laughs and got precious advices. Special thanks to Sascha for all the shared knowledge and Markus for all the Photoshop lessons and table football at the end of the day. Ein großen Dank an Ines für die unendlichen Bestellungen, Zellkultur Ratschläge und die deutschen Gespräche. To Kathrin and Julia, a thank you for the amazing companionship. To Anna-Lena a special thank you for all the scientific advices, the help in the correction of this thesis and all the cinema evenings. To my partner in crime, Christina, my gratitude is beyond limits. For all the hours spent together in this project, for all the knowledge passed on to me and for the friendship my deepest thank you. To Catarina, thank you for coming and joining me on this endeavor. With you in the lab Portugal felt always near.
Thank you also to Philipp, Julia Stindl and Carsten for their advices and positive energy.

I also would like to thank Prof. Dr. Robert Kleta and Dr. Naomi Issler for all their work with the patients, without them this dissertation would have never been possible. A special thank you to Dr. Ina Schießl, Prof. Dr. Ralph Witzgall and Achim Schilling for their help with the multiphoton microscopy, electron microscopy and ABR measurements.

Thank you to Carina, Rui, Karina, Flávio, Inês, Diana and Mauro for making Regensburg my home.

Vielen Dank an Tobi für dein Vertrauen in mich, dass du immer für mich da warst und, was noch wichtiger ist, dass du mir gesagt hast was ich nicht hören wollte, aber hören musste. Danke auch an seine Familie, die mir das Gefühl gibt, dass ich zu ihr gehöre.

Para os meus pais e irmão, que sempre tudo fizeram para tornar os meus sonhos realidade e me mostraram o seu incondicional apoio, o meu maior obrigada. Esta tese é para vocês.